MEASURING THE ^{15}O(α, γ)^{19}Ne REACTION IN TYPE I X-RAY BURSTS USING ^{20}Mg β-DECAY

By

Tyler Markham Wheeler

A DISSERTATION

Submitted to
Michigan State University
in partial fulfillment of the requirements
for the degree of

Physics - Doctor of Philosophy

2024

ABSTRACT

MEASURING THE ^{15}O(α, γ)^{19}Ne REACTION IN TYPE I X-RAY BURSTS USING ^{20}Mg β-DECAY

By

Tyler Markham Wheeler

A neutron star can accrete hydrogen-rich material from a low-mass binary companion star. This can lead to periodic thermonuclear runaways, which manifest as Type I X-ray bursts detected by space-based telescopes. Sensitivity studies have shown that ^{15}O(α, γ)^{19}Ne carries one of the most important reaction rate uncertainties affecting the modeling of the resulting light curve. This reaction is expected to be dominated by a narrow resonance corresponding to the 4.03 MeV excited state in ^{19}Ne. This state has a well-known lifetime, so only a finite value for the small alpha-particle branching ratio is needed to determine the reaction rate. Previous measurements have shown that this state is populated in the decay of ^{20}Mg. ^{20}Mg($\beta p\alpha$)^{15}O events through the key ^{15}O(α, γ)^{19}Ne resonance yield a characteristic signature: the near simultaneous emission of a proton and alpha particle.

To identify these events of interest the GADGET II TPC was used at the Facility for Rare Isotope Beams during Experiment 21072. An ^{36}Ar primary beam was impinged on a ^{12}C target to create a fast beam of ^{20}Mg whose decay fed the ^{19}Ne state of interest. The details of the development, and testing of the GADGET II system will be discussed along with the preliminary results from this experiment, which include discussion of the data processing and analysis methods being used on the newly acquired data.

Moreover, convolutional neural networks (CNNs) are explored for rare event identification in the TPC data. To leverage the computational advantages of 2D CNNs and the availability of pre-trained models, early data fusion techniques have been adopted to efficiently convert

the data into 2D formats. Addressing real training data scarcity and simulation discrepancies, parameter variations are incorporated in simulations to enhance model robustness, making the CNNs ultra-sensitive to subtle event indicators. The resulting ensembles deployed on the experimental data are able to identify >98% of all two-particle-events in the dataset. The techniques of this ongoing study are detailed, highlighting the promising future applications of this methodology.

ACKNOWLEDGMENTS

This portion will be updated in a future version of this document.

TABLE OF CONTENTS

LIST OF TABLES

LIST OF FIGURES

KEY TO ABBREVIATIONS

- ADC - Analogue to Digital Converter
- ARIS - Advanced Rare Isotope Separator
- AsAd Board - ASIC and ADC Board
- ASIC - Application Specific Integrated Circuit
- ATTPC - Active-Target Time Projection Chamber
- CERN - European Council for Nuclear Research
- CNN - Convolutional Neural Network
- CNO Cycle - Carbon-Nitrogen-Oxygen Cycle
- CoBo Board - Concentration Board
- DAQ - Data Acquisition
- DEGAi - Decay Germanium Array initiator
- FC - Fully Connected
- FDSi - FRIB Decay Station initiator
- FPGA - Field Programmable Gate Array
- FRIB - Facility for Rare Isotope Beam
- GADGET - GAseous Detector with GErmanium Tagging
- GET - Generic Electronics for TPCs
- HCNO Cycle - Hot Carbon-Nitrogen-Oxygen Cycle
- HPGe - High-purity Germanium
- LinAc - Linear Accelerator
- ML - Machine Learning
- MM - MicroMegas
- MSU - Michigan State University
- MuTanT Module - Multiplicity, Trigger and Time Module
- ORNL - Oak Ridge National Laboratory

- PCA - Principal Component Analysis
- PCB - Printed Circuit Board
- PMT - Photomultiplier Tube
- ReLU - Rectified Linear Unit
- SGD - Stochastic Gradient Descent
- SPE - Squared Prediction Error
- TPC - Time Projection Chamber

Chapter 1

Overview of Relevant Nuclear Physics

1.1 Introduction to Nuclei

The atom, often called the fundamental building block of matter, has been the subject of scientific curiosity and investigation for centuries. However, it was only in the early 20th century that significant breakthroughs in our understanding of its intricate structure were achieved. Contrary to earlier models that envisioned the atom as a homogenous blend of positive and negative charges (the so-called "plum pudding" model [20]), groundbreaking experiments in the early 1900s unveiled a more complex reality.

In a pivotal experiment, the physicist Ernest Rutherford directed a beam of alpha particles (helium nuclei) towards a thin sheet of gold. According to the plum pudding model, the alpha particles should have passed through the gold foil with only slight, infrequent deflections. However, the experimental results were surprising and changed our understanding of the atom. While most of the alpha particles did pass through the gold foil with minimal deflection, a small number were deflected at very large angles, and some were even scattered straight back towards the source [21]. This unexpected behavior suggested that the atom's positive charge, along with most of its mass, was concentrated in a central region, later termed the "nucleus."

The experimental endeavors following Rutherford's alpha particle scattering experiment further enhanced our understanding of atomic structure, particularly with the discovery of

the neutron by James Chadwick in 1932 [22]. This discovery was instrumental in refining the atomic model. It revealed that the nucleus consists of two types of nucleons: protons, which are positively charged, and neutrons, which are electrically neutral. These nucleons are bound together by the strong nuclear force, a powerful fundamental interaction that overcomes the electrostatic repulsion between the positively charged protons.

A nucleus is distinctly defined by its elemental name and mass number, A, where the mass number represents the sum of protons and neutrons within the nucleus. The elemental name is determined by the proton count, Z, a feature that forms the basis of the periodic table. For instance, a magnesium nucleus with 12 protons and 8 neutrons is denoted as ^{20}Mg, where the elemental symbol, Mg, inherently provides the atomic number information.

The atomic landscape showcases a variety of nuclear configurations. Isotopes are one such variation, characterized by nuclei of the same element (same number of protons) but differing in their neutron numbers. These differences in the number of neutrons between isotopes do not alter the chemical properties of the element but do affect the nuclear properties, such as stability and decay modes (more on decay modes in Section 1.3).

In contrast, isotones are nuclei that share an identical neutron count but differ in their number of protons, thus they are different elements. Isotones often exhibit different chemical properties due to their varying atomic numbers but can share some nuclear characteristics due to having the same number of neutrons. Additionally, the term isobar applies to nuclei with the same mass number A but different numbers of protons and neutrons. Isobars, therefore, belong to different elements and have distinct nuclear properties.

Nuclear isomers are another fascinating aspect of nuclear variety. They represent nuclei with the same number of protons and neutrons but with different energy states, referred to as excited states. Isomers exist because nucleons in a nucleus can arrange in different energy

configurations. This can mean a nucleon moving to a higher energy orbital, or adding rotational or vibrational energy to the core of paired nucleons [3] (see the discussion of the shell model in Section 1.2). Some of these configurations/states can be relatively stable, leading to the existence of metastable isomers that have longer half-lives. A classic example of this is Technetium-99m, a metastable nuclear isomer used in medical imaging [23]. Other states are extremely unstable and decay rapidly via different decay modes.

The chart of nuclides provides a comprehensive map of all known nuclei, encompassing both stable and unstable varieties. This chart plots Z vs N, and is an invaluable tool for understanding the relationships and properties of different nuclear species, including isotopes, isotones, isomers, and isobars. It serves as a visual representation of the intricate and diverse world of nuclear physics and can be seen in Figure 1.1.

The nucleus's unveiling brought forth a myriad of questions, particularly about the origins of elements. This curiosity birthed the domain of nuclear astrophysics in the mid-20th century. Pioneering work in this field aimed to discover the origins of the elements. As the discipline evolved, it grappled with profound questions about stellar energy generation, life cycles of stars, nucleosynthesis sites, and the stellar events responsible for creating various isotopes (more on the field of nuclear astrophysics can be found in Section 1.4).

To navigate these cosmic riddles, a deep comprehension of nuclear structure (properties of stable and unstable nuclei) and nuclear reactions (interactions between nuclei) is crucial.

1.2 Nuclear Shell Model

The nuclear shell model has been critical in improving our understanding of nuclear structure and behavior, offering profound insights into the internal arrangements and energy states of

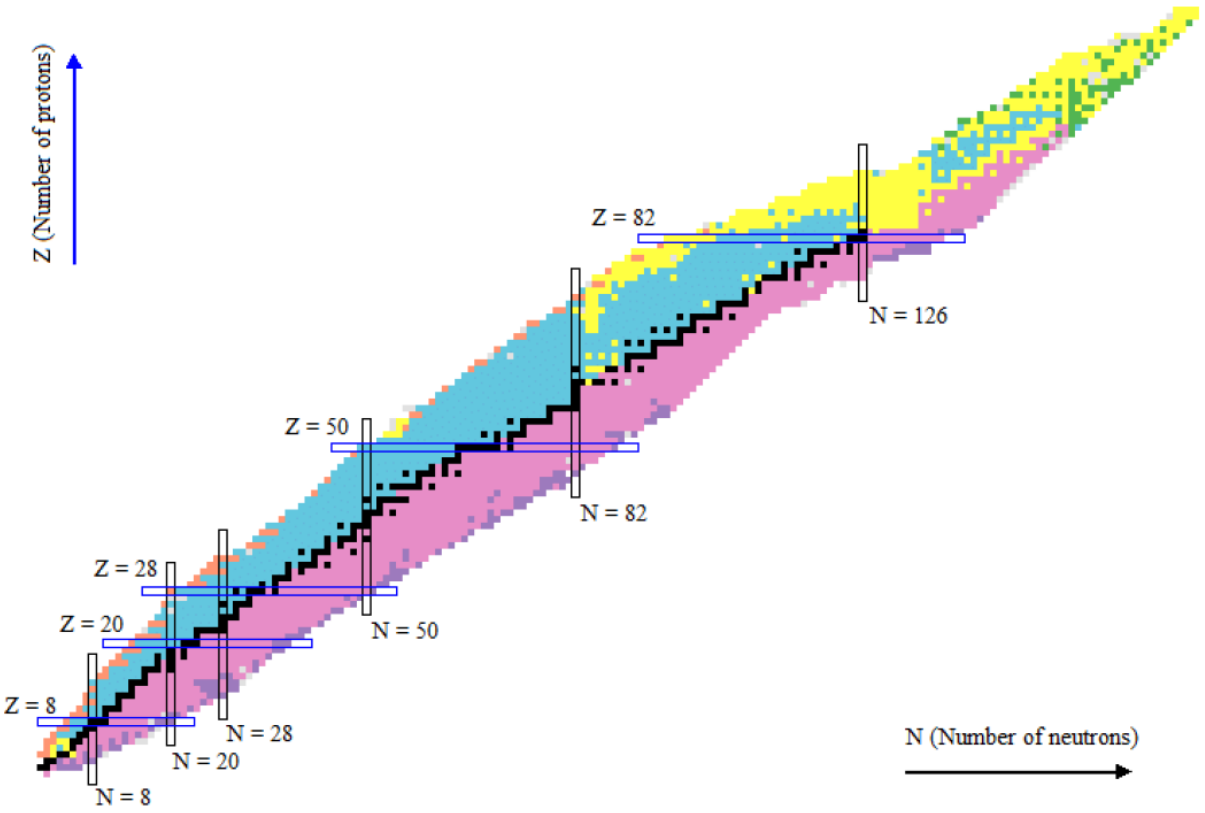

Figure 1.1: The chart of nuclides. On this chart, the y-axis signifies the number of protons (Z) in the nucleus, while the x-axis indicates the number of neutrons (N). Black boxes on the chart identify stable nuclei, and boxes in various colors represent various types of unstable nuclei. [1]

a given nucleus. The model draws inspiration from the atomic shell model, where electrons are organized into discrete (quantized) energy levels called shells. Electrons fill these shells in order of increasing energy, with the lowest energy levels (closest to the nucleus) being filled first. As these shells are filled, electrons occupy higher and higher energy shells consistent with the Pauli exclusion principle. With this approach, we obtain a structure consisting of a stable core formed by completely filled shells, accompanied by a number of valence electrons. The model then posits that the fundamental properties of atoms are primarily influenced by these valence electrons, and this theory has been remarkably successful. Interestingly, proton and neutron separation energies exhibit patterns and discontinuities at specific nucleon numbers, analogous to the changes in atomic properties observed with electron configurations [3]. This suggested that a similar model could be applied to nuclear structure.

In the nuclear shell model protons and neutrons fill shells independently. Each shell contains subshells called orbitals, that are determined by the quantum states the nucleons can occupy. The states are characterized by quantum numbers that include the orbital angular momentum l, the total angular momentum j, and the principal quantum number n, which refers to the number of nodes in the corresponding wave function and can be effectively represented using a harmonic oscillator potential (see Figure 1.2). Note that no 2 protons or neutrons in a given nucleus can have the exact same quantum numbers, as nucleons are fermions, which means that they are spin $s = 1/2$ particles that obey the Pauli Exclusion Principle. This characteristic inherently limits the capacity of each shell.

Each shell contains specific types of orbitals denoted as s, p, d, f..., where each letter corresponds to a specific value for the orbital angular momentum ($l = 0, 1, 2, 3...$). The degeneracy for each orbital (the number of protons or neutrons in each subshell) is given by $2l + 1$. To get this shell structure to agree with observed data, a critical modification

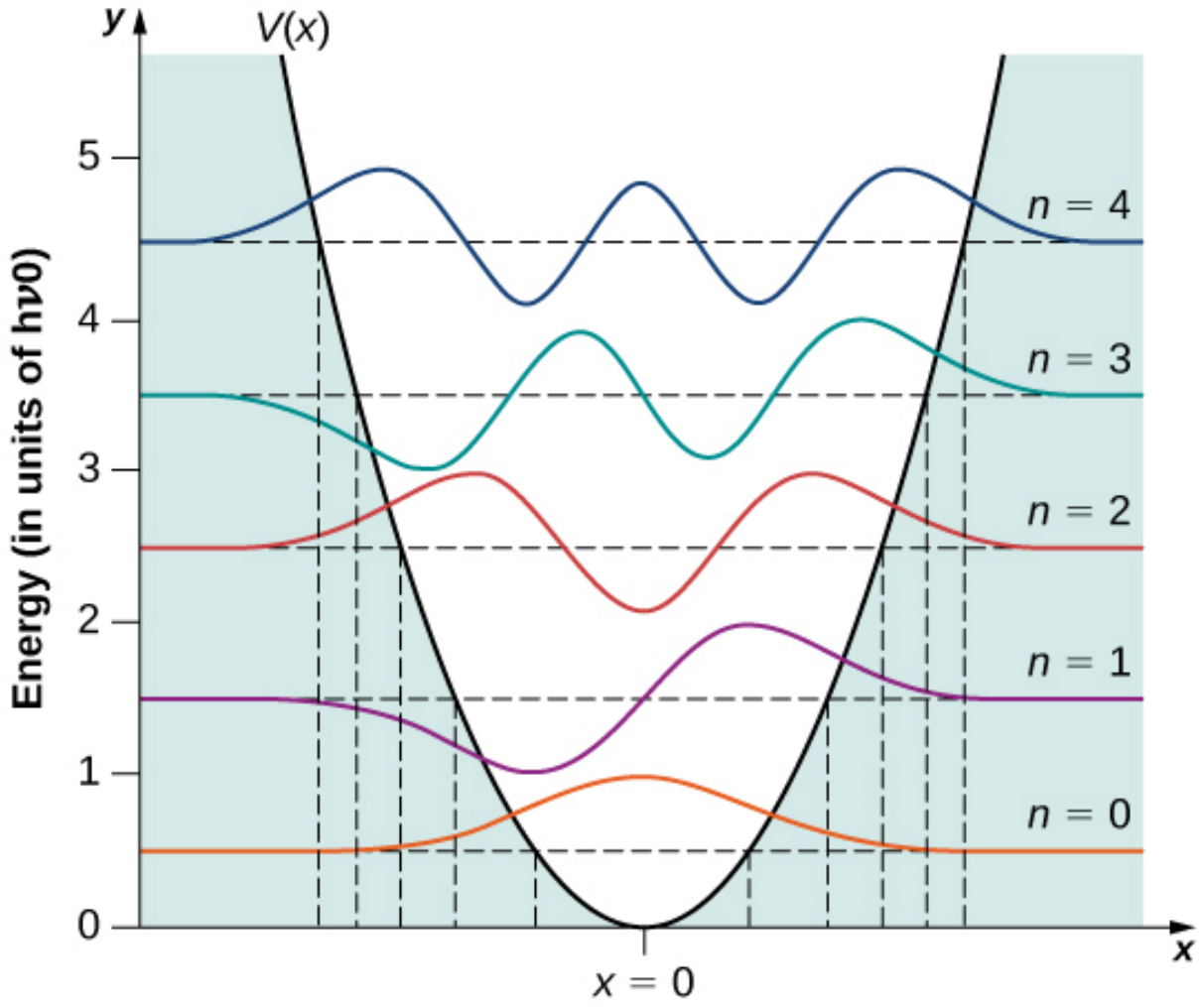

Figure 1.2: Figure illustrates the first five wave functions of a quantum harmonic oscillator. Vertical lines mark the classical turning points, representing the extremities of motion for a classical particle with equivalent energy. This depiction shows how, with increasing principal quantum number, the wave functions transition between even and odd symmetries.[2]

is needed; spin-orbit coupling. This concept is essential for the correct ordering of nuclear subshells and the emergence of the magic numbers (2, 8, 20, 28, 50, 82, 126), which represent the observed number of nucleons needed to fill each successive major shell. From spin-orbit coupling we derive the expression for the total angular momentum: $j = l \pm 1/2$, where a larger j value represents a lower energy state. Then the spacing between levels depends on the spin-orbit potential. An example of the single-particle energy level scheme for the harmonic oscillator potential can be seen in Figure 1.3. Note that in this context, the number in front of the denoted orbital does not represent the principal quantum number but rather serves as a counter for the number of levels corresponding to a specific l value. This means that the '1d' level refers to the initial (lowest) d state, '2d' identifies the subsequent d-state, etc.

Based on the above let's work through an example using ^{20}Mg. The isotope of ^{20}Mg contains 12 protons and 8 neutrons. We can see from Figure 1.3 that the 8 neutrons will completely fill the p-shell. The protons will also fill the p-shell, so the first 8 protons and neutrons combine to form something like an inert ^{16}O core. Then the remaining protons will go into the $d_{5/2}$-shell. From this we can determine the spin and parity, J^{π}, of this nucleus in the ground state (lowest possible energy configuration). In this case J is the total coupled angular momentum of the system, and π is the parity, which refers to the symmetry of the nuclear structure under coordinate inversion, and is given as $(-1)^l$. Of the four protons in the $d_{5/2}$-shell, two will be spin-up and two will be spin-down, which leaves us with a total angular momentum of $J = 0$. Then the d-shell corresponds to l=2, which gives us positive parity. Thus, the ground state of ^{20}Mg can be described as $J^{\pi} = 0^{+}$.

There are of course other models (liquid drop model, collective model, etc.), however, the nuclear shell model, with its basis in empirical evidence and its successful predictions,

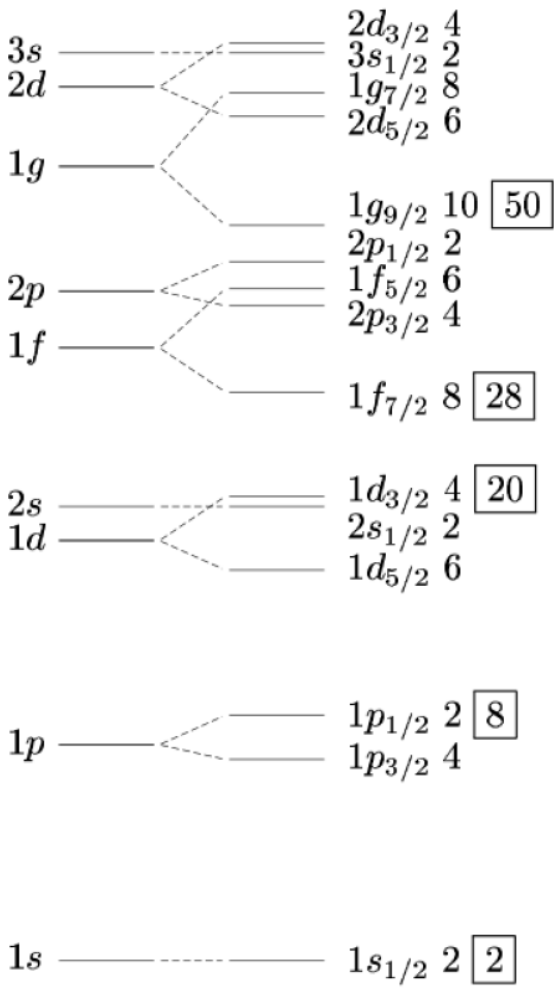

Figure 1.3: Single-particle energy level scheme derived from the harmonic oscillator potential. The spin-orbit component in the nuclear potential results in the division of these energy levels, which approximates shell closures and leads to the emergence of the magic numbers (the boxed integers). Figure Credit: Bakken (GPL)

remains an essential tool in nuclear physics. While simplified, it provides deep insights into the complex world of nuclear structure and interactions, underscoring the intricacies of the forces at play within the atomic nucleus.

1.3 Nuclear Decay

The chart of nuclides, Figure 1.1, reveals that a majority of nuclei are inherently unstable. Such nuclei invariably undergo a transformation, or decay, transitioning towards a more stable state. The degree of instability of a nucleus can often be gauged by its distance from the line of stability on the chart of nuclides (black boxes in Figure 1.1): the farther it is, the greater its instability.

Interestingly, the exact moment an unstable nucleus will decay is unknowable, and this unpredictability is deeply rooted in the principles of quantum mechanics. In quantum mechanics, the behavior of particles, including atomic nuclei, is inherently probabilistic. However, this probabilistic nature means that when we observe a substantial sample of identical nuclei, their decay behavior adheres to the exponential law of radioactive decay. This can be mathematically represented as:

$$N(t) = N_0 e^{-\lambda t} \tag{1.1}$$

where $N(t)$ denotes the number of undecayed nuclei at time t, N_0 is the initial number of nuclei, and λ is the decay constant. Note also that the term $\tau = \frac{1}{\lambda}$ signifies the mean lifetime of the nucleus, representing the average time for a nucleus to decay [3]. Thus, the decay constant (λ) is notably larger for nuclei that are very unstable, when juxtaposed with nuclei

near stability.

Nuclei can undergo decay through various mechanisms. Lighter nuclei predominantly decay via mechanisms such as β-decay, γ-decay, and particle emission (like proton, neutron, or α-particle emission). In contrast, heavier nuclei, while also susceptible to the aforementioned decay modes, have the added possibility of undergoing spontaneous fission. In this process, a nucleus splits into two fragments of nearly equal size. Spontaneous fission is a significant decay mode for superheavy elements (A $>$ 232) and sets a practical limit on the number of nucleons in heavy elements.

A nucleus may undergo decay through multiple pathways, each known as a decay branch. These branches represent the nucleus's potential transitions to different states. The total lifetime of the parent nucleus τ_{total} is a composite measure that intertwines the decay rates of all possible branches. It's mathematically expressed as:

$$\tau_{\text{total}} = \frac{1}{\sum_i \lambda_i} \tag{1.2}$$

where λ_i represents the decay constant for each branch, indicating the rate of decay along that specific pathway.

While the total lifetime offers a collective perspective, understanding the individual decay constants, λ_i, is crucial. These constants illuminate the branching ratios – the probabilities of the nucleus decaying via each particular branch. Knowledge of these ratios is fundamental for accurately predicting nuclear behavior and understanding the stochastic nature of nuclear decay.

1.3.1 α-Decay

Alpha decay, a process governed by the interaction of the strong nuclear force and the Coulomb force, serves as a pathway for nuclei to achieve greater stability. It involves the emission of an alpha particle (helium nucleus), which is comprised of two protons and two neutrons. The alpha particle can be seen as a beacon of stability, having a significantly higher binding energy than neighboring isotopes, meaning it has a small mass relative to its separate constituents. Thus, this tightly bound quartet of nucleons is a favored particle to emit, and once it escapes from a parent nucleus the resulting daughter nucleus will be in a more stable configuration [3].

For a nucleus represented as ${}^{A}_{Z}X$, alpha decay transforms it into a lighter nucleus ${}^{A-4}_{Z-2}Y$ plus the emitted alpha particle. The process can be elegantly expressed as:

$$ {}^{A}_{Z}X \rightarrow {}^{A-4}_{Z-2}\,Y + \alpha \tag{1.3}$$

The energy dynamics of this transformation are encapsulated in the Q-value for alpha decay, Q_α. This value represents the net energy released during the decay process and is the difference in mass-energy between the initial state (parent nucleus ${}^{A}_{Z}X$) and the final states (daughter nucleus ${}^{A-4}_{Z-2}Y$ and the alpha particle). The Q-value is given by:

$$ Q_\alpha = [m({}^{A}_{Z}X) - m({}^{A-4}_{Z-2}Y) - m_\alpha]c^2 \tag{1.4}$$

In alpha decay, the Q-value is a testament to the transformation of mass into kinetic energy, shared between the daughter nucleus and the alpha particle. This energy release is the driving force of alpha decay, propelling the alpha particle on its journey away from the

parent nucleus and signifying the shift towards stability.

1.3.2 β-Decay

Beta decay is mediated by the weak force and is the process whereby a proton is converted into neutron or vice versa. This conversion conserves mass number ($A = Z+N$), but changes both the proton number (Z) and the neutron number (N) by one unit such that $Z \rightarrow Z \pm 1$, $N \rightarrow N \mp 1$. Thus, this process is a convenient path for steering nuclei towards stability [3].

Beta-minus decay (β^--decay) occurs in neutron-rich nuclei below the stability line, transforming a neutron into a proton while emitting an electron (e^-) and an electron antineutrino ($\bar{\nu}_e$). This transformation can be represented by:

$$ {}^{A}_{Z}X \rightarrow {}^{A}_{Z+1}Y + e^- + \bar{\nu}_e \tag{1.5} $$

The energy released, denoted by the Q-value $Q_{\beta-}$, is the mass-energy difference between the parent and daughter nuclei, converted into kinetic energy:

$$ Q_{\beta-} = [m({}^{A}_{Z}X) - m({}^{A}_{Z+1}Y)]c^2 \tag{1.6} $$

Beta-plus, or positron decay (β^+-decay) is observed in proton-rich nuclei, involving the conversion of a proton to a neutron, and emitting a positron (e^+), electron neutrino (ν_e), and an additional electron (e^-) to conserve charge. The process is viable only if the Q-value, $Q_{\beta+}$, exceeds the combined mass of two electrons (1.022 MeV). This threshold accounts for the energy required to create the emitted positron and the electron that the atom must emit to balance the charge. An expression for this transformation and the corresponding Q-value

can be given as:

$$ {}^{A}_{Z}X \rightarrow {}^{A}_{Z-1}Y + e^{+} + \nu_e \tag{1.7} $$

$$ Q_{\beta+} = [m({}^{A}_{Z}X) - m({}^{A}_{Z-1}Y) - 2m_e]c^2 \tag{1.8} $$

Electron capture, another decay mode for proton-rich nuclei mediated by the weak interaction, involves the nucleus capturing an inner orbital electron to convert a proton into a neutron:

$$ {}^{A}_{Z}X + e^{-} \rightarrow {}^{A}_{Z-1}Y + \nu_e \tag{1.9} $$

The associated Q-value, Q_{EC}, considers the binding energy of the captured electron:

$$ Q_{EC} = [m({}^{A}_{Z}X) - m({}^{A}_{Z-1}Y)]c^2 - BE(e^{-}) \tag{1.10} $$

These processes illustrate the complexity of beta decay, involving continuous energy spectra for emitted electrons, the introduction of neutrinos, and the nuanced interplay of nuclear forces, reflecting the intricate nature of atomic transformations.

1.3.3 γ Decay

Following α or β decay it is typical for a nucleus to be left in an excited state, and then rapidly decay to the ground state via the emission of one or more γ-rays [3]. Gamma-rays are high-energy (0.1 to 10 MeV) photons that when emitted don't alter the atomic number or mass number of the nucleus. The energy of the emitted gamma ray is equal to the energy difference between the initial and final nuclear states, described by:

$$ \Delta E = E_i - E_f = E_\gamma + KE_{rec} \tag{1.11} $$

where ΔE is the energy released in the transition, E_i is the energy of the initial state, E_f is the energy of the final state, E_γ is the energy of the emitted γ-ray, and KE_{rec} is the kinetic energy of the recoiling nucleus. KE_{rec} can be expressed in terms of its momentum using the classical kinetic energy formula for non-relativistic speeds:

$$KE_{rec} = \frac{p_{rec}^2}{2M_f} \tag{1.12}$$

where M_f is the mass of the recoiling nucleus and p_{rec} its momentum. Additionally, conservation of momentum dictates that the momentum of the recoiling nucleus is opposite in direction to that of the emitted gamma-ray ($\vec{p}_\gamma$ where $p_\gamma = \frac{E_\gamma}{c}$) :

$$\vec{p}_\gamma = -\vec{p}_{rec} \tag{1.13}$$

Using the above, we get the following expression for KE_{rec}:

$$KE_{rec} = \frac{1}{2M_f}\left(\frac{E_\gamma}{c}\right)^2 = \frac{E_\gamma^2}{2M_f c^2} \tag{1.14}$$

Then the total energy balance of the process is represented by:

$$\Delta E = E_\gamma + \frac{E_\gamma^2}{2M_f c^2} \tag{1.15}$$

The energy of an emitted gamma-ray allows us to deduce the energy of the corresponding excited state from which it was emitted, and our knowledge of nuclear spectroscopy is tantamount to our knowledge of excited states. Thus, the study of gamma-ray emission emerges as a gold standard technique in nuclear spectroscopy [3]. This method, celebrated for its

ability to measure gamma-ray energies with remarkable precision, works to reveal the complex energy levels of excited nuclear states, thereby enhancing our understanding of nuclear structure and dynamics. Additionally, the study of gamma emission and internal conversion together provides a robust framework for deducing intrinsic nuclear properties, such as spins and parities of excited states, thereby offering a holistic view of nuclear behavior.

1.3.4 Nucleon Emission

Nucleon emission (the emission of a proton or neutron) hinges on the Q-value for the decay being positive. This process is encapsulated by the neutron separation energy (S_n) and proton separation energy (S_p), defined as the differences in binding energy when a neutron or proton, respectively, is removed from a nucleus:

$$S_n = -Q_n = BE(N;Z) - BE(N-1;Z) \tag{1.16}$$

$$S_p = -Q_p = BE(N;Z) - BE(N;Z-1) \tag{1.17}$$

These energies delineate the threshold beyond which nuclei become unstable against nucleon loss, delineating the so-called nuclear drip-line [3]. Here, nuclei are replete with excess protons or neutrons, and any attempt to add another nucleon fails, as it 'drips off' unbound, signifying the transition from positive to negative separation energies.

Similar to gamma-decay (Section 1.3.3), nucleon emission can occur following beta-decay (Section 1.3.2), and will be in competition with gamma-decay. This happens if the resulting nucleus is in a sufficiently excited state (E_{exc}) such that $E_{exc} > S_N$ (where $N = n$ or p). This phenomenon is termed beta-delayed nucleon emission, and a schematic of the process

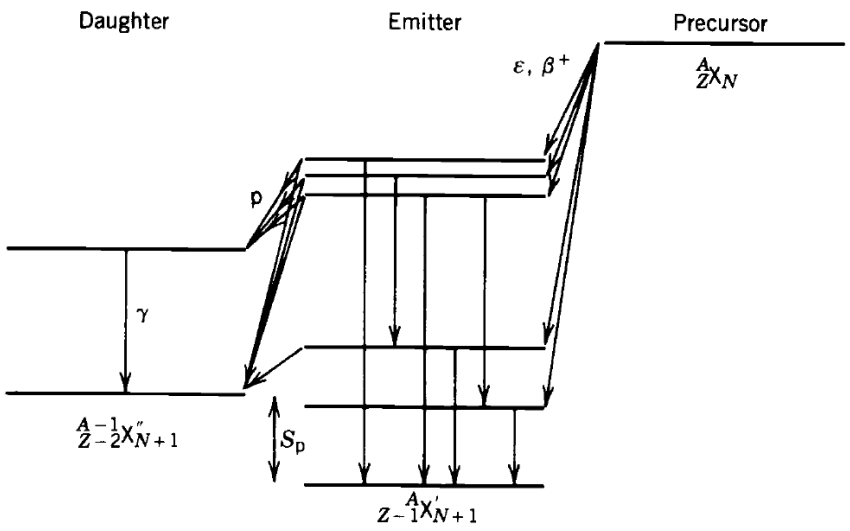

Figure 1.4: Schematic of beta-delayed nucleon emission: The beta decay of the precursor leads to the population of highly excited states within the emitter. These states are prone to nucleon emission due to their instability. It is important to recognize that the energy level of the emitter's excited state is the sum of the energy of the nucleon emitted, and the nucleon separation energy between states X' and X", and a minor adjustment accounting for the recoil of the emitting nucleus [3].

can be seen in Figure 1.4.

1.4 Introduction to Nuclear Astrophysics

The field of nuclear astrophysics marries the intricate principles of nuclear physics with the grand tapestry of cosmic phenomena. There are a host of fundamental questions at the heart of astrophysics, and cosmology that can only be answered if we posses a detailed understanding of nuclear structure and nuclear reactions, and such is the work of nuclear astrophysicists.

The field came into prominence in the mid to late 1960s, a pivotal era when the Big Bang theory crystallized as the prevailing narrative of cosmic genesis. However, the Big Bang was found to produce primarily the lightest elements—hydrogen, helium, and traces of lithium [9]. This revelation gave rise to a cosmic conundrum: if the Big Bang birthed only the

lightest elements, how did the rest of the elements form? It was against this backdrop that the concept of nucleosynthesis, championed by astrophysicist Fred Hoyle, came into favor, proposing that the synthesis of heavier elements occurs within stars.

Discoveries such as the existence of technetium in red giant stars worked to solidify the concept of nucleosynthesis. Technetium is a transient element without stable isotopes and a life-time that is far shorter than the age of the universe [24]. Thus, stars are not just nuclear furnaces but also cosmic crucibles where the elements of the universe are forged. Over eons stars transmute the primordial Big Bang elements into a rich array of heavier elements. The mechanisms of alpha, beta, and gamma decays, detailed in the previous sections, are not confined to Earthly laboratories but are active participants in the alchemy of stars.

In the realm of nuclear astrophysics, the role of observational astronomy is pivotal in painting a detailed picture of cosmic processes. This pursuit is complemented by nuclear experiments probing the properties of atomic nuclei. This interdisciplinary field, thus, seeks to unravel the origins of the elements, the nature of matter in extreme astrophysical environments, the properties of neutron stars, and much more. In the context of this thesis, we will be exploring the nuclear physics underlying X-ray bursts from neutron stars (see Section 3). And in so doing we will discover how measuring critical nuclear reactions within these bursts can shed light on the properties of neutron stars including their mass, radius, and crust elemental composition.

Chapter 2

Overview of Relevant Machine Learning Algorithms

2.1 Convolutional Neural Networks

Machine learning (ML) represents a significant stride in the field of artificial intelligence, offering the ability to automate the extraction of knowledge from data. Among its many applications, ML excels in pattern recognition, and predictive analytics. The essence of machine learning lies in its capability to learn and improve from experience without being explicitly programmed for specific tasks. This adaptability makes it a powerful tool across a wide array of domains.

In recent years, the focus has shifted towards deep learning, a subset of ML, which employs neural networks with multiple layers. These multilayered structures, known as deep neural networks, are adept at handling vast amounts of data and extracting complex patterns. Convolutional Neural Networks (CNNs), a class of deep neural networks, have gained prominence, particularly in the realm of image processing and classification [25].

In the context of this thesis, the focus on CNNs is particularly pertinent due to the nature of the experimental data gathered. The data for this thesis experiment was obtained using a Time Projection Chamber (TPC) (see Chap. 4 for details on TPCs). TPC data can be visualized as 2D images, as illustrated in Figure 4.7. This representation aligns perfectly with the

capabilities of CNNs, making them the most appropriate choice for analyzing and extracting valuable insights from the dataset [19]. By employing CNNs, we can harness the computational efficiency and superior performance of these networks, particularly in image-related tasks. Furthermore, the availability of a wide range of pre-trained models allows for leveraging and fine-tuning these models to suit our specific dataset and tasks, thereby enhancing the model's performance and reducing the need for extensive computational resources.

In the following sections, we delve into the fundamental components and strategies involved in optimizing CNNs, ensuring that they are well-equipped to handle the intricacies of the dataset in question.

The subsequent sections/subsections are adapted from our other work that is currently in preparation [26]. These adaptations are used with permission and have been modified to fit the context of this thesis.

2.1.1 CNN Building Blocks

Convolutional Layers: The convolutional layer stands as the core component of a CNN, and it is primarily responsible for feature extraction from images. An image input to this layer is typically in the format of $n \times n \times n_c$, where n represents the image's width and height, and n_c denotes the channel count (for instance, $n_c = 3$ in RGB images).

Within a convolutional layer, several filters (or kernels) are present, each possessing adjustable parameters. These filters are characterized by dimensions $f \times f \times n_c$, with f being smaller than n (common values for f include 3, 5, or 7), allowing the filter to have a compact receptive field that spans the full depth of the input volume, n_c. The application of these filters across the entire image facilitates the extraction of a diverse set of features, with each filter targeting different characteristics of the image.

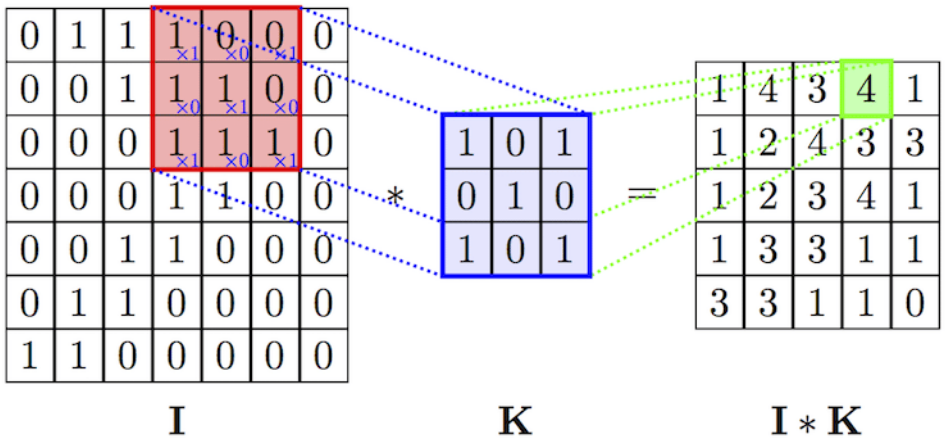

Figure 2.1: An illustration of the convolution process. The input is a 7 x 7 image, the filter size is 3 x 3, yielding an output feature map of dimensions 5 x 5 [4].

The essence of the convolution operation lies in a sliding dot product mechanism. As the filter traverses the input image, a dot product computation occurs, treating both the filter and the covered image region as vectors. This process is visually illustrated in Figure 2.1, showcasing the convolution operation on a simplified, single-channel input. The resultant feature map post-convolution possesses a depth equal to the number of filters utilized and dimensions given by $(n - f + 1) \times (n - f + 1)$.

Activation Layers: The role of an activation layer is to introduce non-linear capabilities into the Convolutional Neural Network (CNN). It receives the output from a convolutional layer and applies a non-linear function to these inputs. This non-linearity is crucial as it allows the CNN to capture complex patterns and relationships in the data, going beyond what linear operations can achieve.

Among the various activation functions, two are particularly prevalent. The sigmoid function, denoted as $\sigma(z)$, is expressed as $\sigma(z) = \frac{1}{1+e^{-z}}$. This function maps any input to a value between 0 and 1, making it especially useful for models where output interpretation as a probability is beneficial. On the other hand, the Rectified Linear Unit (ReLU) function,

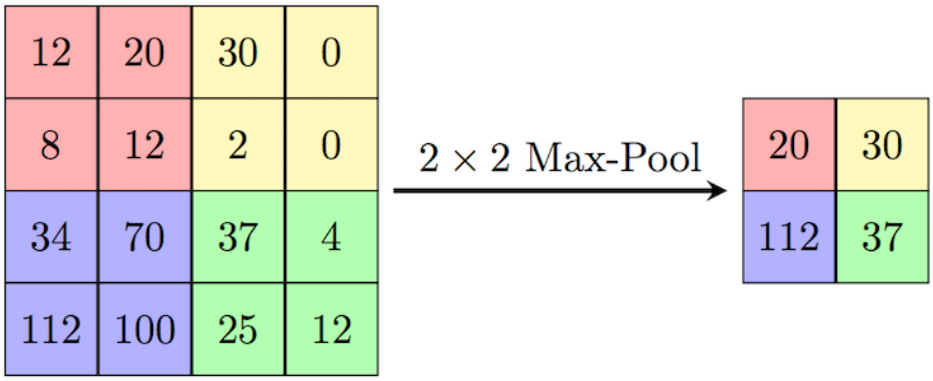

Figure 2.2: Illustration of reducing the dimensions of a feature map using 2 x 2 max pooling [5].

represented by $R(z)$, is defined as $R(z) = \max(0, z)$. ReLU has gained popularity due to its computational efficiency and the ability to mitigate the vanishing gradient problem often encountered in deep networks [27].

Pooling Layers: Pooling layers are integrated into CNNs following the convolutional and activation layers. The purpose of these layers is to infuse the network with robustness to minor positional changes and variations within the input. This is achieved by downsampling the output feature maps from preceding layers, which fosters local translation invariance and concurrently diminishes the computational demand for the layers that follow.

Max pooling stands out as a commonly used pooling technique. In this approach, the principal idea is to traverse the feature map with a defined window and stride, and at each step, select the maximum value within the window. This process effectively distills the most salient feature within the observed region of the feature map, thereby capturing the most critical aspects and discarding the rest. The operation of max pooling is visually depicted in Figure 2.2, providing a clear example of how this technique condenses the information in the feature map while maintaining the most prominent features [28].

Fully Connected Layers: The Fully Connected (FC) or dense layers come into play

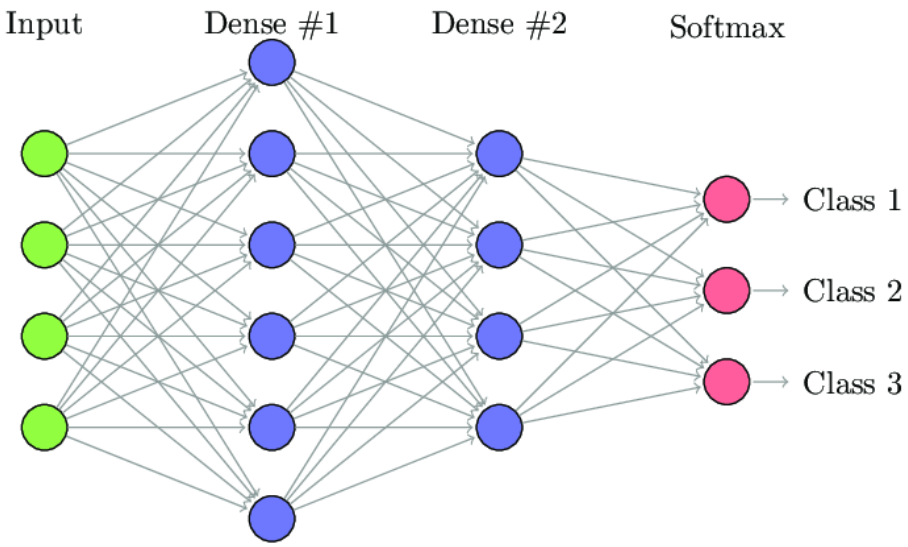

Figure 2.3: Representation of fully connected layers [6]. The input, after being flattened, passes through 3 FC layers. The final layer utilizes a softmax activation function to yield probabilities for each class.

after the convolutional and pooling layers have completed the feature extraction phase. These layers are instrumental in interpreting the features extracted previously and mapping them to specific categories in the context of the classification task [28]. The data flowing from the preceding convolutional or pooling layer is transformed into a one-dimensional array, forming the input for the FC layers. Within these layers, a comprehensive network of connections is established, wherein each neuron (or activation unit) is linked to every neuron in the layer that follows, creating a densely interconnected structure. The culmination of these layers is typically marked by an FC layer that contains a number of neurons equivalent to the number of classes in the classification problem at hand. Subsequently, a softmax activation function is applied, effectively translating the output into a set of probabilities. These probabilities signify the likelihood of the input being categorized into each class, a process illustrated in Figure 2.3.

2.1.2 The VGG16

The VGG16, a distinctive CNN architecture, has demonstrated its prowess in handling TPC data [19]. This robust neural network boasts an extensive array of over 130 million parameters. Its capabilities were recognized globally when it clinched victory in the ImageNet competition in 2014, cementing its status as a premier choice for image classification tasks.

Figure 2.4 provides a schematic representation of the VGG16 structure. The architecture encompasses 16 weighted layers – 13 of these are convolutional layers, while the remaining 3 are fully connected layers. In the convolutional segments, ReLU activations are utilized, a strategic choice inspired by ReLU's effectiveness in mitigating the vanishing gradient dilemma, a prevalent issue with other activation functions such as the sigmoid. The VGG16 is designed to handle 224 x 224 x 3 dimension RGB images. It introduces a padding of one pixel preceding each convolutional layer, a design nuance that not only preserves the spatial dimensions of the image post-convolution – thereby facilitating the construction of a deeper network – but also boosts the network's efficacy by ensuring comprehensive weighting of the image borders. The network's architecture proceeds with the integration of max pooling layers, strategically placed to downsample the feature maps obtained from convolutional and activation stages. The culmination of the VGG16's architecture is marked by a trio of fully connected layers, with the final layer employing a softmax activation function, which allows the network to perform classification tasks [25].

2.1.3 Fine-Tuning

The technique of fine-tuning is employed to harness and augment the capabilities inherent in the VGG16 architecture. Fine-tuning is a form of transfer learning that involves adapting

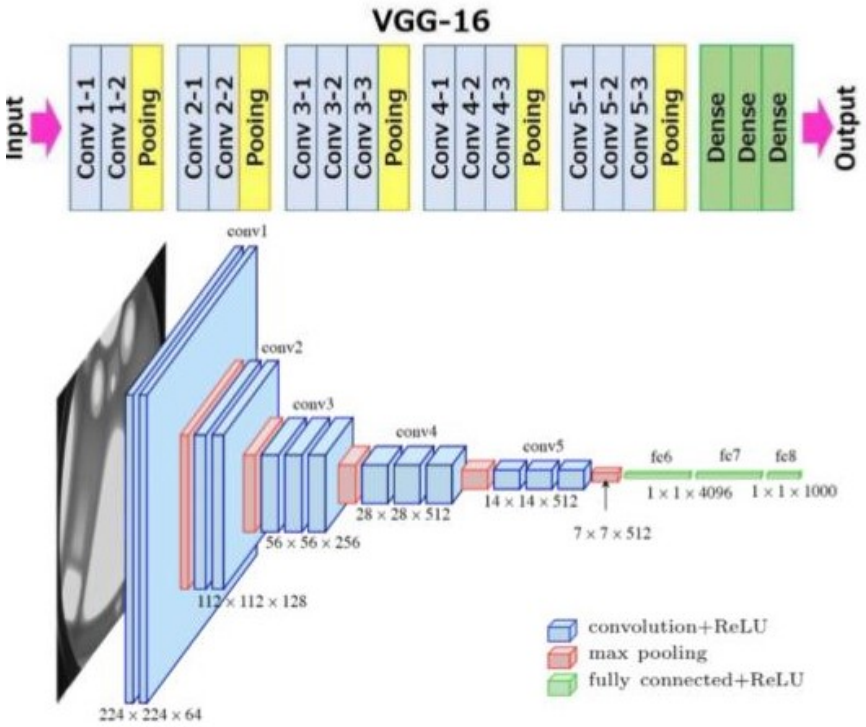

Figure 2.4: A depiction of the VGG16 architecture, illustrating the orderly sequence of layers from the initial input to the final output [7]. The upper segment of the Figure elucidates the journey from the raw input through a series of convolutional and pooling layers. The lower segment visualizes the transformation of an input image as it traverses through the network, delineating the evolution in dimensions and depth of the feature maps at various junctures.

a pre-trained model to undertake a new, albeit related, task [29].

In executing this strategy, we start by preserving the weights of the pre-trained model's initial layers, thereby capitalizing on the network's proficiency in feature extraction. This approach not only streamlines the training procedure but also safeguards the fundamental insights already encoded within the network's structure. Subsequently, we integrate a custom classifier for our specific dataset. This classifier is structured with three fully connected layers, each initialized with random weights, and culminates in a final layer that contains a number of nodes equivalent to the distinct categories in our classification task. During the phases of training and validation, the focus is on adjusting only the weights associated with this newly introduced classifier. It's noteworthy that our experimental findings revealed that retraining the entirety of the network's weights did not lead to a marked enhancement in performance. Instead, it incurred a significant escalation in the duration of the training process. This observation further reinforces the practicality and efficacy of the fine-tuning methodology.

2.2 Strategies for Optimal Model Training

Mastering the art of CNN-based detection in extensive datasets, particularly when dealing with the challenge of identifying rare events, necessitates a nuanced and precise approach. The realm of TPC data perfectly encapsulates this challenge, presenting a highly imbalanced dataset where events of interest can be notably scarce (see Chap. 7 for more details). Attaining peak performance from a model in such conditions is contingent upon various critical factors. Paramount among these is the careful selection of hyperparameters, which profoundly impact the model's performance. This is especially true given the vulnerability

of CNNs to overfitting, a risk that becomes markedly acute when dealing with sparsely occurring target events. In such cases, the model might exhibit remarkable accuracy on the training data but falter in its ability to generalize to new, unseen datasets.

To deal with these complexities, adopting a comprehensive approach to model training is indispensable. This involves meticulous efforts in data preparation, strategic data splitting, the deployment of regularization strategies, and the careful choice of a loss function. Particularly in the context of the significant imbalance characteristic of TPC data, employing strategies such as class reweighting, oversampling, and undersampling is not merely beneficial but imperative. These methods are instrumental in ensuring that the model retains its sensitivity towards sought after rare events while bolstering its resilience against false positives. Additionally, the incorporation of advanced methodologies, like active learning, serves to further refine the model. Through an iterative process, active learning progressively enriches the training dataset, guaranteeing the thorough capture and precise classification of each rare event. This section delves into these methodologies, shedding light on how each one significantly contributes to the ultimate goal of accurately detecting rare events with the utmost precision.

2.2.1 Training, Validation, and Testing Splits

To effectively train a CNN model, one must first hand-label a substantial number of images. This carefully annotated dataset can then be strategically segmented into three distinct subsets: training, validation, and testing. Such segmentation is a cornerstone in the edifice of robust model development. The **Training Set** will typically encompass 80% of the labeled dataset, and serves as the primary learning source for the model. Through iterative exposure to this dataset, the model fine-tunes its internal parameters, like weights and biases, aiming

to diminish the disparity between its predictions and the actual labels.

The **Validation Set**, typically representing 10% of the data, functions as a pivotal checkpoint within the training regime. Subsequent to each training epoch (an entire cycle through the training data) the model's performance is assessed against this validation set. This phase is crucial, not for further training of the model, but to evaluate its efficacy on unseen data. Insights gleaned from the validation set performance are instrumental in fine-tuning the model's hyperparameters. In essence, while the training set enables the model to learn, the validation set serves as a check of the model's capabilities, guiding us in optimizing its configuration.

Finally, the **Testing Set**, often comprising 10% of the data, is safeguarded for the final phase of the training process. This subset provides an unbiased assessment, offering a genuine metric of the model's potential performance in real-world settings. The employment of this tripartite data split orchestrates a holistic training approach, delicately balancing the model's learning phase with the imperative need for thorough evaluation and fine-tuning.

2.2.2 Loss Function

Central to assessing a model's predictive accuracy is the loss function, also known as the cost or objective function. This function quantifies the disparity between the model's predictions and the actual data. A smaller loss function value is indicative of a higher degree of congruence between the predicted outcomes and the true labels. In the context of our classification challenge, we opt for the **Cross-Entropy Loss** as the metric of choice. This choice is particularly apt for scenarios involving classification [30].

In binary classification contexts, where the true label is denoted as y and the predicted

probability as p, the cross-entropy loss is articulated as follows:

$$L(y, p) = -y \log(p) - (1 - y) \log(1 - p) \tag{2.1}$$

For scenarios encompassing multi-class classification, the expression for cross-entropy loss evolves to accommodate multiple classes, as illustrated below:

$$L(y, p) = -\sum_{i=1}^{C} y_i \log(p_i) \tag{2.2}$$

Here, C symbolizes the total number of classes, y_i denotes the actual label for class i (which could be either 0 or 1), and p_i signifies the predicted probability that a given sample falls within class i.

The guiding aim during the model's training phase is the minimization of this loss function. Achieving a lower value for the loss function is tantamount to ensuring that the model's predictions are in closer harmony with the true labels, thus enhancing the model's predictive precision.

2.2.3 Optimization and Learning Rate

The optimization process is akin to the navigator of the model's training journey, guiding the model towards the apex of performance amidst a complex terrain of potential outcomes. This journey involves the methodical refinement of the model's parameters to curtail the loss function. In this pursuit, we use the **Stochastic Gradient Descent (SGD)** optimizer [31], a method celebrated for its efficacy. SGD updates the model's weights incrementally, utilizing subsets of data, thereby enhancing the efficiency of the optimization process. It

computes the gradient of the loss function in relation to each parameter and nudges the weights towards a direction that diminishes the loss. The extent of these parameter updates is modulated by the learning rate, a pivotal hyperparameter that dictates the step size in the optimization journey (an initial learning rate set to 0.001 is often a good first choice).

To amplify the effectiveness of SGD, we infuse the process with momentum (often assigned a value of 0.9). Momentum serves as a strategic tool, enabling the optimizer to deftly traverse local minima and sidestep potential stagnation points by factoring in past gradients. It introduces a velocity component, bolstering the optimizer's descent in directions of sustained gradient and mitigating the propensity for oscillatory movements.

Moreover, to ascertain that the learning rate is consistently fine-tuned throughout the training voyage, we deploy a learning rate scheduler equipped with a patience parameter (usually set to 4). Patience here delineates the count of epochs the scheduler patiently observes before adjusting learning rate, contingent on the absence of performance enhancement (as depicted in Figure 2.5). This dynamic adaptation of the learning rate, orchestrated by the scheduler, strikes a balance between expedited convergence and the stability of the training dynamics. It ensures that the model adeptly navigates through the data's intricacies and converges on an optimal solution.

2.2.4 Regularization

When training deep neural networks, one prevalent challenge is overfitting. This phenomenon occurs when a model excels in its performance on the training data but fails to replicate this success on new, unseen data, indicating that the model is memorizing rather than generalizing. To address this issue, we integrate regularization techniques into our training methodology.

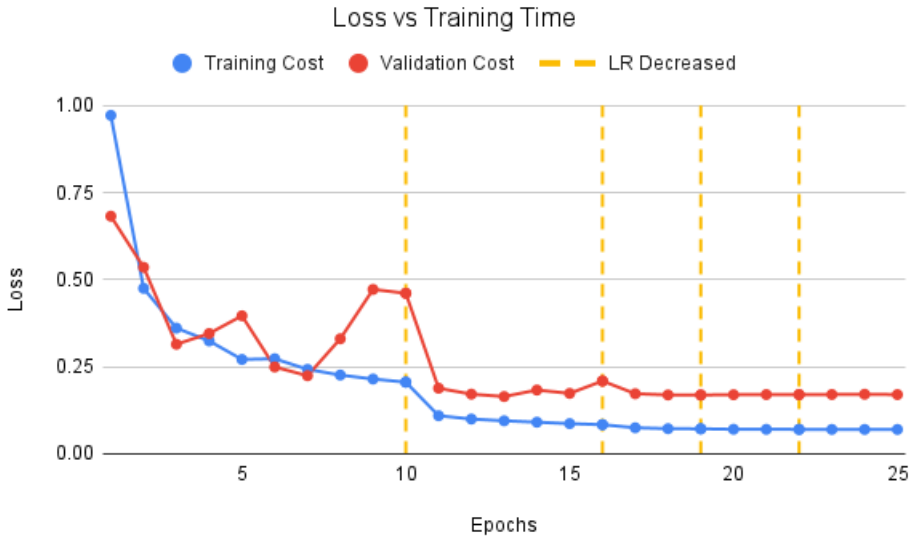

Figure 2.5: Depiction of the learning curve, illustrating the evolution of the model's loss on the training set (in blue) and the validation set (in red) across epochs. The epochs where the learning rate underwent a decrement by an order of magnitude are marked by the yellow dashed lines.

There are many techniques for combating overfitting that we will look to explore in subsequent studies, such as the use of sparse neural networks, inspired by the lottery ticket hypothesis [32]. However, our current approach harnesses the strengths of L2 regularization [33], a strategy designed to prevent the model from becoming overly complex, a common precursor to overfitting. L2 regularization introduces a penalty term to the original loss function. This term is directly proportional to the sum of the squares of the model's weights, inherently promoting smaller weight values. The mathematical representation of the L2 regularization term is given as:

$$L2 = \lambda \sum_{i} w_i^2 \tag{2.3}$$

In this expression, λ symbolizes the regularization strength, a hyperparameter that can be fine-tuned, while w_i denotes the individual weights of the model. By judiciously adjusting λ, we are able to navigate the balance between fitting the training data closely and maintaining

modest weight values to enhance the model's ability to generalize effectively.

Chapter 3

Motivation for Measuring the ^{15}O(α, γ)^{19}Ne Reaction

3.1 X-ray Bursts from Neutron Stars

Binary star systems, where two stars are gravitationally bound, are common throughout the cosmos. When a close binary system includes a neutron star and a hydrogen-rich companion, this can lead to phenomena such as Type I X-ray bursts. These bursts are a result of thermonuclear explosions on the surface of neutron stars and are a topic of active investigation in the nuclear astrophysics community.

Consider a binary system where a neutron star, typically with a mass of $\gtrapprox 1.4 M_\odot$ and a radius between 10 to 15 km, orbits in tandem with a companion star of mass $\lessapprox 1.5 M_\odot$. The neutron star, with its extreme density on the order of 10^{14}g/cm^3, acts as a gravitational sink, pulling material from its partner star [9].

The structure of such a system is defined by Roche lobes, which are regions around each star where their respective gravitational pulls are dominant (see Figure 3.1). Material transfer occurs when the companion star fills its Roche lobe and matter spills over through the inner Lagrangian point onto the neutron star, leading to a series of nuclear reactions on the neutron star's surface [34].

As the accreted hydrogen undergoes fusion, it forms helium, which eventually ignites in

a helium flash via the triple-α process, as detailed in Section 3.2.1. This ignition is the spark that triggers the X-ray burst, a brilliant and rapid increase in X-ray luminosity, which can be observed from Earth through the use of space-based telescopes [35]. The nature of these emissions can vary depending on the mass of the companion star and the magnetic field strength of the neutron star, with some systems exhibiting X-ray pulsations due to the alignment of the magnetic and rotational axes [9].

Following the initial flash, the process continues through the hot Carbon-Nitrogen-Oxygen (CNO) cycles (detailed in the next section) and the rp-process, with temperatures reaching upwards of 10^9 K. Despite this intense nuclear activity, it is posited that the strong gravitational field of the neutron star prevents the newly synthesized elements from escaping, thereby exerting a negligible influence on the galactic chemical composition. However, there is evidence that a small fraction of the mass envelope can escape via radiation driven winds [36]. Regardless, the bursts themselves are invaluable for probing the physical characteristics of neutron stars, such as mass, radius, and surface composition [9].

3.1.1 Hot-CNO cycles and Breakout

The CNO cycle is a cornerstone of stellar nucleosynthesis, particularly in stars with masses exceeding $1.3M_{\odot}$, where it serves as the primary mechanism for energy generation through the fusion of hydrogen into helium. This process is facilitated by a sequence of proton captures and β-decays involving CNO isotopes, with the cycle's rate constrained by the slower proton capture reactions compared to β-decays [9].

During a Type I X-ray burst, the scenario changes drastically as the thermonuclear temperatures rise, causing an acceleration in the reaction rates of the CNO cycle. This results in the Hot CNO (HCNO) cycle, where the proton captures start occurring much more

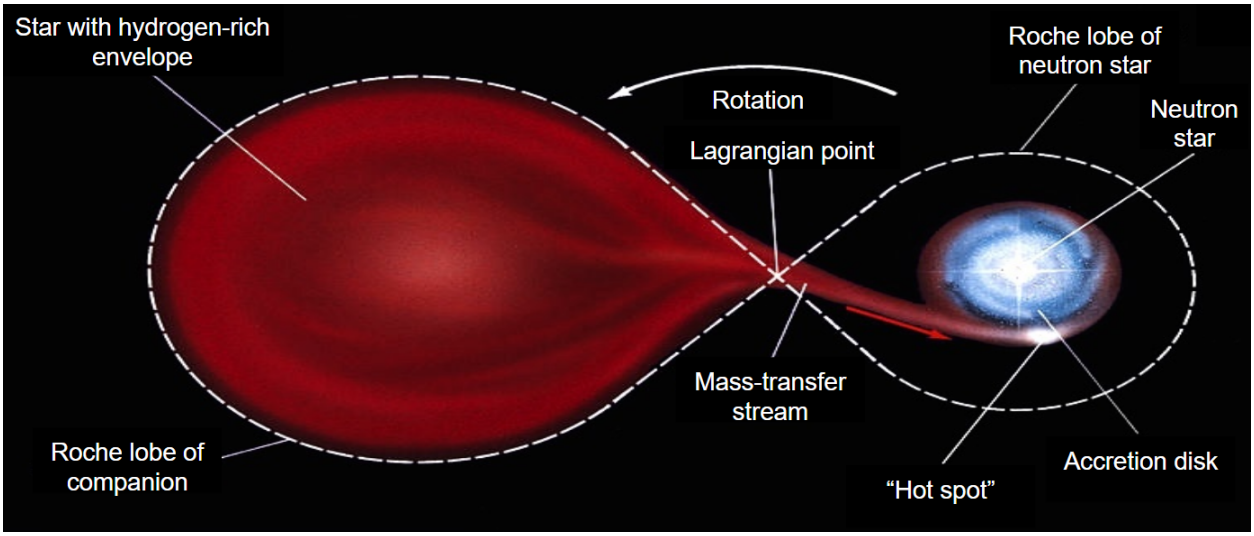

Figure 3.1: Illustration of a binary star system comprising a neutron star and a hydrogen-rich companion, each enclosed by their respective Roche lobes. The inner Lagrangian point, where gravitational forces and rotational effects equilibrate, facilitates mass transfer from the companion star to the neutron star. Adapted from [8].

rapidly than the β-decays, which are temperature independent (Figure 3.2 illustrates these cycles). The HCNO cycles are particularly dominant in energy generation at temperatures ranging from 0.1 to 0.4 GK in environments rich in CNO nuclei. The rate at which energy is generated in these cycles is influenced by the concentration of the catalysts, namely the CNOF nuclei [9].

The HCNO cycles, such as HCNO1, involve isotopes like ^{14}O and ^{15}O, which have β-decay half-lives of 70.62 seconds and 122.24 seconds, respectively. These half-lives are significantly longer than the near-instantaneous proton captures and (p, α) reactions occurring in these cycles. Consequently, the extended β-decay lifetimes of these isotopes present a barrier to the synthesis of heavier elements within the duration of a typical Type I X-ray burst.

However, at temperatures exceeding 0.5 GK, novel pathways for element synthesis become accessible, facilitating the creation of elements with atomic mass numbers exceeding 20. Among these, the breakout reaction $^{15}\mathrm{O}(\alpha,\gamma)^{19}\mathrm{Ne}(p,\alpha)^{20}\mathrm{Na}$ plays a pivotal role. The

sequence's initial step, $^{15}\mathrm{O}(\alpha,\gamma)^{19}\mathrm{Ne}$, stands out as a critical reaction rate for the accurate modeling of X-ray burst light curves. Its significance stems from its role in initiating the HCNO cycle breakout at elevated temperatures, serving as a critical bottleneck for the breakout process. The exploration of this reaction is essential for understanding the intricate processes of nucleosynthesis, and energy generation mechanisms during these Type I X-ray bursts [11].

3.2 Mathematical Framework of Reaction Rates

Nuclear reactions in stars, particularly those of lower temperatures like our Sun, predominantly involve nuclei in their lowest-energy, stable configurations, known as ground states (X). The probability of such reactions depends on three fundamental parameters: the abundance of the reacting nuclei; their relative velocity; and the cross-section, σ. The cross-section quantifies the reaction probability between two nuclei and can be extracted from empirical data through the observed reaction rate, R, which follows the relationship:

$$R = \sigma I_a N \tag{3.1}$$

where I_a denotes the flux of incoming particles and N represents the density of target nuclei per unit area.

In high-temperature, explosive stellar environments like supernovae or X-ray bursts, nuclear reactions are not limited to ground states. Nuclei are often excited to higher energy levels (X^*), opening up additional reaction pathways. Excitation can occur through two primary mechanisms: gamma-ray absorption ($X + \gamma \rightarrow X^*$), where a nucleus absorbs a

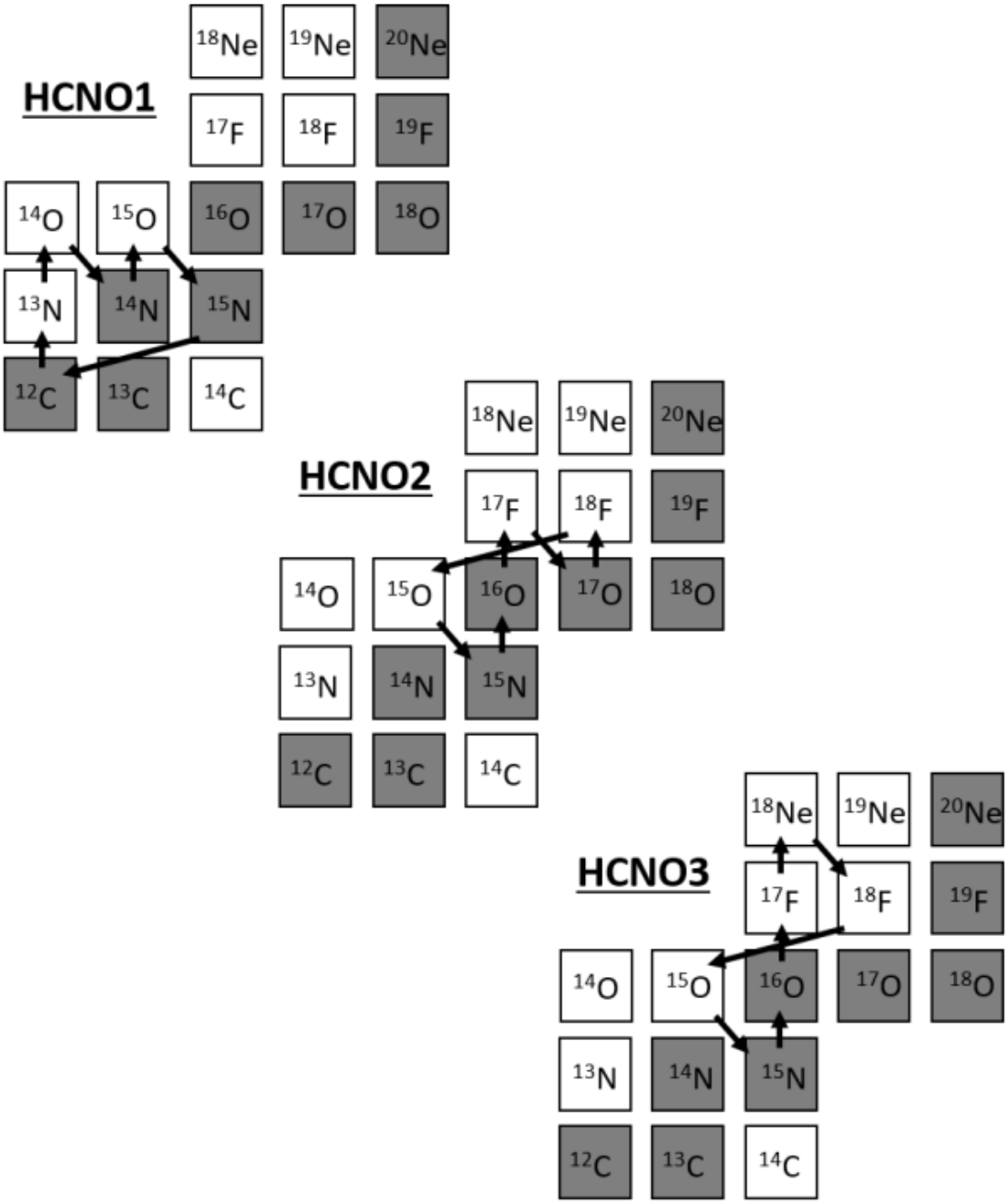

Figure 3.2: Illustration of the three Hot CNO cycles operative during Type I X-ray bursts. Each cycle effectively fuses four protons into one He nucleus. Stable isotopes are denoted by gray boxes, while the arrows indicate the flow of reactions and β-decays within the cycles. Adapted from [9].

high-energy photon, and inelastic scattering ($X(a, a')X^*$), a process in which a nucleus collides with another particle, resulting in energy redistribution.

The role of these excitation mechanisms in stellar nucleosynthesis is profound. They enable reactions that are otherwise forbidden in ground state nuclei, altering the dynamics of nuclear synthesis. In environments typified by rapid, intense thermonuclear reactions like Type I X-ray bursts, including these additional channels is essential for accurate astrophysical modeling.

Expanding on the mathematical depiction of reaction rates, we consider:

$$R_{12} = N_1 N_2 \langle v\sigma \rangle, \tag{3.2}$$

where N_1 and N_2 are the number densities of the interacting nuclei, and v is their relative velocity. The term $\sigma(v)$ represents the energy-dependent reaction cross-section, with $\langle v\sigma \rangle$ indicating an average, given the continuous velocity distribution in stellar contexts.

The reaction cross-section, $\sigma(v)$, is a function that is characterized by several components: a geometric term related to the projectile's de Broglie wavelength ($\pi\lambda_p^2$, where $\lambda_p = \sqrt{\frac{h}{2mE}}$), the quantum mechanical interaction matrix element ($M = \langle f|H|i\rangle$, where i and f delineate the wave functions of the initial and final states), and the penetrability factor ($P_l(E)$, where E is the energy of the projectile), which assesses the likelihood to penetrate the potential barrier of the target nucleus, with significant reductions due to the Coulomb and angular momentum barriers. Incorporating these insights, the cross-section can be formulated as:

$$\sigma \propto \pi\lambda_p^2 \cdot |\langle f|H|i\rangle|^2 \cdot P_l(E). \tag{3.3}$$

At temperatures relevant to astrophysical phenomena, $P_l(E)$ is dominated by the $l = 0$ (s-wave) term, and can be expressed as an exponential function dependent only on the Sommerfeld parameter η, which is a dimensionless quantity encapsulating the essence of the Coulomb interaction between the colliding nuclei. This is expressed as

$$P_l(E) \propto e^{-2\pi\eta}, \quad \text{where} \quad \eta = \frac{Z_1 Z_2 e^2}{\hbar}\sqrt{\frac{\mu}{2E}}. \tag{3.4}$$

Here, Z_1 and Z_2 represent the atomic numbers of the target and projectile nuclei, respectively. The symbol e stands for the elementary charge, $\hbar$ is the reduced Planck's constant, and μ is the reduced mass of the system.

The astrophysical environments of interest are characterized by non-relativistic velocities and thermal equilibrium, and as such can be described using the Maxwell-Boltzmann distribution for velocities:

$$f(v) = 4\pi \left(\frac{\mu}{2\pi kT}\right)^{\frac{3}{2}} v^2 e^{-\frac{\mu v^2}{2kT}} \tag{3.5}$$

where k is the Boltzmann constant, and T is the temperature of the environment. Substituting this distribution into our reaction rate equation yields:

$$R_{12} = 4\pi N_1 N_2 \left(\frac{\mu}{2\pi kT}\right)^{\frac{3}{2}} \int_0^\infty v^3 \sigma(v) e^{-\frac{\mu v^2}{2kT}} dv \tag{3.6}$$

Transitioning to the center-of-mass energy framework, we can express the average rate per particle pair as:

$$\langle \sigma v \rangle_{12} = \frac{R_{12}}{N_1 N_2}\sqrt{\frac{8}{\pi\mu}}\frac{1}{(kT)^{\frac{3}{2}}} \int_0^\infty E\sigma(E) e^{-\frac{E}{kT}} dE \tag{3.7}$$

The derivation of the reaction rate given above, reveals the distinct contributions of the cross section, $\sigma(E)$, and the kinetic energy of the particles, E, to the nuclear reaction rate. In thermonuclear environments, the cross-section for rapid proton capture displays a unique energy dependency, which can be expressed as:

$$\sigma(E) \propto e^{\sqrt{E}}. \tag{3.8}$$

This equation highlights the cross-section's sensitivity to particle energy, especially at low energies where the Coulomb barrier plays a significant role.

The high energy tail of the Maxwell-Boltzmann distribution suggests that higher energies are exponentially less probable. The convolution of this distribution with the penetrability factor is graphically presented in Figure 3.3, delineating the probability of nuclear reactions as a function of energy. This convolution culminates in the Gamow window—a pronounced peak in the probability distribution signifying the optimal conditions for charged-particle reactions and hence, thermonuclear burning. The Gamow window marks the energy range where a substantial fraction of nuclei have enough energy to overcome the Coulomb barrier, thereby enabling fusion reactions [10, 11].

For experimental physicists, the Gamow window provides a targeted energy range for designing nuclear reaction experiments. However, it's not the sole factor to consider. Resonance reactions, which occur when the kinetic energy of the nuclei aligns with a resonance state, can also amplify reaction rates substantially, echoing the kinetic energy considerations seen in the Gamow window. These resonances are pivotal in nuclear astrophysics, as they can lead to significant enhancements in reaction rates.

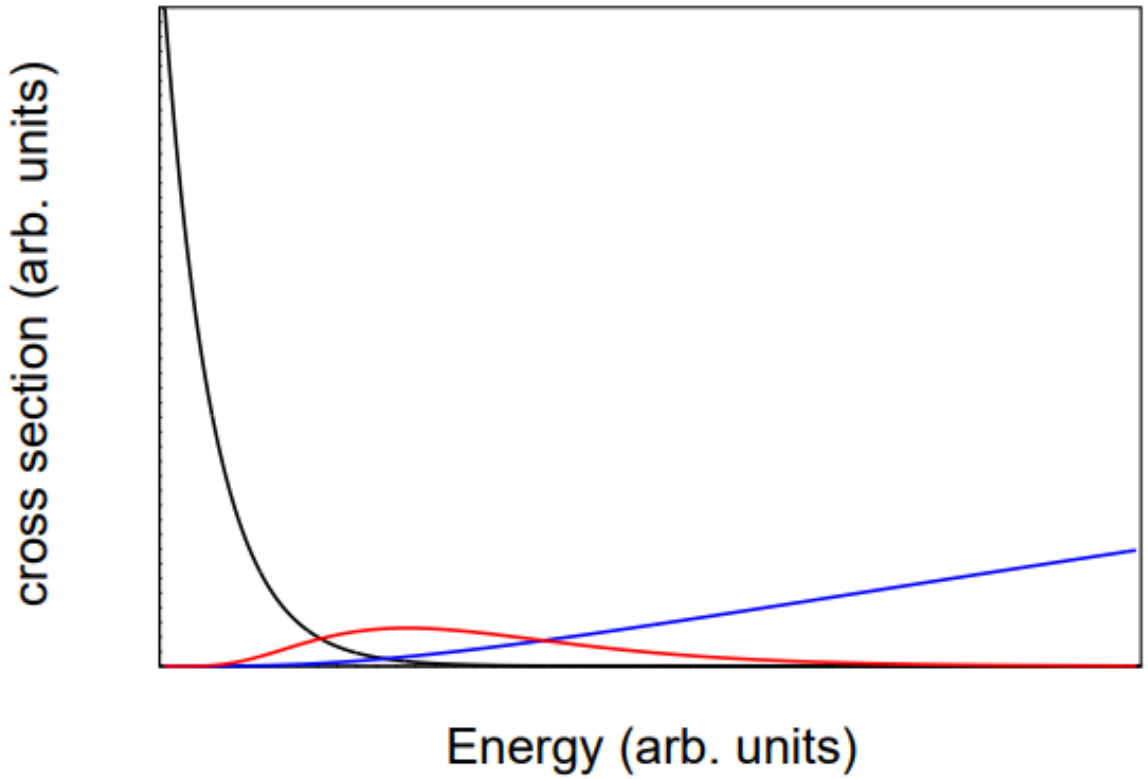

Figure 3.3: The Gamow window, illustrated in red, arises from the convolution of the Maxwell-Boltzmann distribution (in black) with the penetrability factor $P_l(E)$ (in blue). For visual clarity, the peak of the Gamow window has been enhanced by a factor of 100. Adapted from [10].

3.2.1 Dynamics of Direct and Resonant Nuclear Capture

Direct and resonant nuclear capture are crucial for stellar nucleosynthesis, significantly contributing to the formation of new elements and energy generation in stars. These processes influence the life cycle and evolution of stars, and play a pivotal role in phenomena like X-ray bursts.

In direct nuclear capture, a charged particle is rapidly absorbed by a nucleus, forming a new element or isotope. This process adheres to the principle of mass-energy equivalence, resulting in the release of energy (ΔE) in the form of gamma radiation. The energy release is described by the equation $\Delta E = (\text{mass of reactants} - \text{mass of product nucleus}) \times c^2$. A critical aspect of direct capture is the separation energy, which is the minimum energy required to remove a particle from a nucleus. The value of this separation energy varies depending on the type of particle and the specific nucleus involved, influencing the probability of forming a bound state in different nuclear capture scenarios.

Resonant nuclear capture, in contrast, occurs when the center of mass energy of the reactants is near one of the excited energy states of the resulting compound nucleus. This phenomenon is characterized by distinctive peaks in the reaction cross-section at resonant energies. A well known example of resonant capture is the triple-alpha process, which is essential for carbon production in stars [37]. In this process, two alpha particles combine to form unstable ^8Be, which can capture another alpha particle to form ^{12}C. This resonant capture to the Hoyle state, an excited state in ^{12}C at 7.7 MeV, results in the formation of carbon, bypassing the gap in stability for nuclei with 5 or 8 nucleons. The decay probabilities of this excited state are related to the partial widths Γ_γ and Γ_α, where the total width is $\Gamma = \Gamma_\gamma + \Gamma_\alpha$, and the probabilities of gamma decay or alpha particle re-emission are given by

the branching ratios Γ_γ/Γ and Γ_α/Γ, respectively.

The resonant capture cross-section $\sigma(E)$ is described by the Breit-Wigner formula:

$$\sigma(E) = \frac{\lambda^2}{4\pi}\frac{\omega\Gamma_1\Gamma_2}{(E-E_r)^2+(\Gamma/2)^2}, \quad \omega = \frac{2J_r+1}{(2J_a+1)(2J_b+1)}, \tag{3.9}$$

where λ represents the DeBroglie wavelength of the incoming projectile, Γ_1 and Γ_2 denote the partial widths corresponding to the two decay modes, E and E_r signify the center of mass energy and the resonance energy, respectively, and J_a, J_b, and J_r are the spin quantum numbers of the reacting and resultant nuclei.

In the context of the $^{15}O(\alpha,\gamma)^{19}Ne$ reaction, the key resonance of interest is narrow and isolated ($\Gamma \ll E_r$). This means that the reaction rate is highly sensitive to the energy of the incoming alpha particle and happens most effectively when the energy of the alpha closely matches the resonance energy of the ^{19}Ne nucleus. In this case, the resonance reaction rate simplifies to:

$$\langle\sigma v\rangle = \left(\frac{2\pi}{kT\mu}\right)^{3/2}\hbar^2 e^{-E_r/kT}\omega\gamma, \tag{3.10}$$

where γ is

$$\gamma = \frac{\Gamma_1\Gamma_2}{\Gamma}. \tag{3.11}$$

When the resonance energy (E_r) and the temperature (T) are known, all factors in this equation 3.10 become constants except for the resonance strength $\omega\gamma$. This simplification allows experimentalists to measure the branching ratios of specific decay channels from an astrophysical resonance, in addition to the spins and lifetimes of the relevant states, to construct the reaction rate. This approach is invaluable, especially when direct measurement of the cross section of a resonant reaction is challenging or impossible, which is often the

case when one of the reactants is unstable.

3.3 The ^{15}O(α, γ)^{19}Ne Reaction

The shape of the light curve in Type I X-ray bursts from neutron stars can potentially unveil critical attributes of neutron stars, such as their mass, radius, and crust elemental abundance. To extract this information, it's imperative to simulate these light curves and juxtapose them with empirical data. However, the accuracy of these simulations is compromised by uncertainties in nuclear reaction rates, which can markedly alter the simulated light curve profiles.

Sensitivity studies underscore the pivotal role of the ^{15}O(α, γ)^{19}Ne reaction, especially at breakout temperatures of $\approx$0.5 GK (see Figure 3.4). This reaction emerges as one of the most important reaction rate uncertainties that needs to be determined to refine the modeling of X-ray burst light curves. Furthermore, the significance of the ^{15}O(α, γ)^{19}Ne reaction extends to burst ashes, as it is ranked among the top reactions affecting the ashes in multi-zone models [11, 38].

While some contemporary models, based on Cyburt's 2016 comprehensive paper, suggest other reactions might hold equal or greater importance, the prominence of the ^{15}O reaction remains widely agreed upon. The neutron star's continuous fusion of hydrogen into helium culminates in a helium ignition, instigating a thermonuclear runaway. This explosive burning phase, often termed the helium flash, amplifies hydrogen burning, elevating temperatures and accelerating the hydrogen burning rate, thereby propelling the system into the hot-CNO cycle.

As this beta-limited cycle iterates, temperatures escalate, eventually reaching the thresh-

old (0.5 GK) that permits the onset of breakout reactions. At these elevated temperatures, ^{15}O captures an α particle, yielding ^{19}Ne, paving the way for nucleosynthesis that can extend up to mass number 100 via the rp process [35, 12].

A direct measurement of the ^{15}O(α, γ)^{19}Ne reaction is not currently possible due to the absence of high-intensity radioactive ^{15}O beams. Fortunately, the reaction rate is anticipated to be dominated by a single resonance corresponding to the 4.03 MeV state in ^{19}Ne. With the spin [39] and lifetime [40, 41, 42] of this state already established, the focus narrows down to determining the α particle branching ratio (Γ_α/Γ), which represents the fraction of decays via α particle emission from this state. Acquiring this branching ratio will unveil the resonance strength, and consequently, the thermonuclear reaction rate.

Reactions that Impact the Burst Light Curve in the Multi-zone X-ray Burst Model

Rank	Reaction
1	^{15}O(α, γ)^{19}Ne
2	^{56}Ni(α, p)^{59}Cu
3	^{59}Cu(p, γ)^{60}Zn
4	^{61}Ga(p, γ)^{62}Ge
5	^{22}Mg(α, p)^{25}Al
6	^{14}O(α, p)^{17}F
7	^{23}Al(p, γ)^{24}Si
8	^{18}Ne(α, p)^{21}Na
9	^{63}Ga(p, γ)^{64}Ge
10	^{19}F(p, α)^{16}O
11	^{12}C(α, γ)^{16}O
12	^{26}Si(α, p)^{29}P
13	^{17}F(α, p)^{20}Ne
14	^{24}Mg(α, γ)^{28}Si
15	^{57}Cu(p, γ)^{58}Zn
16	^{60}Zn(α, p)^{63}Ga
17	^{17}F(p, γ)^{18}Ne
18	^{40}Sc(p, γ)^{41}Ti
19	^{48}Cr(p, γ)^{49}Mn

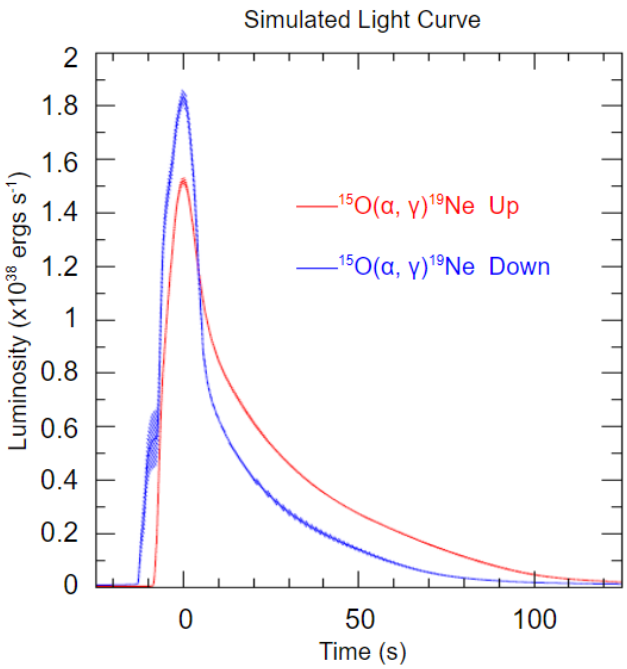

Figure 3.4: Left: Table ranking the sensitivity of light curve models to each of the relevant nuclear reaction rates. Right: Simulated plot of light curve intensity as a function of time using both the upper and lower limit for the ^{15}O(α, γ)^{19}Ne reaction rate [11].

3.3.1 Previous Studies of ^{15}O(α, γ)^{19}Ne

Over the past few decades, accurately measuring the ^{15}O(α, γ)^{19}Ne reaction has become a focal point in nuclear astrophysics research. Various transfer reaction techniques have been employed to populate the 4.03 MeV state in ^{19}Ne, aiming to determine the elusive α branching ratio.

The pioneering transfer reaction $p(^{21}\text{Ne}, ^{3}\text{H})^{19}\text{Ne}^*$ utilized inverse kinematics to produce tritons and ^{19}Ne* [43]. This generated a distinct energy signature when measuring the alpha branch that came from the combination of tritons and the low-energy alphas. Despite minimal background interference, this experiment could only establish an upper limit for Γ_α/Γ at less than 4.3×10^{-4}. Following experiments, such as those by Rehm et al. using $^{3}\text{He}(^{20}\text{Ne}, \alpha)^{19}\text{Ne}^*$ [44], and Tan et al. with $^{19}\text{F}(^{3}\text{He}, t)^{19}\text{Ne}^*$ [45], faced similar challenges. The latter reported an α branching ratio at 1.8 σ significance, but the results are contentious due to uncertainties in background modeling [46].

Other studies have focused on Ne* states above the α separation energy, S_α [47, 48, 49], but these too struggled to detect the α branch from the 4.03 MeV state. The inherent challenges of transfer reactions, including the production of a multitude of byproducts and consequential statistical noise, have consistently impeded the detection of α particles amidst the background. Complications are further exacerbated by the resonance's closeness to the α separation energy and the kinetic energy loss of the α particles, making these measurements particularly complex. Despite these obstacles, the scientific community has been persistently investigating this reaction for over twenty years, primarily employing transfer reactions to probe the 4.03 MeV state in ^{19}Ne. While these methods' substantial background and limited statistical precision pose significant challenges for obtaining definitive measurements, they

have been instrumental in establishing a stringent upper limit on the branching ratio, thereby underscoring the difficulty of accurately measuring this reaction.

3.3.2 Purpose of this Work

Past research by our group led to a significant discovery: the 4.03 MeV state in ^{19}Ne can be populated through the beta-delayed proton decay of ^{20}Mg. This decay sequence results in a distinct signature—the near simultaneous emission of a proton and α particle. This process, as depicted in Figure 3.5, opens a new avenue for accurately measuring the Γ_α/Γ ratio, and consequently, the $^{15}O(\alpha,\gamma)^{19}$Ne reaction rate [12].

Bolstering this method is our prior determination of the proton energy from the excited state in ^{20}Na that feeds the 4.03 MeV state in ^{19}Ne. This was achieved by analyzing the Doppler-broadened 4.03 MeV gamma peak from the recoiling ^{19}Ne nucleus. Through simulations that aligned with observed data, the proton energy was estimated to be $1.21^{+0.25}_{-0.22}$ MeV [17]. This detailed energy profile allows us to define a precise search region in range and energy (see Section 6.3.1), which aids in the filtering out of irrelevant data and focusing on the critical proton-α events.

Employing the GADGET II Time Projection Chamber (TPC) detailed in chapter 4, we capture these elusive proton-α coincidences. The TPC's ability to reconstruct 3D decay events is key to identifying the unique double Bragg peak topology of these proton-α events, ensuring a nearly background-free measurement.

The detection and analysis of these events are expected to lead to the first definitive measurement of the alpha branching ratio from the 4.03 MeV state in ^{19}Ne. This advancement will constrain the $^{15}O(\alpha,\gamma)^{19}$Ne reaction rate and enable us to model X-ray burst light curves from neutron stars far more accurately. Such an achievement would represent

a substantial leap forward in nuclear astrophysics, providing vital insights into neutron star behavior.

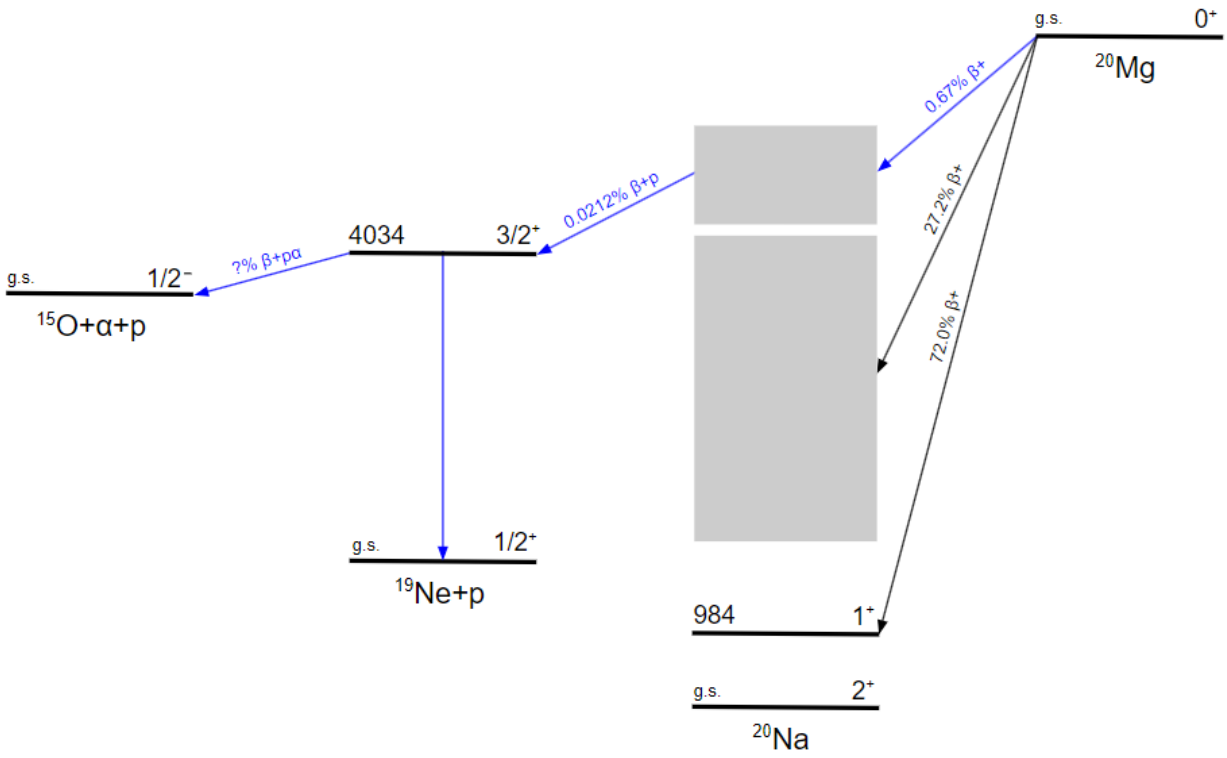

Figure 3.5: Decay sequence of ^{20}Mg illustrating the β-delayed proton emission that populates the 4.03 MeV state in ^{19}Ne. Figure adapted from [12].

Chapter 4

The Time Projection Chamber for GADGET II

The GAseous Detector with GErmanium Tagging (GADGET) was built to detect individual protons emitted after beta decays. However, GADGET is ill-equipped for detecting multiple particle emissions and distinguishing between them. But as we've learned from Chapter 3, the characteristic signature of our events of interest, ^{20}Mg($\beta p\alpha$), is the near simultaneous emission of a roton and alpha particle. To achieve the granularity necessary for the identification of these multi-particle events, we transformed the GADGET Proton Detector into a time projection chamber (TPC), which is the key component of the upgraded GADGET II detection system (the full GADGET II system is described in Section 5.3). This TPC allows for the reconstruction of 3D images of decay events that occur in the active volume of the detector.

The subsequent sections are adapted from our previously published work in collaboration with Mahajan et al. [15]. These adaptations are used with permission and have been modified to fit the context of this thesis.

4.1 Description of TPC

The GADGET II TPC (see Fig 4.1) is a cylindrical gaseous detector that can be thought of as having two distinct regions; a drift region, and proportional amplification region (Figure 4.2 shows a simplified schematic of the TPC). The drift region operates by thermalizing radioactive ions within its gas volume, facilitating the measurement of their subsequent decay. The resulting ionization electrons created from the charged decay products are directed to a readout by a uniform electric field that is tuned to prevent the liberation of any additional charge.

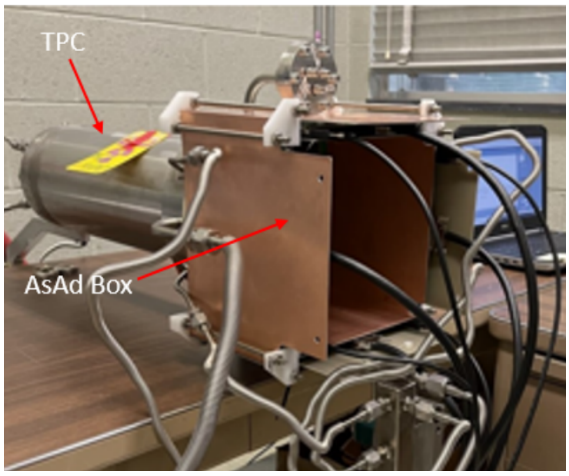

Figure 4.1: The GADGET II TPC in a lab space off the beam line.

The proportional amplification region is characterized by a strong electric field that generates a Townsend avalanche, effectively amplifying event signals (more details in Section 4.1.1). The charge cluster created in this region is collected on a position-sensitive MicroMegas (MM) gaseous amplifier [50]. This MM is notable for its high granularity, featuring 1016 measurement pads, each measuring 2.2×2.2 mm^2, covering an area of 50.24 cm^2. This design marks a substantial enhancement over the original GADGET proton detector, which was equipped with only 5 measurement pads. This high density of pads coupled with precise timing information from arriving electrons allows the GADGET II TPC to perform 3D reconstructions of charged particle tracks.

The operational efficiency of the GADGET II TPC is highlighted by its ability to function in distinct modes that correspond to implant-decay cycles with radioactive beams. During 'beam off' periods, charged particles from decays are detected as they are drifted towards the MM. During 'beam on' periods, the system employs an electrostatic gating grid [12]

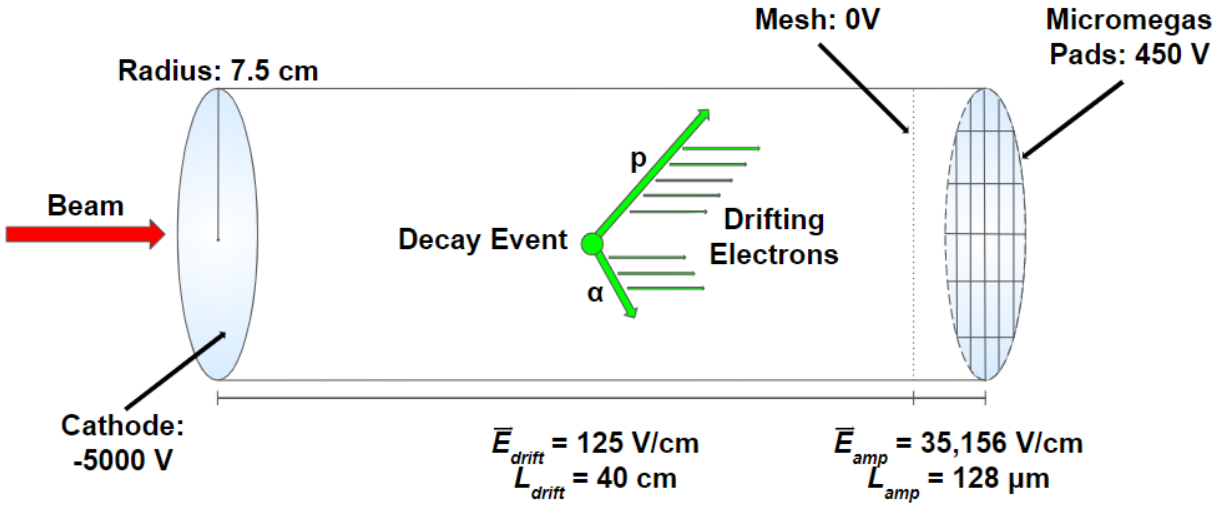

Figure 4.2: Simplified schematic of the GADGET II TPC.

to counteract the intense ionization caused by the beam, which can cause large signals and distort the electric field, thus ensuring accurate detection while minimizing background interference.

The GADGET II TPC's design and functionality enable it to play a crucial role in astrophysical studies, particularly in the identification and analysis of low-energy β-delayed single- and multi-particle emissions. Table 4.1 enumerates some of the TPC's nominal operating parameters, and the following subsections delve into the specifics of the TPC's individual components.

4.1.1 Resistive MICROMEGAS

The GADGET II readout board is a MM that is uniquely designed with a resistive-anode, which is a novel application in the field of low-energy nuclear physics [51]. This resistive MM, which doubles as the detector's gas volume end cap, is a custom-designed component manufactured at CERN. It features a resistivity of 10 MΩ per square, which works to safeguard the front-end electronics [52] from electrical breakdown caused by sporadic discharges.

Additionally, the MM comprises a stainless steel micromesh characterized by an 18 µm wire diameter and a 45 µm micromesh opening. The micromesh, following calendaring, attains a thickness of 30 µm with 45% optical transparency. The micromesh is supported by insulating pillars placed 128 µm above the anode plane and maintained at ground voltage. The Townsend avalanche of electrons occurs across a 128 µm amplification gap between the micromesh and the resistive anode at an electric field strength of approximately 35 kV/cm.

The resistive MM in GADGET II is further characterized by its high-granularity readout plane, which includes 1024 square pads, with 1016 measurement pads covering an area of 50.24 cm^2 and 8 veto pads covering an area of 28.26 cm^2. The readout plane's segmentation ensures effective capture of charged particles, with the veto pads functioning to exclude particles escaping the active volume. The anode forms a circular area with a diameter of 10 cm on a PCB frame, parallel to the micromesh. The resistive anode is layered atop 50 µm of Polyimide, which is bonded to the segmented readout plane using a thin layer of glue. This arrangement forms a two-dimensional RC network, where the resistance is defined by the surface resistivity, R, of the anode, achieved through a uniform layer of diamond-like carbon (DLC). The capacitance, C, is determined by the relative permittivity of the glue and Polyimide. We can model this RC network by utilizing the two dimensional Telegraph equation [53]:

$$\frac{\partial \rho}{\partial t} = h\left[\frac{\partial^2 \rho}{\partial r^2} + \frac{1}{r}\frac{\partial \rho}{\partial r}\right], \tag{4.1}$$

where ρ is the charge density, r is radial position, and $h = \frac{1}{RC}$. In the ideal case we take the resistive anode to have an infinite radius, and at time $t = 0$ we assume there to be a point

charge at the origin. Then the solution for the charge density is given by:

$$\rho(r,t) = \frac{1}{2th} exp(-r^2/4th). \tag{4.2}$$

Using this equation one can find the charge density as a function of radial position for various R and C values. We can also model the amount of charge that will be deposited on each pad, Q_{pad} [54]. We start by writing the Telegraph equation in terms of Cartesian coordinates:

$$\frac{\partial \rho}{\partial t} = h\left[\frac{\partial^2 \rho}{\partial x^2} + \frac{\partial^2 \rho}{\partial y^2}\right]. \tag{4.3}$$

Then, in order to ensure a closed form solution we assume a delta function point charge is collected at the origin at $t = 0$, to get:

$$\rho_\delta(x,y,t) = \left(\frac{1}{2\sqrt{\pi th}}\right)^2 \exp[-(x^2+y^2)/4th]. \tag{4.4}$$

To account for the fact that the actual charge profile is described by a Gaussian, we convolve the above equation with the Gaussian characterizing the charge cluster:

$$\rho(x,y,t) = \frac{Nq_e}{2\pi(2ht+w^2)} \exp[-(x^2+y^2)/(2(2ht+w^2))], \tag{4.5}$$

where N represents the numbers of electrons, q_e is the electron charge, and w is the width of the Gaussian describing the charge cluster. From here we can integrate the charge density

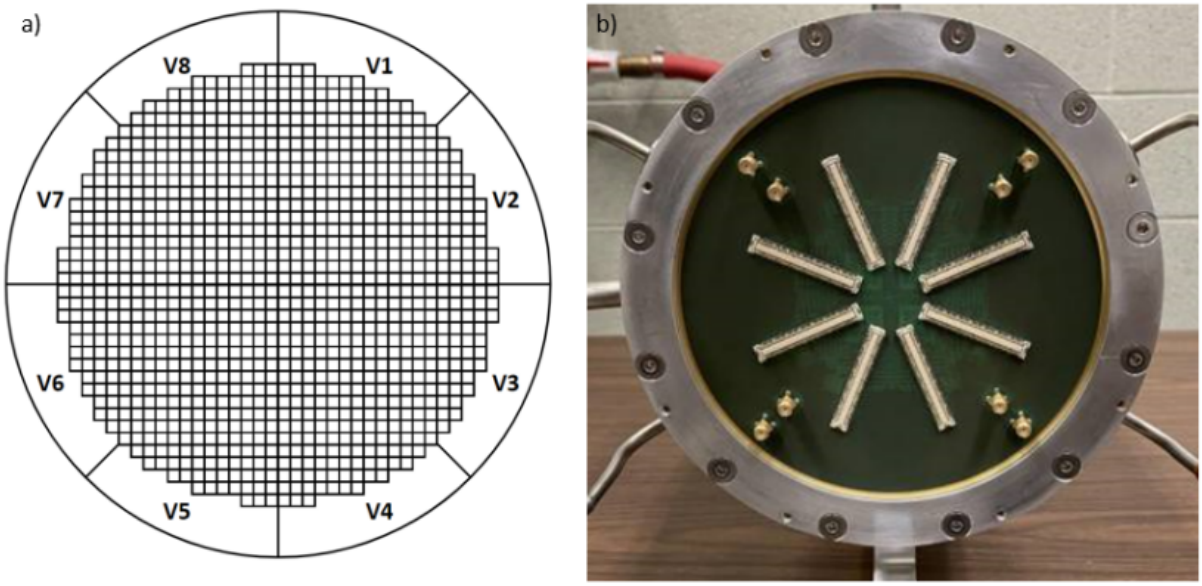

Figure 4.3: a) Schematic of the MM board's front view, illustrating the central region composed of 1016 measurement pads, along with 8 veto pads labeled V1 to V8. b) A view of the MM board's rear end cap, showing 8 multi-pin connectors, each with 144 channels, which are then connected to the T-Zap boards (not depicted).

function over the area of a single pad to get the charge on a pad:

$$Q_{pad}(t) = \frac{Nq_e}{4}\left[erf\left(\frac{x_{high}}{\sqrt{2}\sigma_{xy}}\right) - erf\left(\frac{x_{low}}{\sqrt{2}\sigma_{xy}}\right)\right] \times \left[erf\left(\frac{y_{high}}{\sqrt{2}\sigma_{xy}}\right) - erf\left(\frac{y_{low}}{\sqrt{2}\sigma_{xy}}\right)\right], \quad (4.6)$$

where x_{high}, x_{low}, y_{high}, and y_{low} represent the pad boundaries, and $\sigma_{xy} = \sqrt{2th + w^2}$. This expression for Q_{pad} let's one calculate the charge on a pad for an event of interest. For GADGET II R and C were chosen so as to affect minimal charge dispersion, confining the charge spread to a single pad covering an area of 4.84 mm^2, thereby facilitating precise detection. Figure 4.3 a) and b) show the front and rear view, respectively of the installed MM at one end of the TPC.

4.1.2 The GET System

To handle the high-density of signals from our MM we utilized the GET (Generic Electronics for TPCs) system. This system, specifically developed for gas-filled detectors in nuclear physics, is notable for its scalability and adaptability to various TPC configurations. The GET system's architecture is designed around a versatile ASIC (Application Specific Integrated Circuit), enabling multiple modes of data acquisition tailored for different experimental needs.

Central to the GET system is the AsAd (ASIC and ADC) front-end card, which comprises four AGET chips and ADCs. These chips are responsible for the initial aggregation of data from 64 input channels to a single analog output, a process critical for handling the large amount of data generated by the TPC. To facilitate control and monitoring, the system includes a small Field Programmable Gate Array (FPGA), which oversees the slow control of the chips, while keeping track of parameters like currents, voltages, and temperature.

The CoBo (Concentration Board) can accommodate up to four AsAd boards, and is equipped with an FPGA. The CoBo performs several key functions: configuring the AsAd cards, local calibration, trigger functions, and managing data flow. It also plays a role in time-stamping and formatting functions, contributing to efficient data management and transfer at high speeds. For the GADGET II experiment (E21072) at FRIB (see chapter 4 for more details), a configuration of four CoBos was employed to read out all 1024 channels of the MM, addressing the challenge of data throughput limitations (see Section 5.3.6.1). While a single CoBo is capable of handling all 1024 channels, the use of four CoBos enhances the system's performance.

The MuTanT (Multiplicity Trigger and Time) module within the GET system provides

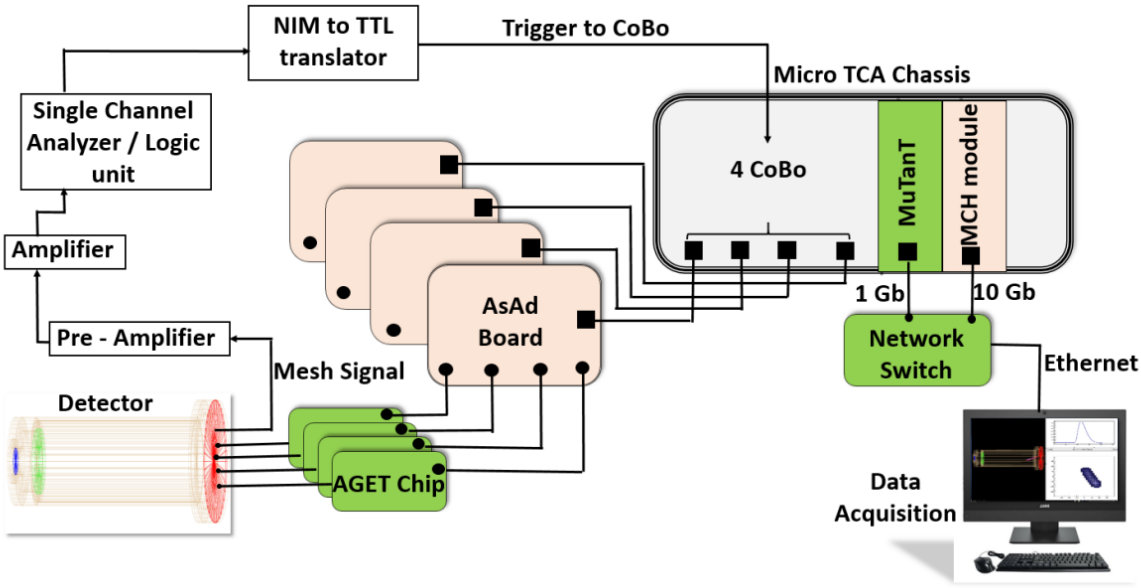

Figure 4.4: Simplified schematic of the GET system with a single µTCA (Micro Telecommunications Computing Architecture) chassis, 4 CoBos (Concentration Board) and a MuTanT (Multiplicity Trigger and Time).

the internal clock. This module is also essential for triggering capabilities and offers flexible triggering options for different experimental scenarios. Namely, the tigger is generated by total multiplicity and/or an external trigger. For additional details on the GET system see Ref. [55]. Figure 4.4 presents a schematic representation of the GET system, illustrating all its primary components and the specially designed mesh trigger (refer to Section 4.1.4) for the data acquisition system.

4.1.3 AsAd Box and T-Zap Boards

The integration of front-end electronics with the TPC is achieved through the innovative design of the AsAd Box and T-Zap boards. The AsAd Box was designed to house the front-end electronics of the GET system. It consists of four triangular Printed Circuit Boards (PCBs), known as T-Zap boards. These boards were custom designed and fabricated at

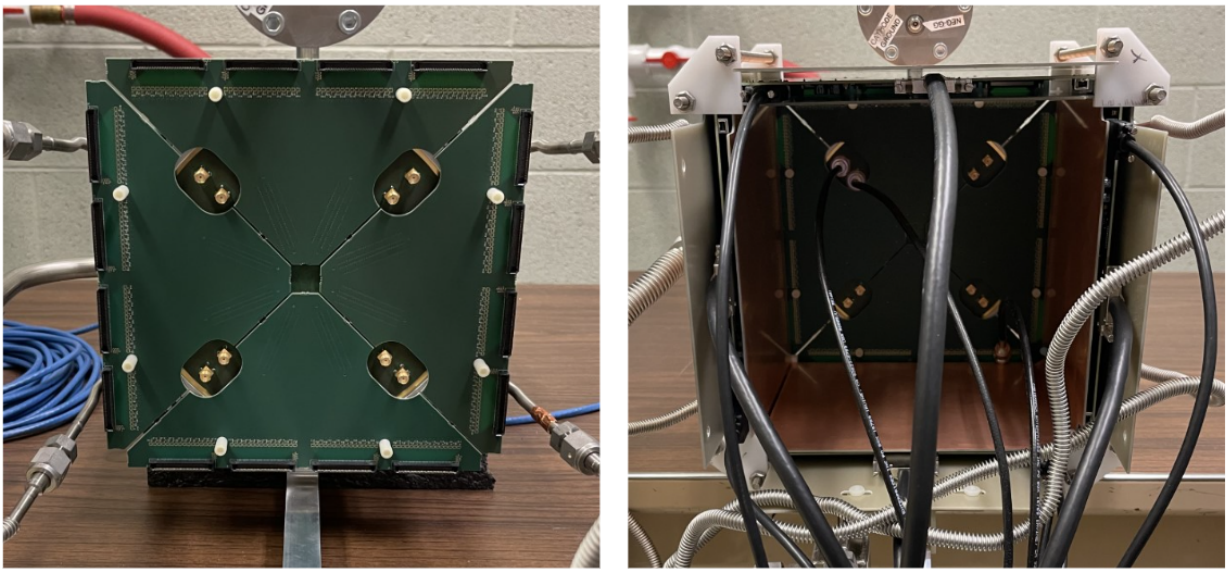

Figure 4.5: Left: Image of the 4 triangluar T-Zaps attached to the MM. Right: Image of the completed AsAd box.

CERN, and connect directly to the MM (see Figure 4.5). This connection is crucial as it enables the transmission of signals from the TPC to the AsAds (ASIC and ADC) boards. Each T-Zap board is designed to interface with the AsAd boards, with the layout allowing each AsAd board to handle a total of 256 signals originating from the MM pads. This design ensures that the signal transmission from the TPC to the AsAds is both efficient and reliable.

To optimize this configuration, the AsAd boards are positioned perpendicularly to the T-Zap boards. This arrangement places the AsAd boards as close as possible to the MM to minimize signal loss and ensure the integrity of the data being transmitted. An additional design consideration is the electromagnetic shielding of these components. The entire assembly, including the T-Zap and AsAd boards, is housed within a box constructed from copper plates. These plates serve as a Faraday cage to reduce the pickup of external electromagnetic noise. This shielding is vital in maintaining the quality of the signal and preventing interference that could compromise the quality of the data collected by the TPC. The assembled

AsAd Box configuration, including the T-Zaps, is depicted Figure 4.5.

4.1.4 Mesh Trigger

To trigger the DAQ a mesh trigger was designed to signal the arrival of charge at the MM mesh (see Figure 4.4). The operational principle of the mesh trigger revolves around the movement of ionization electrons towards the MM mesh. As these electrons traverse the mesh and enter the gap between the mesh and the resistive anode, they instigate an avalanche of charges. This avalanche results in electrons moving towards the resistive anode and ions towards the mesh, generating detectable signals on both the resistive anode and the mesh. Notably, these signals exhibit identical pulse heights but opposite polarities: negative on the resistive anode and positive on the mesh.

By grounding the mesh through a low impedance charge amplifier (a modified Canberra model 2006), a trigger logic signal is generated. This is achieved using a fast amplifier and leading-edge discriminator, ensuring that all particle tracks above a set threshold entering the active volume generate a mesh trigger. The signal-to-noise ratio (S/N) for the mesh signals, specifically using an α-particle source (see Section 7.0.10 for more details), was measured to be 16. Additionally, Section 5.3.6.1 describes an anti-coincidence circuit that was introduced to reduce the mesh trigger rate using the veto pad signals.

4.2 Performance Evaluation of GADGET II TPC

4.2.1 α-Particle Source Test

The initial performance assessment of the GADGET II TPC involved an α-particle source test, utilizing a ^{228}Th source (1µCi) which was installed in the TPC's gas handling system. The detector volume was filled with a P10 (90% Argon, 10% Methane) gas mixture at 800 Torr. The ^{228}Th undergoes decay to ^{220}Rn gas (half-life of 55.4 seconds), which, due to recoil from alpha emission, occasionally escapes the source's thin window, mixes with the P10 gas in the inlet line, and then flows into the detector. The decay of ^{220}Rn to ^{216}Po emits α-particles with an energy of 6.288 MeV and a branching ratio of 99.886% [56]. The subsequent decay of ^{216}Po emits a 6.778 MeV α-particle with a 99.9981% branching ratio [57].

For effective track analysis, signals on pads outside the main track's locality in a given event were removed to eliminate noise. This was achieved by implementing two different outlier detection algorithms, Hotelling and Squared Prediction Error (SPE), in sequence [58]. The Hotelling algorithm computes distances between data points and their mean based on variance, identifying potential outliers as points significantly distant from the mean. The SPE algorithm, on the other hand, calculates squared prediction errors for each data point using a statistical model, flagging points with high SPE values as outliers. Charge collection on a pad (point) is considered an outlier only if both algorithms concur on this assessment.

Figures 4.6 and 4.7 illustrate the projected 2D images of the ^{220}Rn alpha tracks on the pad plane, both before and after the elimination of outliers, respectively. Figure 4.8 presents a 3D reconstruction of an alpha track within the TPC. Principal Component Analysis (PCA) was employed to fit tracks by identifying lines and planes that best approximate the data via

least squares optimization [59]. In this analysis, the first and second principal components correspond to the length and width of a track, respectively. The length of a track is extracted and then the charge is integrated over all pads and converted to energy. The resulting energy spectrum for ^{220}Rn and ^{216}Po alphas is depicted in Figure 4.9. The 6.778 MeV α-peak appears weaker in comparison to the 6.288 MeV α-peak, likely because the positively charged ^{216}Po drifts towards the cathode. As a result, α-particles emitted into the inactive cathode from ^{216}Po decay are not detected.

After calibrating the MM pads using signals induced from pulses on the mesh, an energy resolution of 5.4% was achieved for events with an angular range of 0° to 70° relative to the pad plane. This level of resolution aligns with that of other TPC energy resolutions cited in the literature [60, 61, 62, 63]. However, it is important to note that the energy resolution of TPCs can vary depending on various factors such as gain matching procedures and operating parameters (e.g., type of gas, pressure, drift voltage) [61, 62]. Also, reference [61] mentions a smaller angular range relative to the pad plane, which can improve energy resolution at the expense of reduced statistics.

A range versus energy plot was generated for an ensemble of events, as shown in Figure 4.10. This plot is essential for particle identification, revealing two predominant features. The dense region where the 6.288 MeV and 6.778 MeV α-particles are found is marked as Region 1. Most events in Region 1 indicate α-particles depositing their full energy in the active volume, with expected ranges for the 6.288 MeV and 6.778 MeV α-particles. Events in Region 2 represent "wall effect," occurring when decays happen near the TPC's anode or cathode, resulting in α-particle tracks terminating on a solid surface after partial energy deposition in the active gaseous region. Events with tracks crossing the volume projected by the veto pads have been eliminated using an anti-coincidence condition, as discussed in

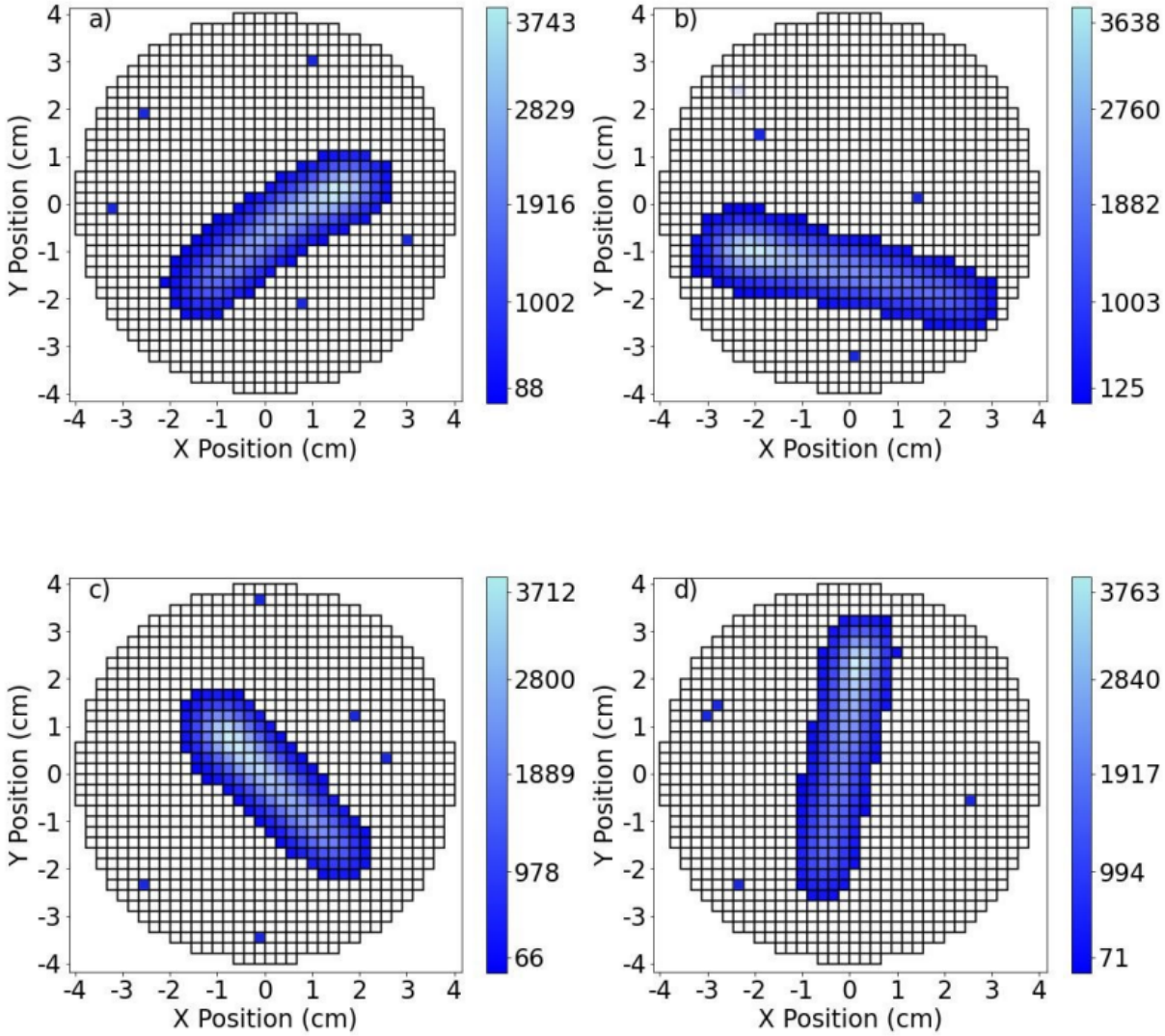

Figure 4.6: Label a)-d): 2D track projections on the MM pad plane in GADGET II TPC, showcasing tracks from ^{220}Rn alpha particles. The pads that are diffusely illuminated represent the points identified as outliers.

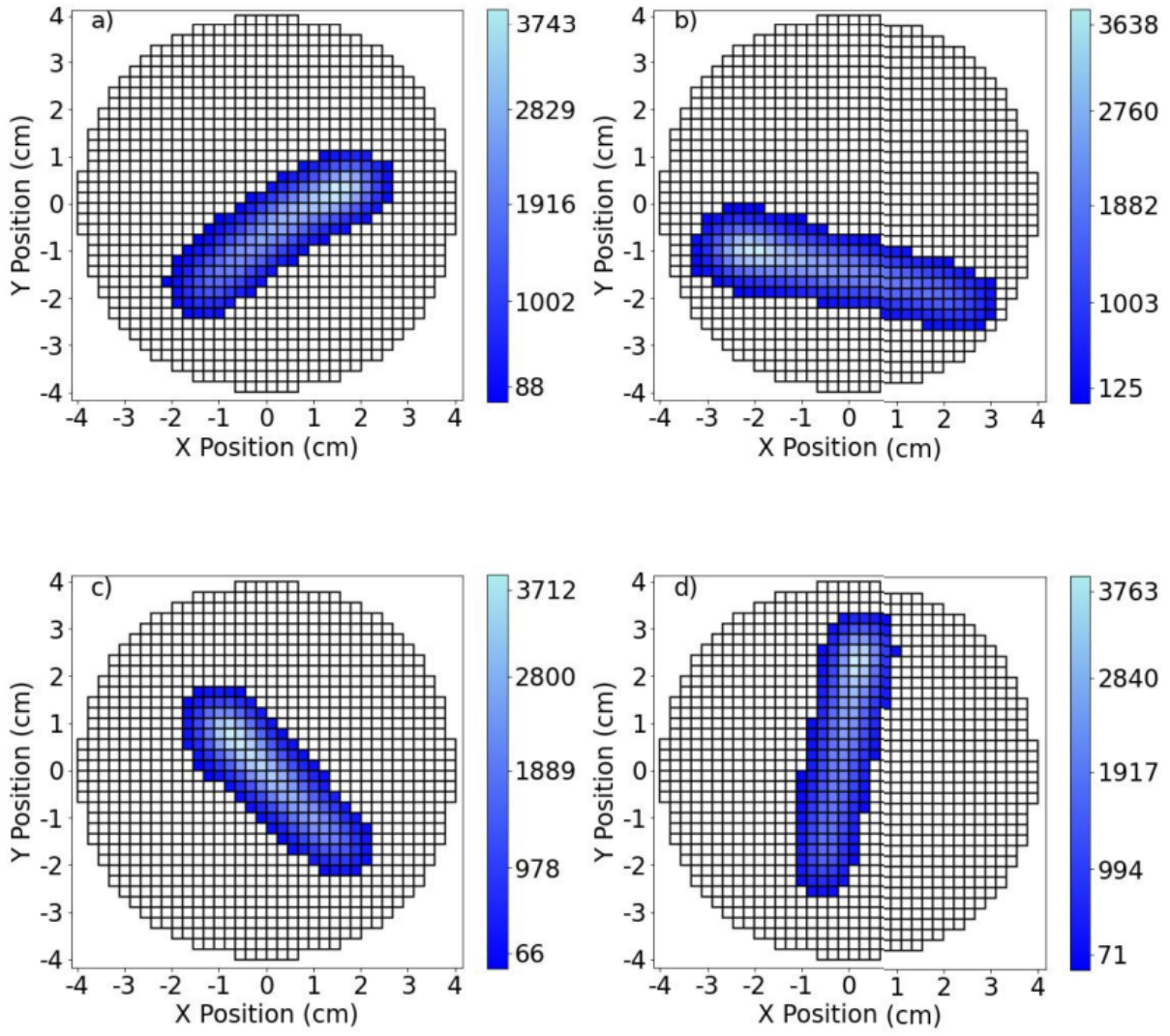

Figure 4.7: Label a)-d): 2D track projections on the MM pad plane in GADGET II TPC, showcasing tracks from ^{220}Rn alpha particles after outlier removal.

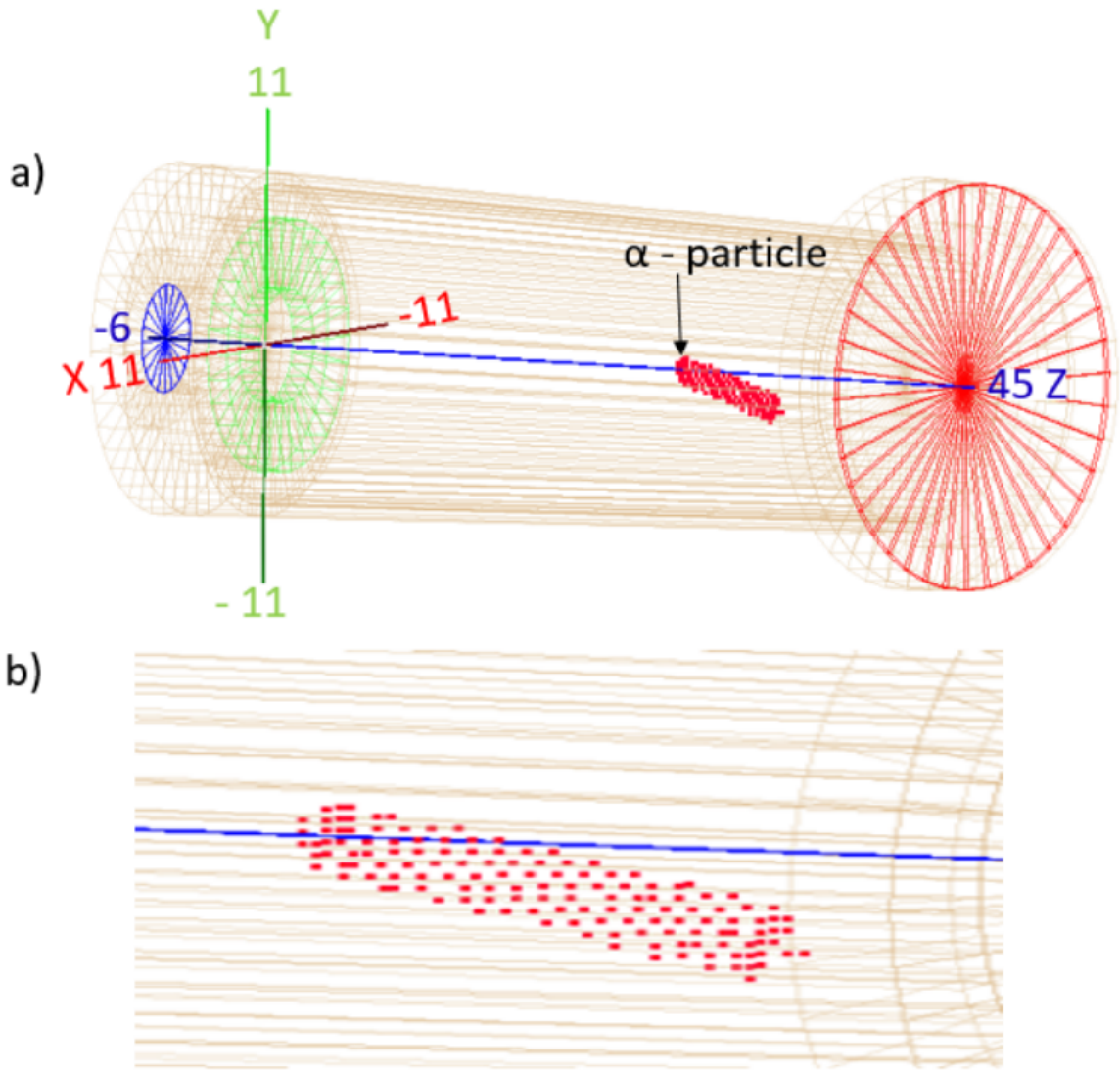

Figure 4.8: a) Illustrates a 3D hit pattern of a ^{220}Rn alpha track within the GADGET II TPC. b) Provides a zoomed-in image of the ^{220}Rn alpha track in the same TPC. For this representation, the z-coordinate is assigned an arbitrary value since the precise z position of the decay event within the TPC is not known. The numbers (11, -11, 45, and -6) displayed on the axis labels correspond to the lengths of the X, Y, and Z axes, respectively, measured in centimeters.

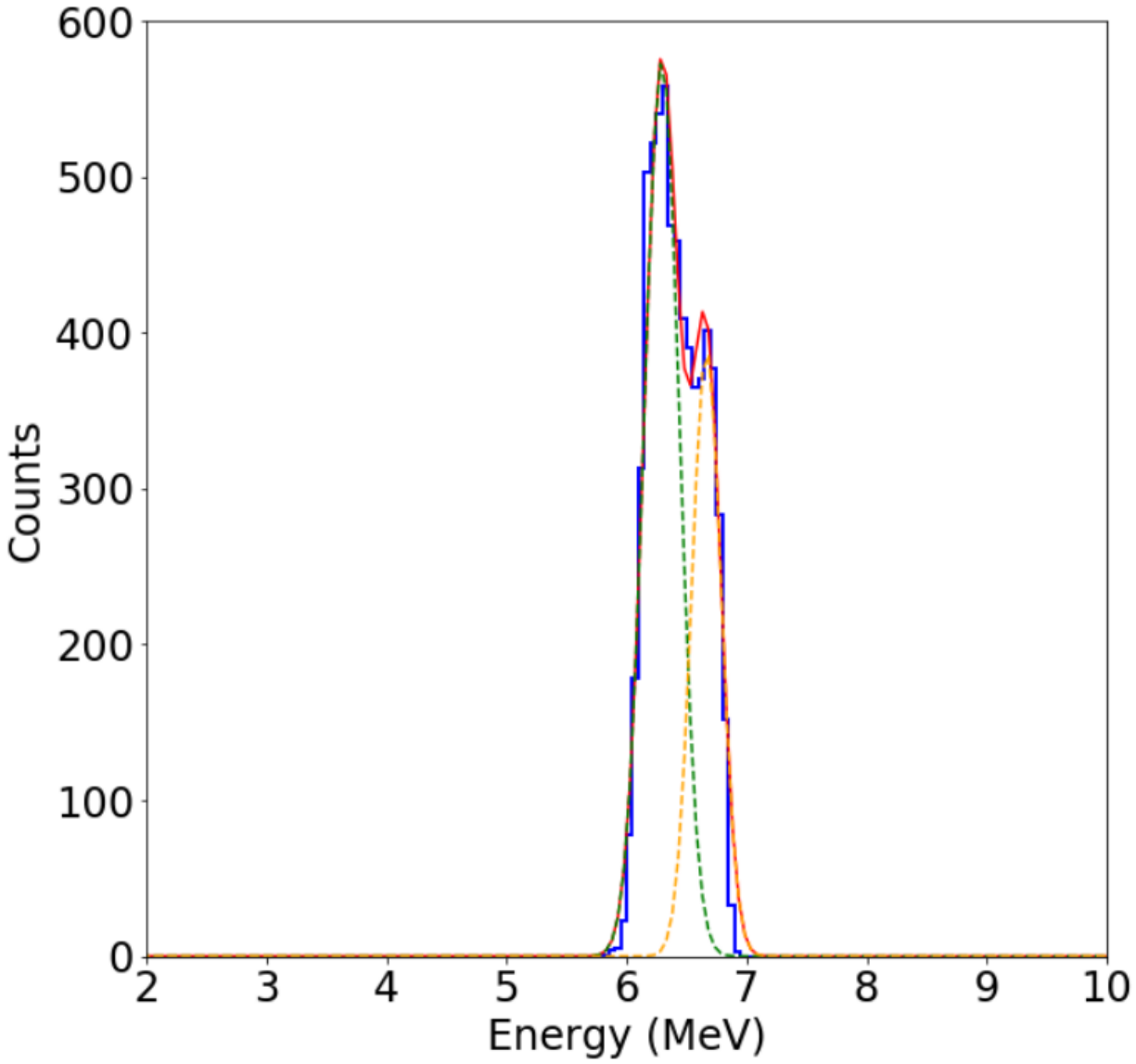

Figure 4.9: Energy spectrum for ^{220}Rn (shown in blue), featuring a fitted curve (in red) that indicates an energy resolution of 5.4% at 6.288 MeV. The peak at the higher energy level corresponds to the 6.778 MeV α-particle from ^{216}Po.

Section 5.3.6.1.

4.2.2 Cosmic-ray Muon Events

The GADGET II TPC's proficiency in detection extends to cosmic-ray muon measurements. This testing avenue focused on detecting minimum-ionizing cosmic-ray muons streaming through the active volume of the TPC. In these instances, only ≈27 electron-ion pairs are formed per pad in the drift zone, as is inferred from the cosmic-ray muon stopping power in P10 gas [64]. Thus, detecting these minimum-ionizing cosmic-ray muons demonstrates the superb sensitivity of the detector and the very good signal-to-noise ratio on the pads.

To accurately detect these muons, a setup using two plastic scintillators (BC408), each connected to a photomultiplier tube (PMT), was employed. These scintillators, measuring 2.5 cm in width, 40 cm in length, and 2 mm in thickness, were strategically positioned above and below the TPC's drift chamber. The PMT signals were used to generate a coincidence signal whenever a cosmic muon passed through both scintillators simultaneously. This coincidence signal served as a trigger for the data acquisition system, substituting the mesh trigger detailed in Section 4.1.4. For these specific measurements, the amplification field was increased to 44 kV/cm to ensure adequate gain. A few example tracks captured using this method can be seen in Figure 4.11.

These cosmic-ray muon measurements provide valuable insights into the diffusion effects of ionization electrons within the gas volume. For beam-line experiments there is no global external trigger, so the absolute z-position (distance from the MM) is not known. However, by measuring the width of cosmic muon tracks as a function of distance from the MM, we can calibrate the absolute position of charged particle events (alphas and protons) relative to their track width. To this end, the entire drift length of the detector was scanned in 5 cm

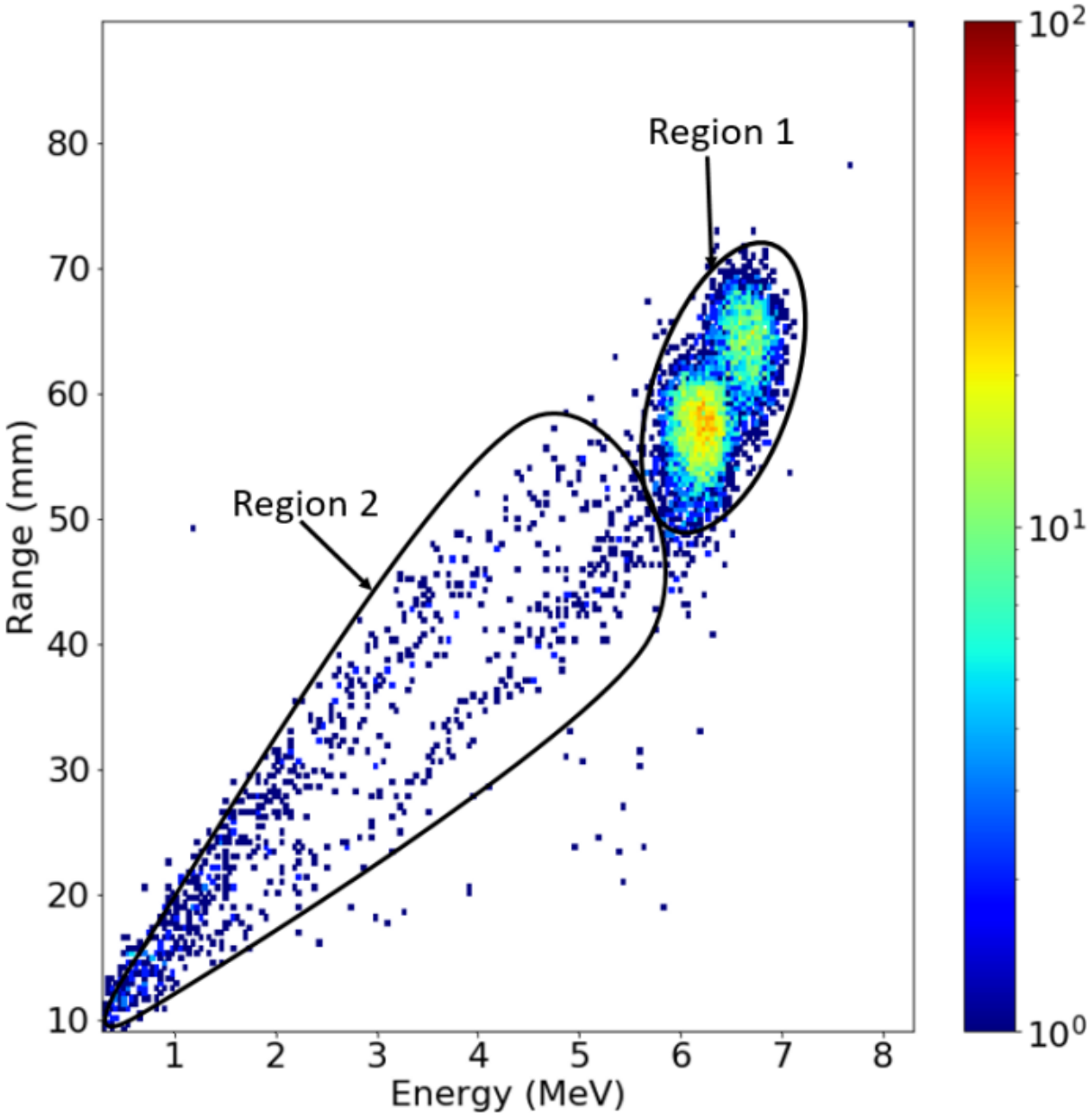

Figure 4.10: Aggregate histogram depicting range versus energy for ^{220}Rn and ^{216}Po α-particles, encompassing events with angular orientations ranging from 0° to 70° relative to the pad plane.

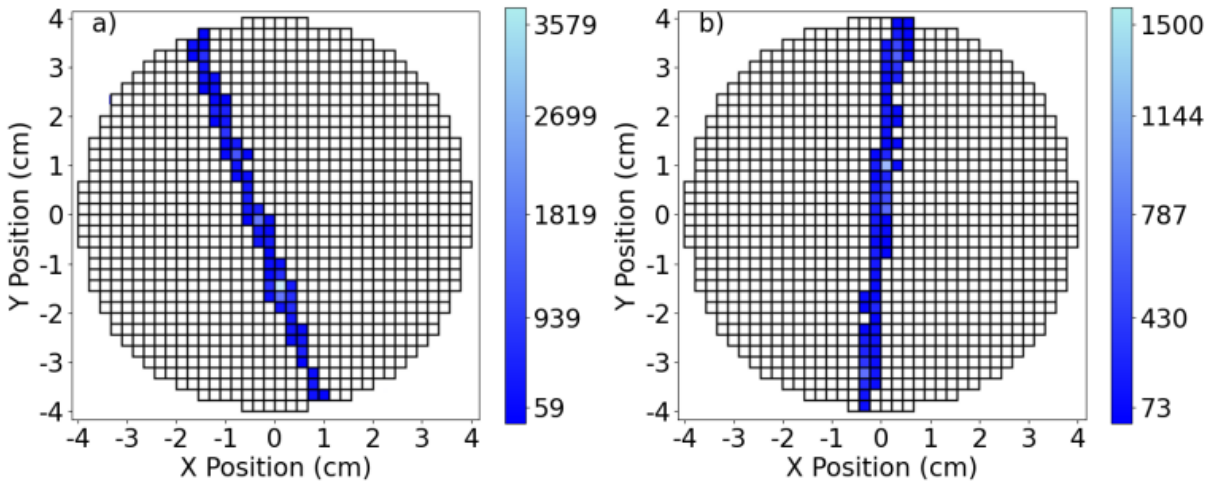

Figure 4.11: Label a)-b): Examples of cosmic-ray muon tracks detected in the GADGET II TPC.

increments to determine the cosmic-ray muon track widths as a function of distance. The width W of these tracks as a function of drift length is mathematically described by the function $W = A + BC^x$ [65], where A represents the initial track width, B is the diffusion level, C is the rate of diffusion, and x is the drift distance in the gas. Consequently, tracks closer to the upstream end (cathode) appear broader than those nearer to the downstream end (anode), as illustrated in Figure 4.12.

Additionally, the drift velocity of these events was ascertained from the timing distribution of the cosmic-ray muon events. The value was determined by fitting the drift time versus distance from the MM data with a linear model as seen in Figure 4.13. The drift velocity was found to be 5.44 ± 0.03 cm/µsec. In a 40-cm drift region, the maximum drift time for primary ionization electrons is thus calculated to be 7.352 ± 0.041 µsec. These findings align with previous measurements conducted with the original GADGET detection system using a particle-gamma coincidence method [66].

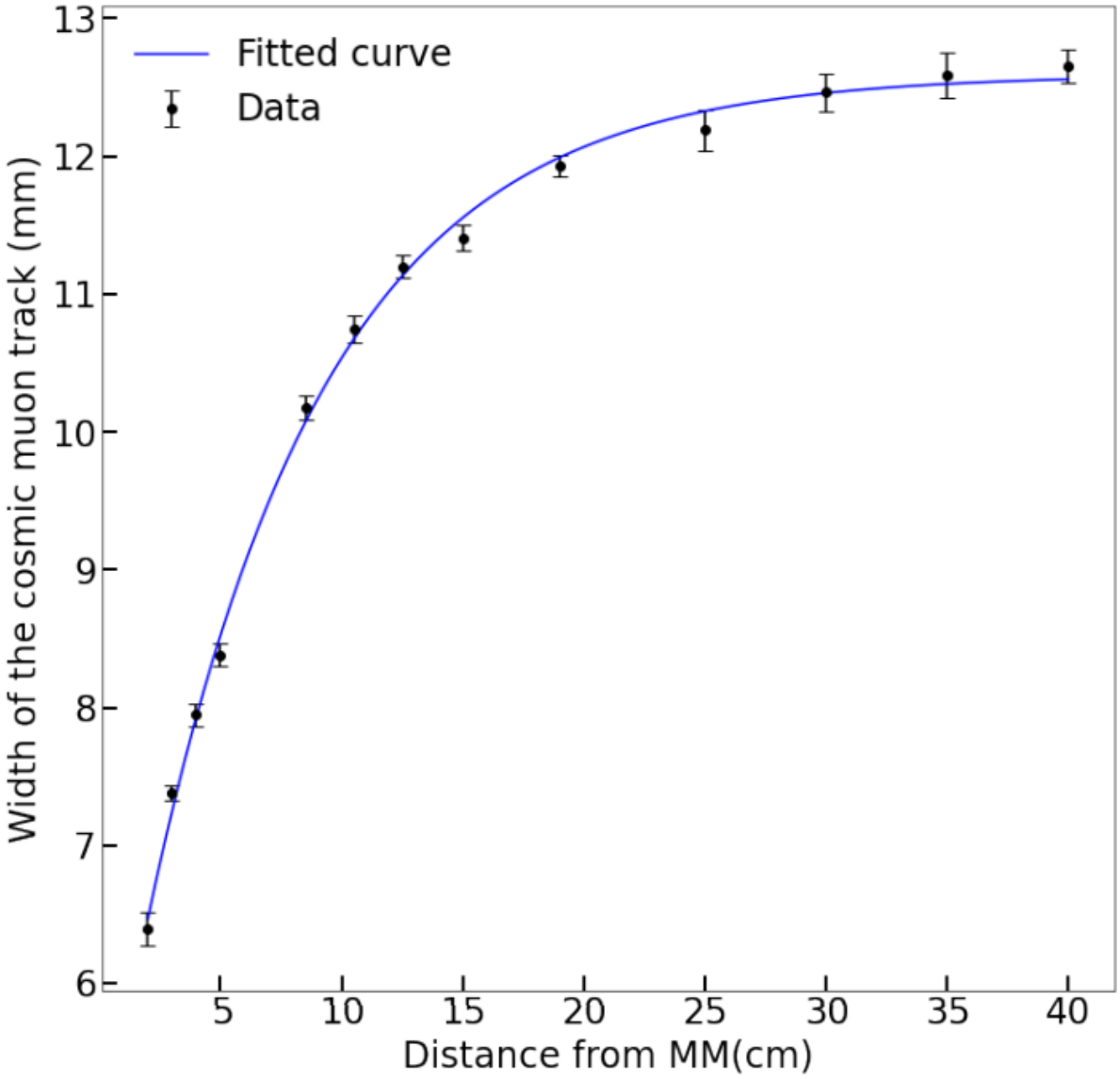

Figure 4.12: Average width of cosmic-ray muon tracks as a function of distance from the MM pad plane.

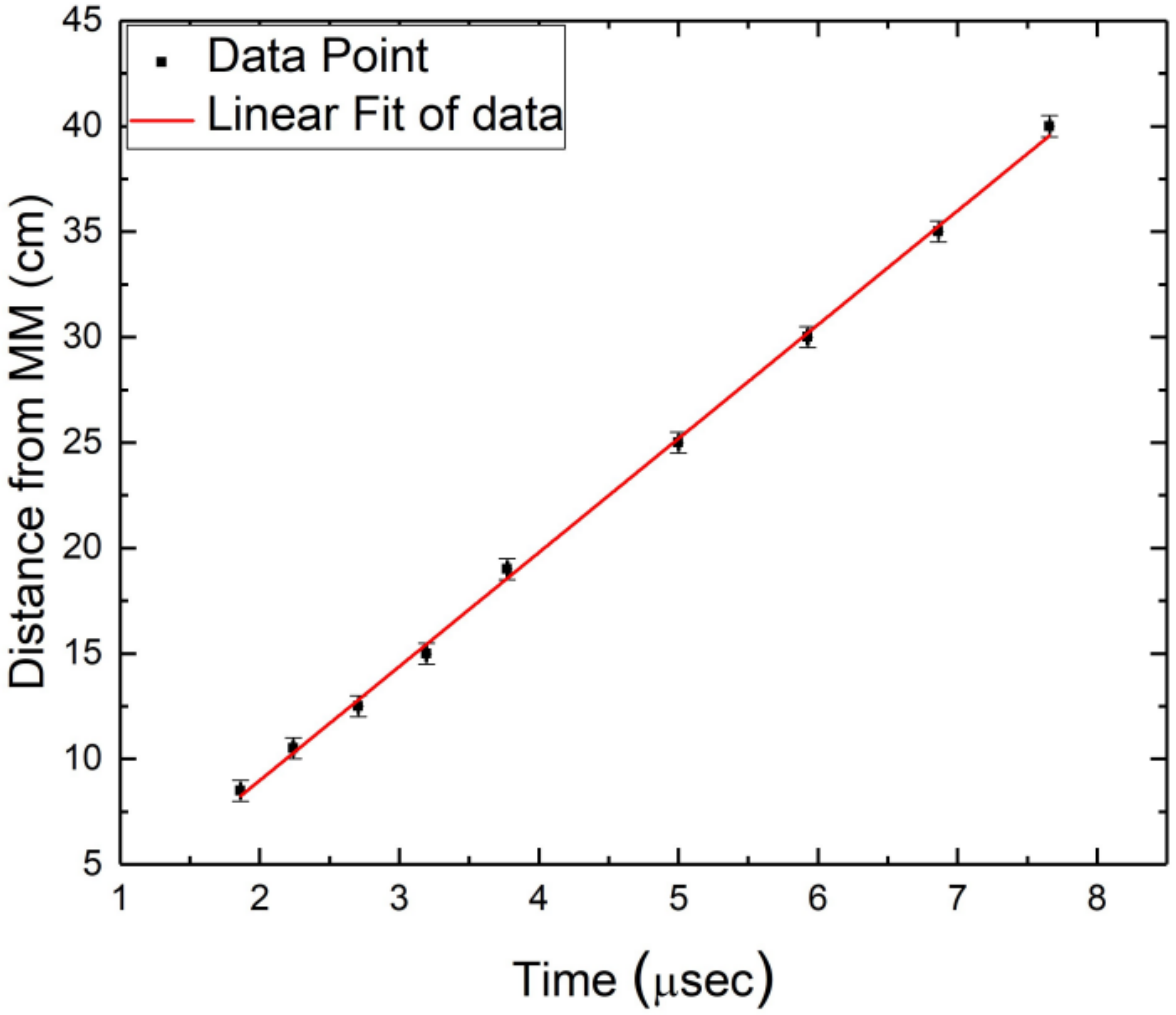

Figure 4.13: Average width of cosmic-ray muon tracks as a function of distance from the MM pad plane.

Table 4.1: Nominal operating parameters of GADGET II TPC.

TPC Parameters	
No. of measurement pads	1016
Pad size	2.2×2.2 mm^2
Pad plane area	50.24 cm^2
No. of veto pads	8
Veto pad area	28.26 cm^2
Length of drift region	400 mm
Amplification gap	128 µm
Gating Grid Parameters	
No. of gold plated copper wires	60
Diameter	20 µm
Wire separation	2 mm
GET Parameters	
Electronic sampling frequency	50 MHz
Signal shaping time	502 nsec
Event rate	1 kHz
GET gain	1 pC
Gas Amplifier Parameters	
Typical gas composition	P10 (90% Ar + 10% CH_4)
Gas pressure	800 Torr
Gas gain	40 for ^{220}Rn α-particles
Drift field	150 V/cm
Amplification field	30 kV/cm
Drift velocity	5.44 ± 0.03 cm/µsec
Temperature	25°C
Micromesh Parameters	
Resistance	10 MΩ/square
Capacitance (calculated)	287 nF
Mesh - Anode separation	128 µm

Chapter 5

Experiment E21072 at the Facility for Rare Isotope Beams

Experiment E21072 was conducted at the Facility for Rare Isotope Beam (FRIB) at Michigan State University in November 2022. The experimental campaign lasted just over one week starting on November 19^{th} and concluding on November 28^{th}. During the experiment, a beam of ^{20}Mg was delivered to the GADGET II TPC. This Chapter will cover the purpose of the experiment, how the beam was produced, and detail the experimental setup and procedure.

5.1 Purpose

Sensitivity studies indicate that the $^{15}\text{O}(\alpha,\gamma)^{19}\text{Ne}$ reaction is among the most important reaction rate uncertainties affecting the modeling of Type I X-ray burst light curves (see Chap. 3). This reaction is anticipated to be dominated by the 4.03 MeV excited state in ^{19}Ne. Given the established lifetime of this state, determining the reaction rate requires only a finite value for the minor alpha-particle branching ratio, Γ_α/Γ. Past measurements have documented that this particular state is populated in the decay sequence of ^{20}Mg, with $^{20}\text{Mg}(\beta p\alpha)^{15}\text{O}$ transitions occurring through the critical $^{15}\text{O}(\alpha,\gamma)^{19}\text{Ne}$ resonance. This process is marked by the distinct emission of a proton and an alpha particle. In order to

detect these near simultaneous emissions, the GADGET II detection system (see Section 5.3) was employed at the Facility for Rare Isotope Beams.

5.2 Beam Production

The production of the rare isotope beam at FRIB began with a stable isotope that was ionized using an electron cyclotron resonance ion source. The resulting ions were then injected into the FRIB superconducting RF heavy-ion linear accelerator (linac). This accelerator uses superconducting radio frequency (SRF) cavities to accelerate ions to high kinetic energies. A 3D rendering and schematic of the superconducting RF linac can be see in Figure 5.1. The primary beam for experiment E21072 was ^{36}Ar, which was accelerated using the linac to an energy of $\sim$ 200 MeV/u.

The ^{36}Ar primary beam was then focused to a 1mm spot and impinged on a multi-slice carbon target rotating at 5000 rpm. When the beam struck this target it generated a nuclear fragmentation process, which produced a cascade of different isotopes including ^{20}Mg, the isotope required for the experiment.

Following fragmentation, the resulting cocktail beam passed through the Advanced Rare Isotope Separator (ARIS). ARIS is a sophisticated three-stage fragment separator, aimed at the efficient refinement of rare isotope beams (see Figure 5.2) [14]. The first stage is the vertically-oriented preseparator, complete with a beam dump. In the preseparator the secondary beam undergoes coarse initial selection of the desired isotopes. This is accomplished using the preseparator's magnetic dipoles that work much like prisms, bending and spreading the beam such that only the desired isotopes make the turn to the next section. This process allows for the categorization and isolation of fragments, and is described by the

Lorentz force, expressed as $mv/q = B\rho$. Here, m represents the ion's mass, v denotes its velocity, q is the nucleus's charge, and $B\rho$ symbolizes the magnetic rigidity. This configuration is meticulously calibrated to ensure that ^{20}Mg ions maintain their trajectory at the beam-line's core. Consequently, ions exhibiting particular magnetic rigidities follow distinct trajectories with differing radii, thereby facilitating their separation from the primary beam.

Nonetheless, ions with different masses can exhibit similar magnetic rigidities to that of the desired ^{20}Mg ions. To address this, a wedge energy degrader was employed between the preseparator dipoles. This wedge operates by decelerating ions in a manner proportional to the square of their mass (A^2), effectively altering the magnetic rigidity of these non-target ions. The preseparator then delivered the beam to the ground level separator (stage 2 and 3) which consists of additional dipole and quadrupole magnets for further isotope refinement and beam focusing, respectively. When the ^{20}Mg beam exited ARIS it was incident on a focal plane with collimating slits, and was then delivered to our experimental setup, which was located in the transfer hall at FRIB. Additionally, the beam was delivered in cycles. Each cycle was comprised of two phases: initially, the beam was delivered for a period of 110 milliseconds, immediately after which the beam was stopped. Subsequently, a decay counting phase would occur, spanning an identical duration of 110 milliseconds. This pattern ensured a clear separation between delivery and measurement intervals. The main beam contaminants included ^{18}Ne, ^{17}F, and ^{16}O, however, none of these contaminants create a background of any concern as they are not beta-delayed particle emitters.

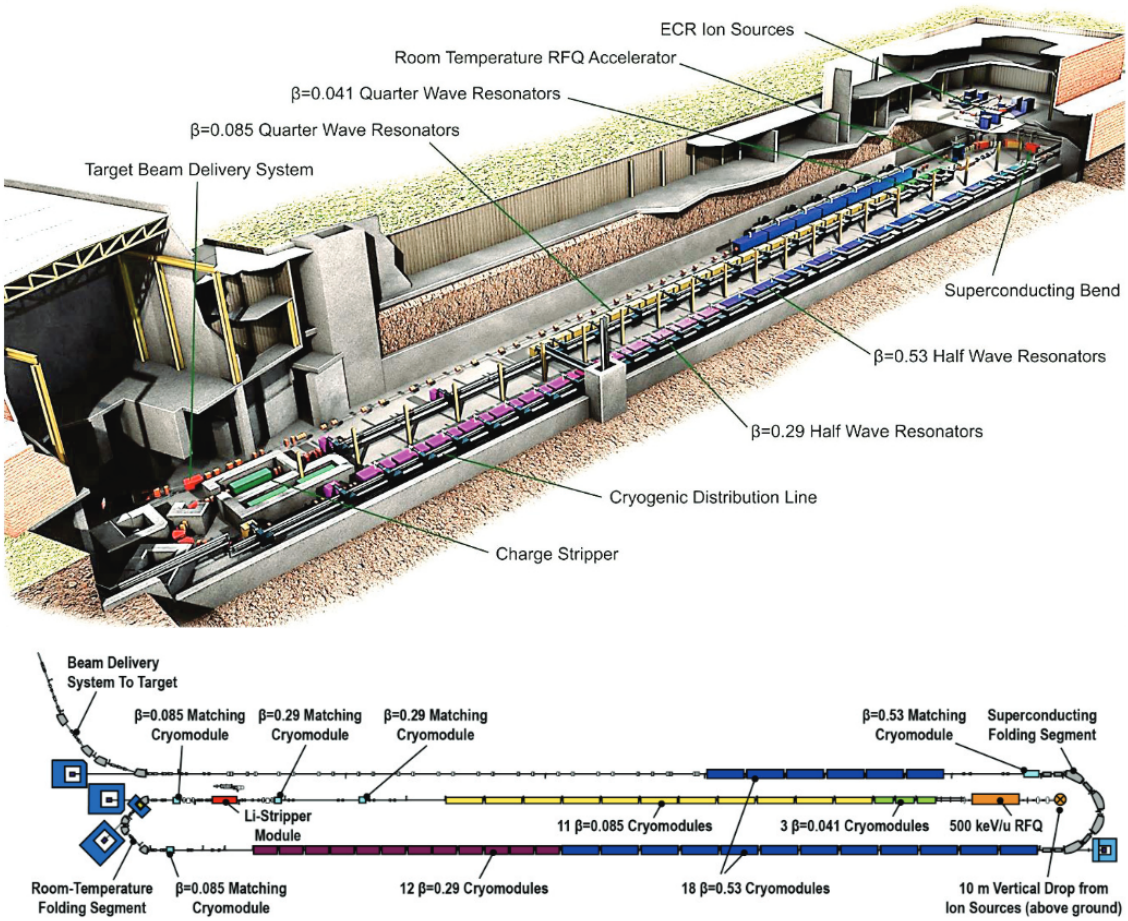

Figure 5.1: Top) Scale 3D rendering of the superconducting radio-frequency driver linear accelerator at FRIB. Bottom) Schematic layout of the FRIB driver linac [13].

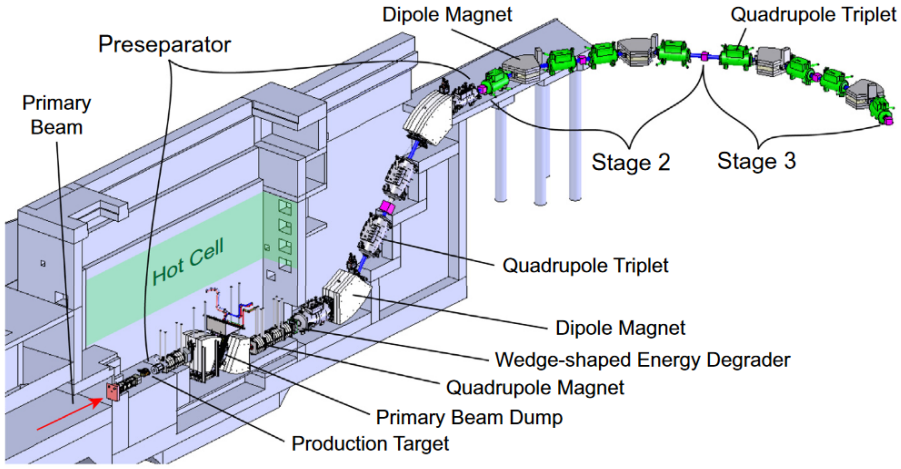

Figure 5.2: This ARIS diagram illustrates the driver linac's primary beam approaching the production target from the lower left. Isotope beams travel through the three stages of the fragment separator (preseparator, stage 2, and stage 3) before being channeled towards experimental setups [14].

5.3 Experimental Setup

The GADGET II detection system as configured for E21072 consists of a diverse assembly of detection technologies, encompassing four primary detector types: A compact TPC with a resistive MicroMegas, the Decay Germanium Array initiator (DEGAi), Lanthanum Bromide ($LaBr_3$) detectors, and a silicon PIN (positive-intrinsic-negative) detector.

Other ancillary components are integral to the successful operation of these detectors, such as an energy degrader, and various Data Acquisition Systems (DAQs), which play pivotal roles in the seamless operation and data handling of the detection array. Discussions on both the primary detectors and these essential supporting elements are presented in the ensuing sections and subsections.

5.3.1 TPC

The TPC was operated with P10 gas (90% Argon 10% Methane) at $\sim$ 800 Torr. This pressure was chosen as it yields optimal track lengths, and ensures that any small leaks would cause gas to flow out of the TPC thereby mitigating air contamination. The pressure was regulated and monitored continuously using the MKS πPC PC99 pressure controller with mass flow meter. To maintain a comprehensive record of the operational environment, the temperature of the TPC was also recorded throughout the experiment via a thermocouple attached to the outside of the drift chamber.

The resistive MicroMegas of the TPC was biased at +440V. Additionally, the gating grid was switched between -225V (transparent mode, used during decay counting phase) and +150V (opaque mode, used during beam implantation) to correspond to the beam pulsing. The gating grid timing also needed a 5ms buffer period after the beam had stopped and before beam turned back on to ensure implantation ionization was not captured. The timing for the gating was provided from the accelerator as an on/off signal (square wave) that was 5 ms wider on both sides to account for the desired buffer period. This signal was then used with a CGC Instruments NIM-AMX500-3 switch which alternated the transparent and opaque voltages.

Biasing for both the MicroMegas and the gating grid was done using a Mesytec MHV-4 module, a 4-channel high precision bias supply. Furthermore, to establish a drift field of 150 V/cm, the field cage was biased at -6 kV via a N1470B programmable high voltage power supply from CAEN. Additional details of the TPC, including default operating parameters used during the experiment, are covered in Section 4.

5.3.2 DEGAi

DEGAi is part of the FRIB Decay Station initiator (FDSi), which is generally maintained/serviced by Oak Ridge National Laboratory (ORNL) and the University of Tennessee at Knoxville. DEGAi consists of 11 high-purity germanium (HPGe) clover detectors that are used for the detection of prompt gamma-rays. This works because when gamma-rays interact with the crystal lattice of the Ge, it leads to the formation of electron-hole pairs. When a reverse bias is applied, this triggers a current pulse to propagate through the Ge. The magnitude of the current pulse is proportional to the number of electron-hole pairs generated, which in turn is proportional to the energy of the absorbed gamma ray. By measuring this pulse, the energy of the incident gamma ray can be accurately determined. Being able to detect gamma-rays in this fashion gives us a detailed way to identify beam contaminants, and acts as a beam diagnostic. It also allows us to clarify the decay scheme of ^{20}Mg. Using a single CLARION1, spherically symmetric hemisphere that covers a 2π solid angle we obtain an efficiency of 6.0(12)% at 1 MeV [67]. A schematic of DEGAi coupled with the TPC and AsAd box can be seen in Figure 5.3.

A significant amount of development work was needed to integrate the TPC with DEGAi. This included designing and building a new TPC support structure, a new gas manifold, and an additional support structure to house $LaBr_3$ detectors. An image of the experimental setup that shows these features can be seen in Figure 5.4.

5.3.3 $LaBr_3$ Detectors

Three 2" $LaBr_3$ detectors were tested as a beam ranging diagnostic tool. The central $LaBr_3$ detector was positioned so as to align with the central beam implantation location. Then

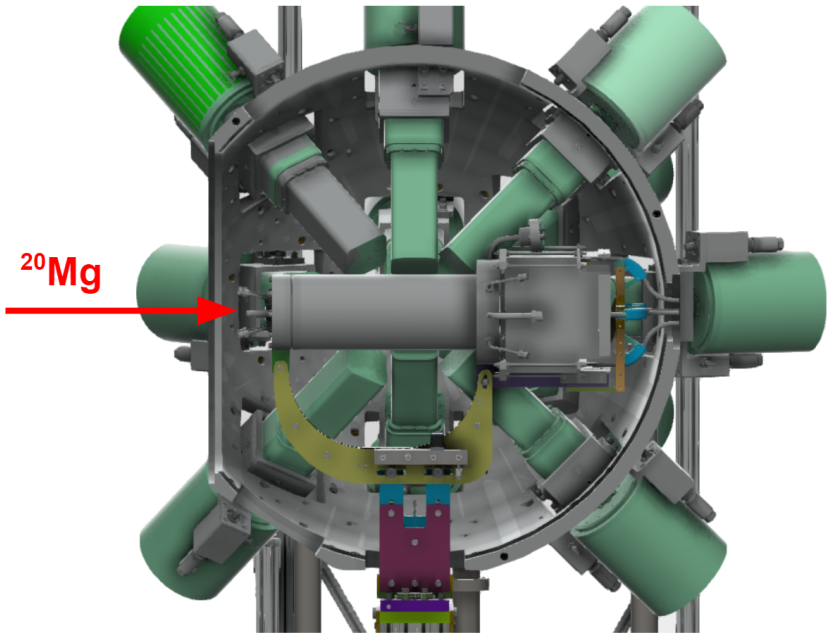

Figure 5.3: Schematic representation of the FRIB Decay Station's DEGAi, featuring the TPC and AsAd box at the core. A red arrow illustrates the entry path of a ^{20}Mg beam into the TPC, and DEGAi is used to measure gamma-rays emitted from the TPC following nuclear decay.

the relative gamma counts in each detector could provide a coarse method for ensuring that the beam was being deposited in the center of the detector. $LaBr_3$ detectors work by utilizing the scintillation process to detect gamma rays. When a gamma ray enters the $LaBr_3$ crystal, it interacts with the crystal lattice, producing high-energy electrons that excite the atoms in the crystal. These excited atoms then emit visible light as they return to their ground state. The emitted light is collected by a photomultiplier, which converts it into an electrical signal proportional to the energy of the incoming gamma ray. Despite an efficiency of approximately 0.27% at 1 MeV—considerably lower than the efficiency of DEGAi's HPGe detectors—$LaBr_3$ detectors offer superior response times and the convenience of operation at ambient temperatures.

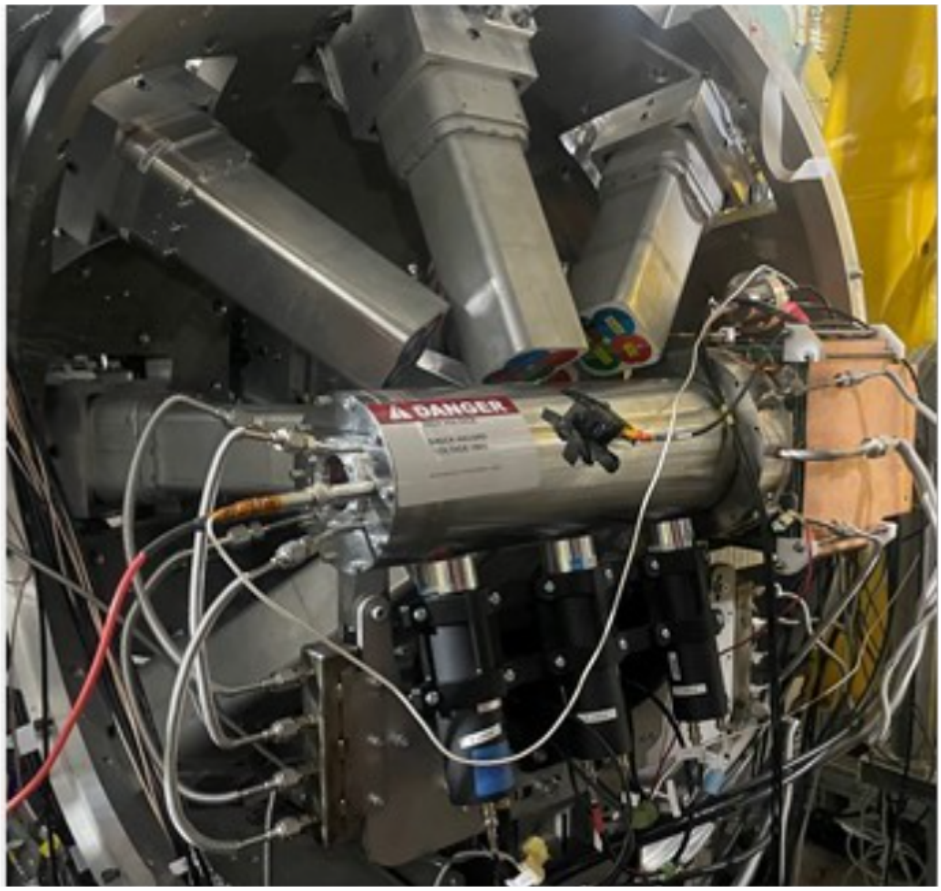

Figure 5.4: Image of the experimental GADGET II setup. The TPC and AsAd box are positioned at the center of the CLARION1 array by a newly built support structure that includes a new gas manifold and three $LaBr_3$ detectors. Surrounding the TPC on one side is DEGAi.

5.3.4 PIN Detector

A Silicon MX100 PIN detector was housed in a diagnostics box approximately 1m upstream from the Kapton window of the TPC, and was positioned in the beam path to measure energy loss (Δ E). A PIN semiconductor diode consists of three main layers: the intrinsic (i-type) layer (in this case Si), which is sandwiched between p-type, and n-type layers. When particles from the beam pass through the PIN detector, they lose energy in the intrinsic layer, which is measured. The PIN detector operates in tandem with a scintillator in ARIS to generate a timing signal that corresponds directly to the time of flight (ToF) between the two detectors. The scintillator is located at the DB3 position in ARIS. By integrating the energy output from the PIN detector with the ARIS timing signal, a particle identification (PID) plot can be constructed (see Figure 5.5). Note that the PIN detector cannot be used with full beam intensity without risking radiation damage, thus, a 100x attenuated, continuous beam was used during periodic PID runs. The PIN detector was moved in and out of the beam path via manual actuators.

5.3.5 Beam Energy Degrader

An aluminum degrader with a thickness of 3.227 mm was also housed in the diagnostics box with the PIN detector. This high purity aluminium plate is placed in the beam path to degrade the energy of the incoming ions. Simulations were done to ensure optimal energy loss and beam ranging with the degrader at 30°. Then the degrader can be rotated to increase or decreased the amount of energy loss. In this case 0°(perpendicular to the beam) reduces the effective thickness of the degrader, and thus reduces energy loss. Conversely, an angle of >30°increases the effective thickness and therefore increases energy loss. The degrader was

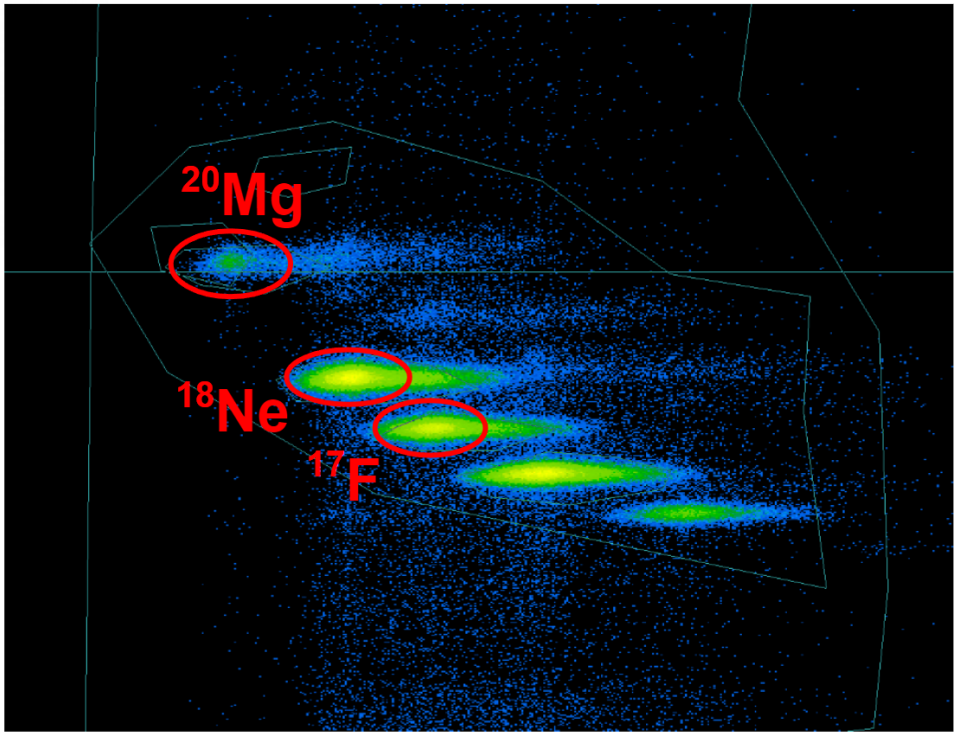

Figure 5.5: PID plot generated using the ΔE-TOF technique for precise particle differentiation. The plots shows that ^{20}Mg was in the beam, along with some other contaminants.

attached to a stepper motor that could be controlled remotely, so that the ideal degrader angle needed to ensure beam implantation in the center of the TPC could be found while beam was being delivered.

5.3.6 Data Acquisition

The GADGET II TPC utilizes the GET (Generic Electronics for TPCs) data acquisition system (see Section 4.1.2 for a full description of the GET system). The experimental setup for the GET system includes 4 AsAd boards (one board for each quadrant of the MM), 4 CoBos, 1 MuTanT module, 1 MCH module, a Micro-TCA chassis, a 1Gb/10Gb network switch, 4 Mac-mini computers (one for each CoBo), and 4 20Tb external hard-drives (data storage for each CoBo).

The germanium array of DEGAi uses the Digital Data Acquisition System (DDAS) [68]. This system utilizes the 250 MHz XIA Pixie-16 module, which can handle signals from an array of different detectors. Each module is equipped with 16 channels and is installed in a computing crate, allowing for the interconnection of several modules within the same framework.

Ideally, each channel from the detectors in DEGAi and from the MM pads in the TPC, would yield consistent outputs for a specific energy input. Yet, output values can vary slightly over time, a phenomenon referred to as gain drift. To mitigate the effects of gain drift, data from the GET electronics for the TPC and DDAS for DEGAi were taken in 1 hour long runs, where the start and stop of each run for both systems was synchronized. This strategy ensures that any variations in output due to gain drift are consistently adjusted for during energy calibration. Additionally, by frequently starting new data runs, the potential loss of data resulting from DAQ malfunctions is significantly reduced.

To ensure precise synchronization for gamma-particle coincident measurements, a clock signal was sent between DDAS and GET at 50 MHz. Both systems would reset clocks at the start of each run. Additionally, the mesh trigger signal (see Section 4.1.4) was split and sent to both DAQs and recorded for the duration of each run. This unique signal can then be matched in both system ensuring proper synchronization.

5.3.6.1 Data Throughput Optimization in TPC

The data acquisition capabilities of the GET system (Section 4.1.2), crucial for the GADGET II TPC's operational efficacy, are notably constrained by data throughput limitations. These limitations directly influence the TPC's rate capability. In the context of our experiment, we needed to be able to record events at the scale of thousands of decays per second in order to

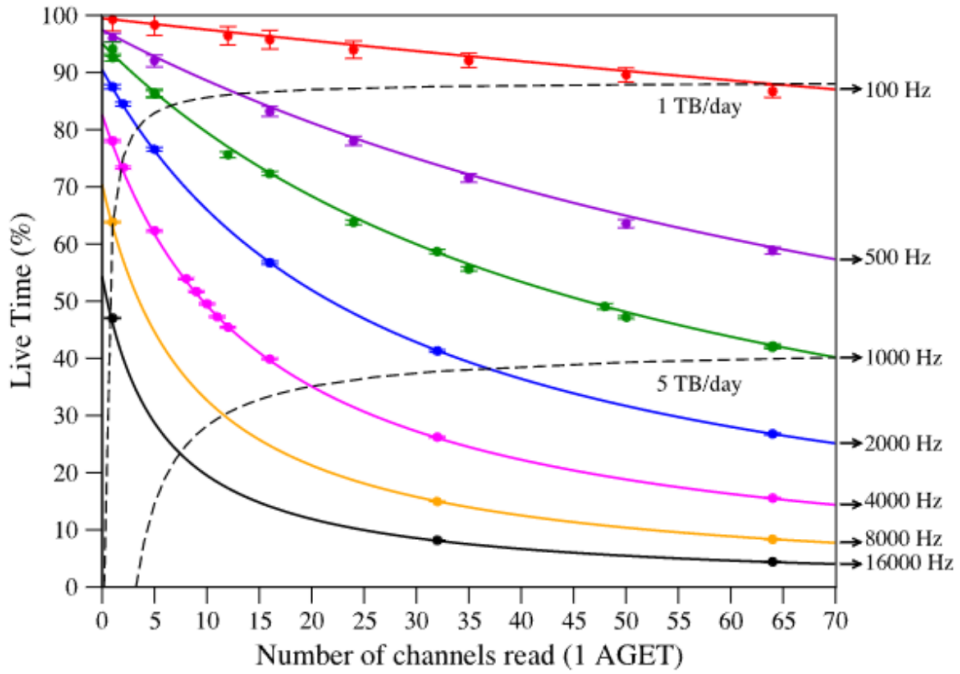

Figure 5.6: Live time of the GET system as a function of channels read for one AGET chip. The plot illustrates the system's performance degradation with increasing event rates and channel activity.

have enough statistics to measure the rare $^{20}\mathrm{Mg}(\beta p\alpha)^{15}\mathrm{O}$ events. However, this target event rate far exceeded the handling capacity of the existing GET system, posing a substantial challenge to the feasibility of our experiment.

The live time of the GET system, as depicted in Figure 5.6, illustrates the system's performance as a function of channels read for a single AGET chip. These AGET chips, being fundamental to the GET system's operation, represent a critical bottleneck. As evidenced in the plot, at an event rate of 2 kHz, even with a single pad firing, the system fails to process approximately 10% of triggers. This inefficiency escalates dramatically with increased channel activity, rendering the system incapable of supporting the desired event rates for our experiment. To address this significant bottleneck, a multifaceted approach was adopted.

This first step in tackling this problem involved expanding the array of Concentration Boards (CoBos) and optimizing parameter settings. The CoBos are responsible for data

aggregation and transfer to the computing system. Our initial setup only called for a single CoBo to be used, but this lead to substantial dead time for event rates surpassing 1 kHz. A series of tests investigating this issue, involving a random pulse generator and the analysis of α-decay events from ^{220}Rn, led to a crucial finding: the data throughput of the system increases approximately linearly with additional CoBos [55]. A particularly effective configuration that emerged from these trials involved the use of a four-CoBo setup (one CoBo per AsAd board) [15].

In addition to increasing the number of CoBos, fine-tuning parameter settings, such as channel hit readouts and threshold adjustments, was identified as a pivotal factor in enhancing data throughput. A significant breakthrough was achieved by reducing the number of time bins per trace. Specifically, decreasing the default readout depth from 512 to just 64 time bins resulted in a notable increase in throughput. This optimization and its consequential impact on data handling capabilities are depicted in Figure 5.7, which illustrates the data throughput as a function of event rate under various time binnings and CoBo configurations.

The next method we used to improve the system throughput was the introduction of a front-end veto condition, which emerged as the most impactful solution. If any energy is detected on the veto pads of the pad plane (see Figure 5.8), the event trigger is discarded, ensuring that only events with energy concentrated on the main part of the pad plane are acquired. This is achieved by soldering lemo connections to the capacitor pads on the zap boards that are linked to each veto pad. With this we established a direct signal connection from the veto pads, which were connected to a mesytec MSCF-16-F; a shaping/timing filter amplifier with constant fraction discriminator and multiplicity trigger. The resulting output from this amplifier is then placed in anticoincidence with our mesh trigger (see Section 4.1.4 for details on the mesh trigger) through an OR gate, allowing for the preemptive

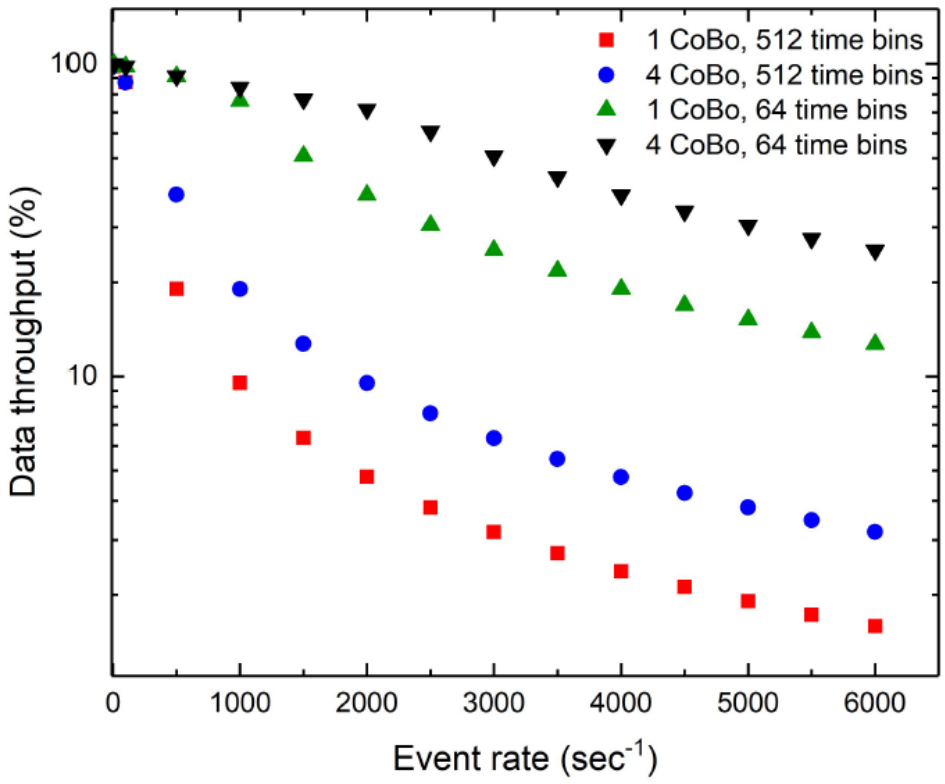

Figure 5.7: Data throughput as a function of event rate for various time binnings and CoBo configurations [15].

exclusion of veto events from processing. This front-end veto condition reduced our trigger rate by an order of magnitude, effectively mitigating the event rate issue and aligning the system's capabilities with the requirements of our high-event-rate experiment. Images of the construction/setup of the front-end veto condition can be seen in Figure 5.9.

5.4 Procedure

During the experiment, data was collected in hour long runs to guarantee uniform readings across our array of detectors. Moreover, supplementary runs were taken prior to and subsequent to the experimental phase to facilitate calibration of the TPC. These calibration runs were done using ^{220}Rn and ^{216}Po alpha-particles from a ^{228}Th source installed in the gas

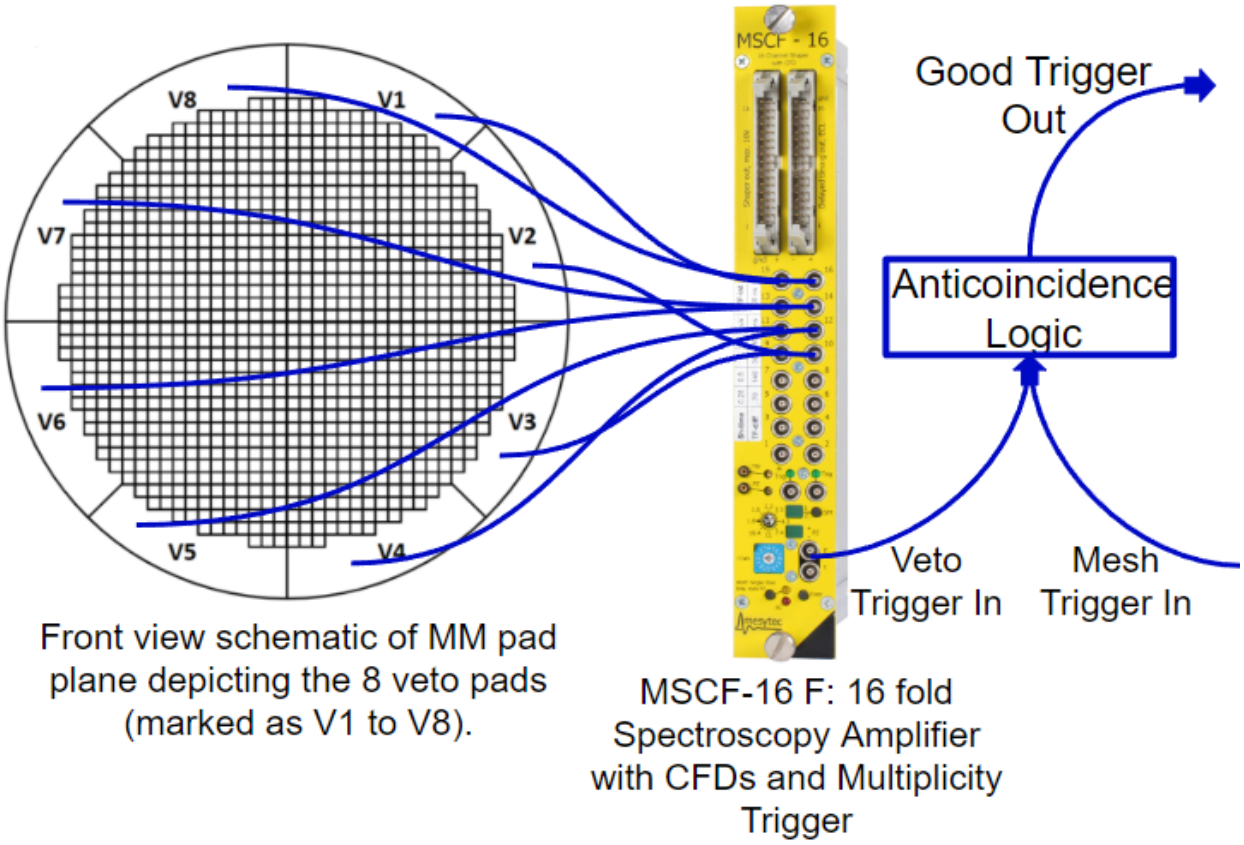

Figure 5.8: Schematic diagram of the front-end trigger veto condition showing the pad plane, connections to the veto pads (marked V1-V8), and the module used to create an output trigger if any signal arrives at the veto pads. The output trigger from the MSCF-16 F module is then placed in anticoincidence with the mesh event trigger.

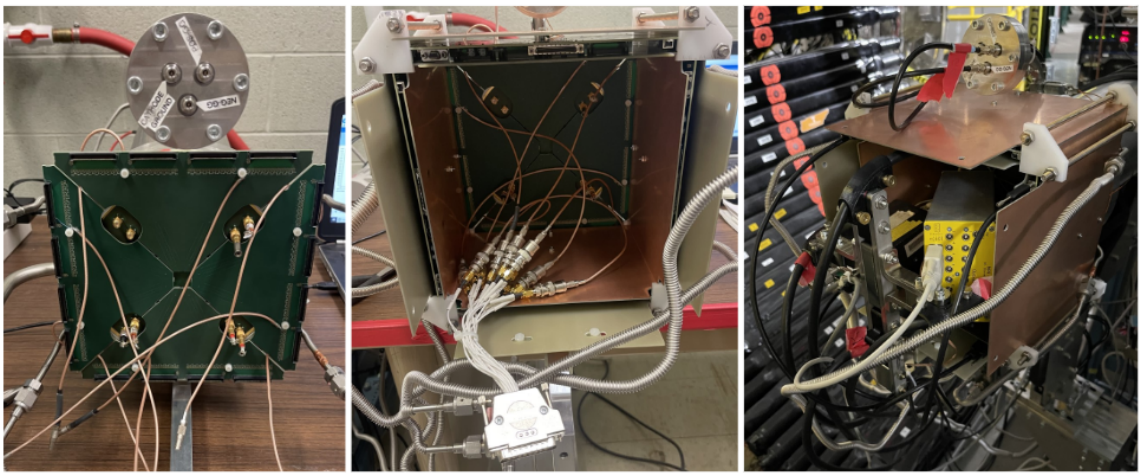

Figure 5.9: Images showing the construction of the front-end veto condition. Left) Image of the soldered lemo connections on the capacitor pads of the zap boards that correspond to each veto pad. Middle) Veto connections integrated into single input for a preamplifier, and AsAd boards are connected with copper shielding. Right) Full AsAd box setup with front-end veto condition fully implemented.

handling system of the TPC (see Chapter 4 for additional details on source tests). Calibration runs were also done for DEGAi using ^{152}Eu and ^{60}Co sources that were taped outside the center of the TPC chamber.

At the commencement of our experimental campaign, diagnostic tests were performed to verify the accuracy of the beam's composition and its precise implantation within the TPC. To tune the beam ranging, we took a pulsed beam at full intensity and observed the $LaBr_3$ detectors to make coarse degrader angle adjustments, aiming for a uniform distribution of gamma counts among them. However, using DEGAi proved to be the most reliable method for adjusting the beam implantation depth, due to it's superior resolution. By plotting the ratio of gamma counts between the upstream and downstream clovers as a function of degrader angle, we determined that an angle of $\sim$25 degrees was optimal for stopping the beam in the center of the TPC. To ensure that the beam was centered on the pad plane, we took data with the TPC and then summed all pad hits across all events. This effectively

generates a heatmap that establishes the xy position of the beam, which showed that the beam spot was indeed centered on the pad plane (see an example in Figure 5.10).

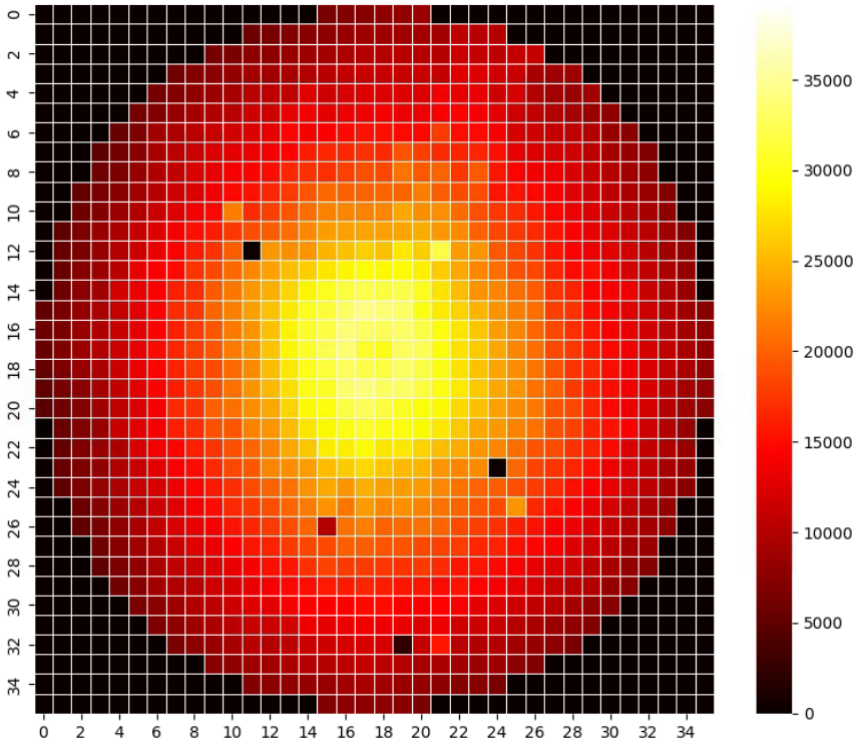

Figure 5.10: Example heatmap used during experiment E21072 to establish the xy position of the beam. The plot is generated with data from the TPC where all pad hits are summed across all events.

To verify that a beam of ^{20}Mg was being delivered, we inserted the Si PIN detector into the beam line and took a continuous beam at 100x rate attenuation. The initial PID plots generated showed significant ^{21}Mg contamination ($\sim$10% the intensity of ^{20}Mg). This was a worrisome contaminant, as it also has a p-α channel at a nearby energy to that of our events-of-interest (^{20}Mg(βpa)), but with a significantly higher branching ratio ($\sim$0.03% of all ^{21}Mg events). However, this proved to be beneficial, effectively serving as a commissioning beam for the detector. It allowed us find p-α events in the data, and show that they had the signature we were expecting. Figure 5.11 shows what is likely a ^{21}Mg p-α found during this commissioning phase. The image shows a clear double peak structure in both the 2D

projected track and the time projection, thus demonstrating that the GADGET II TPC is indeed capable of identifying our events-of-interest.

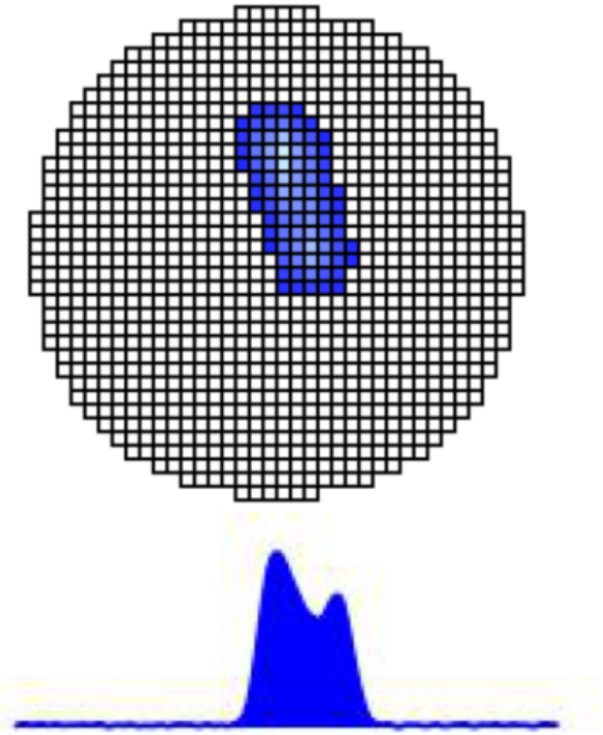

Figure 5.11: The upper panel illustrates the energy deposition in the x-y plane of the GADGET II TPC, highlighting the distinct Bragg peaks indicative of simultaneous proton-alpha particle emission. The lower panel shows the time projection (energy deposition along z), reinforcing the identification of the dual Bragg peaks. These observations strongly suggest the event originates from the beta decay of ^{21}Mg, characterized by a significant ^{21}Mg(βpa) decay pathway.

During this beam sampling, we also encountered an unexpected low beam intensity. Per our proposal, we required >6000 particles per second (pps) of ^{20}Mg deposited in the active region of the TPC during each implantation phase. Additionally, from the Experiment Service Description, we were expecting to have ∼8000 ^{20}Mg particles per second (pps). However, integrating the ^{20}Mg peak on our PID plots showed we were only getting ∼700 pps. After a few days of additional beam tuning efforts, a purely isotonic beam with enhanced intensity was received. The elimination of the ^{21}Mg contamination was corroborated by PID

plots, and the lack of any characteristic ^{21}Mg gammas detected by DEGAi. This cleaned up ^{20}Mg beam was depositing ∼1,800 pps of ^{20}Mg, and our experiment was extended by two days due to the time spent with impure beam, and the insufficient rate.

While the beam rate was greatly improved, given that we are searching for extraordinarily rare events, the reduction in statistics from what we were expecting will likely hinder our ability to make a finite measurement of the ^{19}Ne alpha branching ratio. Had we received the beam intensity we anticipated, we would have expected 40-50 events-of-interest, and the astrophysical problem at hand can be effectively addressed with a branching ratio uncertainty of 50% or less, equating to us finding roughly 4 events-of-interest. However, considering a rough estimate of the integrated beam at this reduced rate, our detector efficiency, and the established upper limit of the branching ratio, we will likely see no more than 4 events-of-interest under the most optimistic scenarios, and 0 based on the lowest estimate of the branching ratio.

With the beam optimized, we focused on calibrating the TPC, experimenting with various voltages applied to the MM DLC to refine the clarity of TPC tracks and enhance the signal-to-noise ratio. Starting with an initial voltage of +380 V, we incrementally increased it by 10 V steps, identifying +440 V as the optimal setting for maximizing gain while minimizing sparking events and noise (see 5.3.1 for additional setup details). Production runs then commenced with minimal interruption except due to periodic PID runs (see 5.3.4), pauses for the liquid nitrogen filling of DEGAi, and occasional beam maintenance.

Chapter 6

Preliminary Analysis of Experimental Data from E21072

6.1 Data Processing

For every decay event that occurs in the GADGET II TPC each CoBo sends a single data frame of pad traces per AsAd (see Section 4.1.2 for details of the GET system). We operated in partial readout mode, so only those pads that are hit have traces that are recorded. Figure 6.1 shows the traces on one AGET chip from a typical TPC event. Each trace spans 512, 10 ns time bins and the integral of each trace is proportional to the energy deposited on each pad, thus, the abscissa of each peak indicates the time of arrival for the charge on that pad.

The trace data from each AsAd is output as a separate raw data file, and these files are subsequently merged and converted to HDF5 files for analysis [69]. During this data transformation channel signals are mapped to the pad plane layout. Additionally, a peak detection algorithm finds the time bucket in which each channel peak is located, then the drift time of the detector is used to extract the z-coordinate for that charge deposition. Once the merge is complete, the resulting HDF5 file contains the x,y,z hit pattern, the max charge per pad, the time of the pad hit, and the summed trace data as an array with 512 elements (one value per time bucket).

These HDF5 files can then be used for several different types of analysis/visualization.

One can use the x,y hit data to construct 2D projection images of particle tracks representing the components transverse to the beam axis. Additionally, by normalizing the charge per event, the relative charge density along the track can be seen. This allows us to see clear Bragg peaks for each event regardless of the total energy of that event (see Figure 4.7).

The reconstruction of the z-coordinate during merging also allows for the visualization of a 3D dimensional point-cloud for the event as can be seen in Figure 4.8. With the point-cloud generated we can then apply outlier removal algorithms to clean up the event tracks. As is detailed in Section 4.2.1, noise reduction was achieved by removing points in the point-cloud from the main track cluster using Hotelling's T-squared and Squared Prediction Error (SPE) algorithms sequentially. The Hotelling method identifies outliers by their significant distance from the mean considering variance, while SPE flags points with high prediction errors. A point in the cloud is considered an outlier only if both methods agree, ensuring accurate elimination of noise, and/or beta particle ionization in the data.

The data can be further cleaned by instituting veto conditions. There are 8 veto pads that surround our main detection pads, and these veto pads are essential for improving data quality. They enable the rejection of events that fall outside the main detection area, ensuring that only events that deposit all of their energy in the main area of the pad plane are analyzed. Throughout the experimental campaign, a front-end veto condition was applied (detailed in Section 5.3.6.1) to preclude numerous events that fell outside this detection area. Despite this measure, some events could still bypass the initial filter, necessitating the exclusion of any event with veto pad signals surpassing a set threshold via software. Additional unwanted events are removed by implementing integrated charge, and track length thresholds, above which the events are removed. This event selection works to eliminate nonphysical events caused by detector noise, such as sparks.

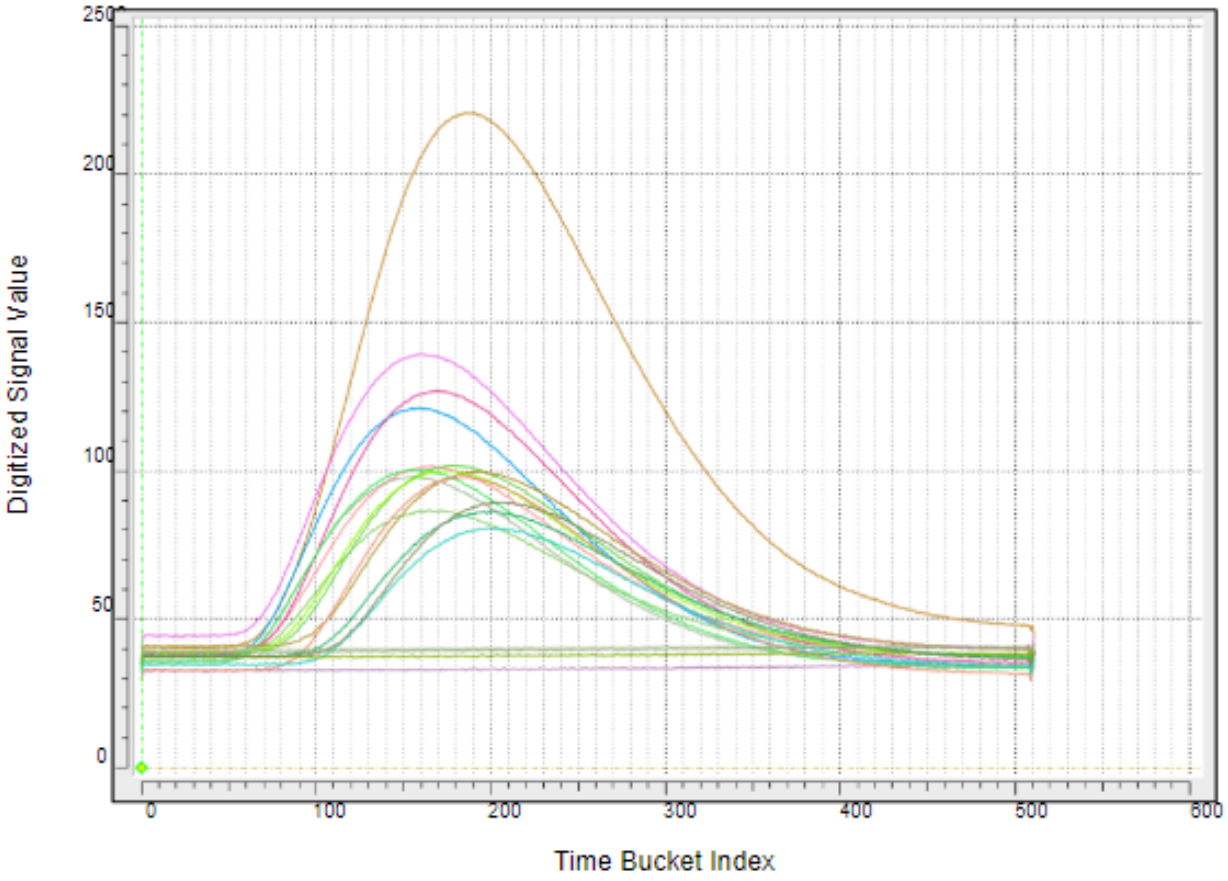

Figure 6.1: Traces on a single AGET chip for a typical TPC event. Each trace represents the signal from one pad. Each trace spans 512, 10 ns time bins and the integral of each trace corresponds to the energy collected.

6.1.1 Improved Point-cloud Reconstruction

The process delineated above constructs the 3D point clouds for our events by creating a point based on the max charge per pad. This means that events that are very perpendicular relative to the pad plane would have very sparse point clouds, which can affect the fitting of their range.

To fix this issue we improved the reconstruction of the z-coordinate by leveraging and modifying software originally developed by the ATTPC group at Michigan State University. This adapted software utilizes a Gaussian Mixture Modeling approach to enhance the z-coordinate reconstructions. This statistical model fits multiple Gaussian distributions to the signal data, effectively capturing the nuances of charge distribution over time. Each Gaussian component can represent a localized charge deposition, with its mean corresponding to the time bucket of peak charge and its variance indicating the spread of the charge distribution. By ensuring the integrated charge of all Gaussians matches the total observed charge, this method not only preserves the total charge information but also enhances the spatial resolution of the reconstructed tracks. We introduced additional routines for interpolating between points on a trace-by-trace basis. This modification significantly improved the reconstruction quality, allowing for the accurate depiction of tracks even for events perpendicular to the pad plane. Figure 6.2 shows a few events that are almost completely perpendicular to the pad plane, and what the point clouds look like before and after this method is applied.

6.2 Energy Spectrum

Among the first data we looked at from the experiment were energy spectra from the TPC. These spectra are generated by integrating the charge from all pads and across all good events

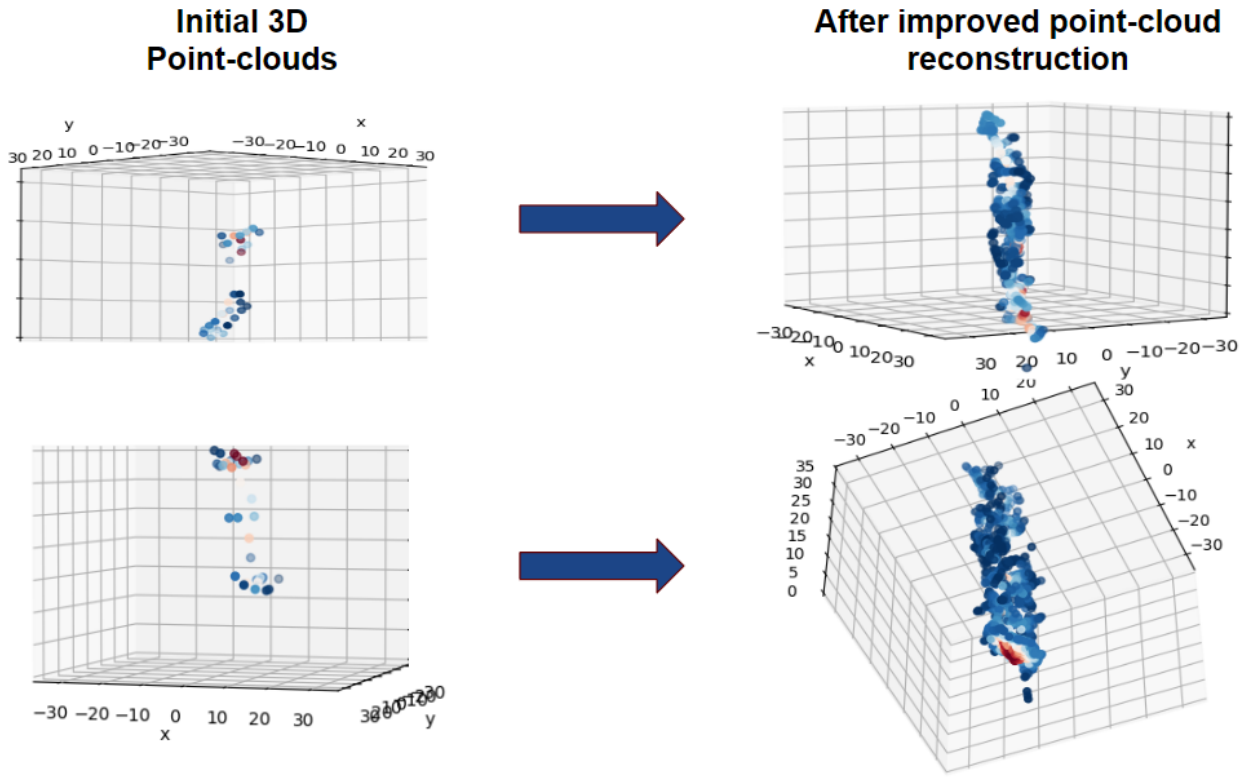

Figure 6.2: Point-cloud representations of particle events in the GADGET II TPC that occurred perpendicular relative to the pad plane (xy-plane). Left) Sparse point-clouds generated using only the max charge per pad. Right) Dense point-clouds generated using a combination of Gaussian Mixture Modeling transforms and additional interpolation routines.

(all veto conditions mentioned above were applied). The main normalization peak in these spectra is the salient ∼800 keV peak. This peak is a beta-delayed proton from ^{20}Mg (see Figure 6.3), it has a well known branching ratio of 11.5%, and we have a near 100% efficiency for detecting them. Integrating this peak for a later experimental run with a purely isotonic beam and improved intensity (Section 5.4), and using the well known branching ratio, shows that a typical run contains ∼500,000 ^{20}Mg decays. From this we can estimate that around 80 x 10^6 ^{20}Mg decay events were recorded in the TPC, with about half of this having been searched for rare events, so far (see Chapter 7). While a precise normalization won't be completed until we finish our rare event search of the data, we can still use this peak to calibrate the energy spectrum.

A calibrated energy spectrum from the TPC can be seen in Figure 6.4. The peaks in the spectrum were modeled using exponentially modified Gaussian functions, and the figure shows a composite function of those fits. This energy spectrum reveals several notable peaks and features that merit discussion. Some of these characteristics are currently under investigation, highlighting the ongoing exploration and analysis efforts in understanding the underlying phenomena. For example, the small shoulder at 0.31 MeV could in part be due to wall-effect, where decays take place close to the TPC's anode or cathode, causing particle tracks to end prematurely, and thus only deposit part of their energy in the active region. Then the event trigger energy threshold causes the shoulder to terminate slightly above zero MeV. But this part of the spectrum requires careful consideration to differentiate between signal and potential background effects.

The peak at 0.43 MeV is attributed with high confidence to the 537 keV ^{16}O recoil, stemming from the E_{cm} = 2.69 MeV beta-delayed alpha emission from ^{20}Na decay [70]. This can occur when neutralization is not fully achieved, and atoms carrying a positive

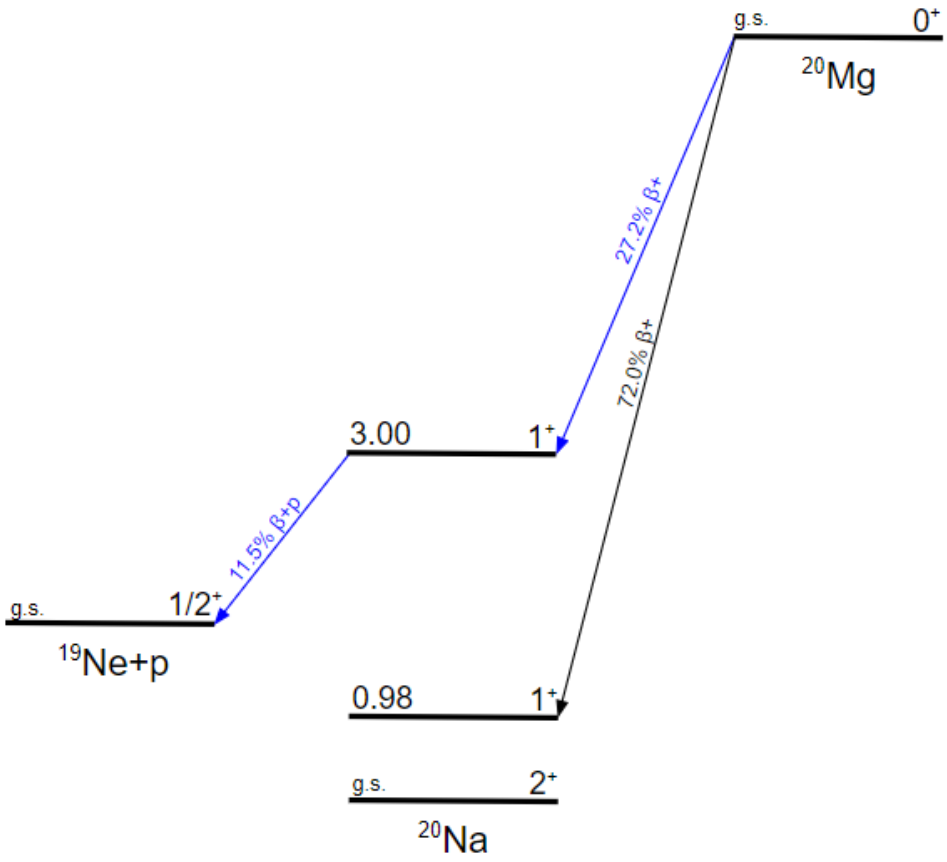

Figure 6.3: Simplified decay scheme showing 797 keV beta-delayed proton from ^{20}Mg, which serves as the main normalization peak in our energy spectrum. Figure adapted from [16].

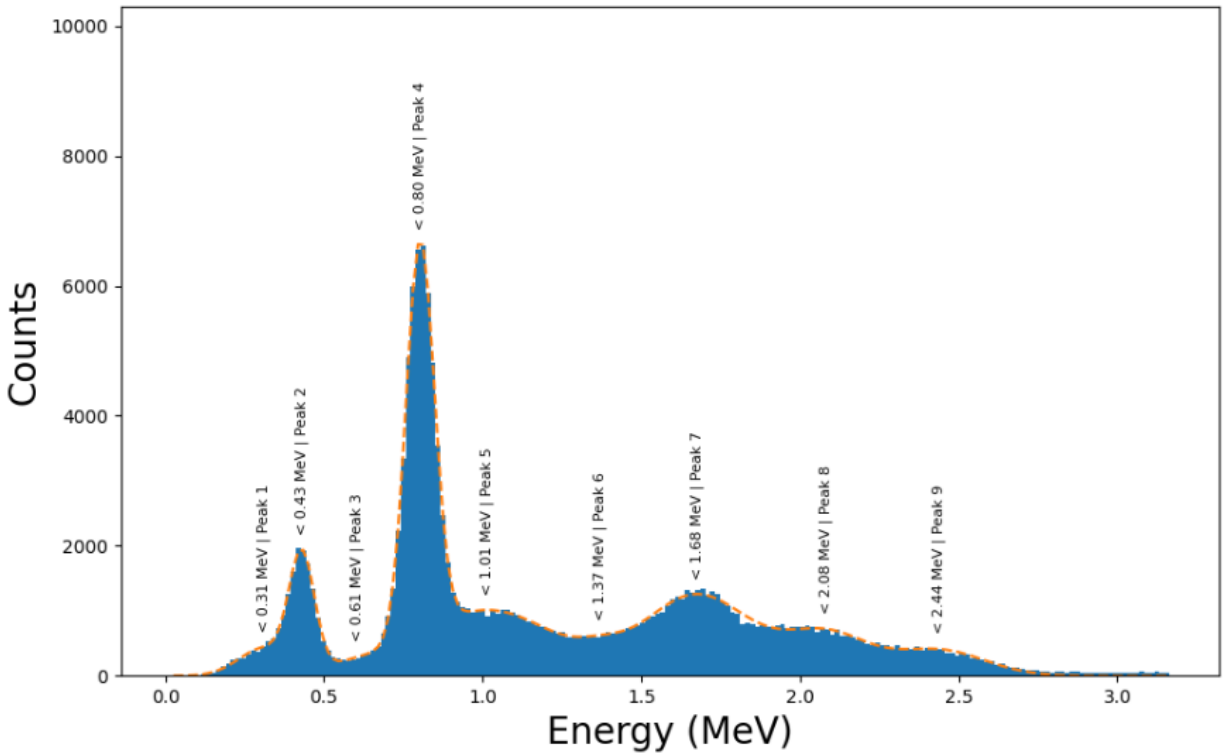

Figure 6.4: Energy spectrum from the TPC representing one hour worth of data taken during experiment E21072. Peaks were fit using exponentially modified Gaussian functions, and the orange dashed line is a composite function of those fits displayed to highlight key features in the spectrum.

charge drift towards, and decay on, the detector's cathode. In these instances, only the energy from either the emitted alpha, or the ^{16}O recoil will deposit energy in the active volume of the TPC (as the decay is back to back). The observed discrepancy in energy can be ascribed to a significant pulse-height defect, which is exacerbated given that these events always drift the full length of the detector. The pulse height defect in gaseous detectors refers to the lower-than-expected electrical signal produced when ionizing radiation is detected, due to energy losses from recombination, attachment, diffusion, excitation of gas molecules, and the presence of quenching gases. These factors prevent some of the energy deposited by ionizing particles from being fully converted into measurable ionization signals, affecting the accuracy of energy measurement and particle identification in radiation detection systems [71]. At the relevant energies there appears to be a ∼100 keV shift down in an energy for heavy recoils, and ∼70 keV shift down for alphas due this effect.

The feature at 1.01 MeV could be a confluence of several phenomena, including the 1056 keV beta-delayed proton from ^{20}Mg and the 1108 keV ^{16}O recoil. The latter originating from the E_{cm} = 5540 keV alpha emission from ^{20}Ne. The slightly lower observed measurement can once again be ascribed to the pulse height defect.

The peak at 1.68 MeV is identified as the well known beta-delayed proton from ^{20}Mg. At 2.08 MeV, the spectrum shows what is likely a single alpha particle resulting from the E_{cm} = 2.69 MeV alpha decay on the cathode. Once again considering the impact of the pulse height defect on the observed energy.

Finally, the feature at 2.44 MeV appears to encapsulate the combined energies of the 0.43 MeV and 2.08 MeV peaks. This suggests it could represent the E_{cm} = 2.69 MeV peak inclusive of both particles—minus the pulse height defect—for ^{20}Na decay occurring within the bulk volume. This interpretation implies a complex interplay of emissions and detector

effects that are crucial for understanding the decay mechanisms at play.

This analysis is ongoing, and the hypotheses outlined above will undergo further examination. This will involve applying gates on protons and alphas within the two-dimensional histograms of range versus energy, as detailed in the subsequent section. Moreover, we will leverage the comprehensive functionalities of the GADGET II system to explore these hypotheses, particularly through the analysis of particle-gamma coincidences. This dual approach aims to provide a thorough investigation of the phenomena under study.

6.2.1 Energy Sharing

A critical aspect of the E21072 analysis involves determining the energy sharing in two-particle events, which is key to identifying the specific type of two-body decay that has occurred. For instance, while $p - \alpha$ decays from ^{20}Mg and ^{21}Mg may occur at similar energies, the energy sharing between the decay particles is markedly different. To glean a preliminary understanding of the energy distribution, one can extract the total energy of an event, fit a 3D point cloud of the event's trajectory, and project the track's energy onto this line. The projection is done with a kernel density estimator with Gaussian kernels. Analysis of the resulting curve yields insight into the energy distribution along the track, shedding light on the energy sharing dynamics in multi-particle events. An illustrative example of this method applied to a ^{21}Mg $p - \alpha$ candidate event from the dataset is depicted in Figure 6.5.

It should be noted, however, that this approach is part of a broader analytical framework. A more detailed analysis, which will utilize the full spectrum of raw data to provide a nuanced quantitative assessment of an event's characteristics, is currently in development. Such comprehensive analysis will be reserved for a select subset of particularly significant events due to its data-intensive nature, while the point-cloud methodology offers efficiency

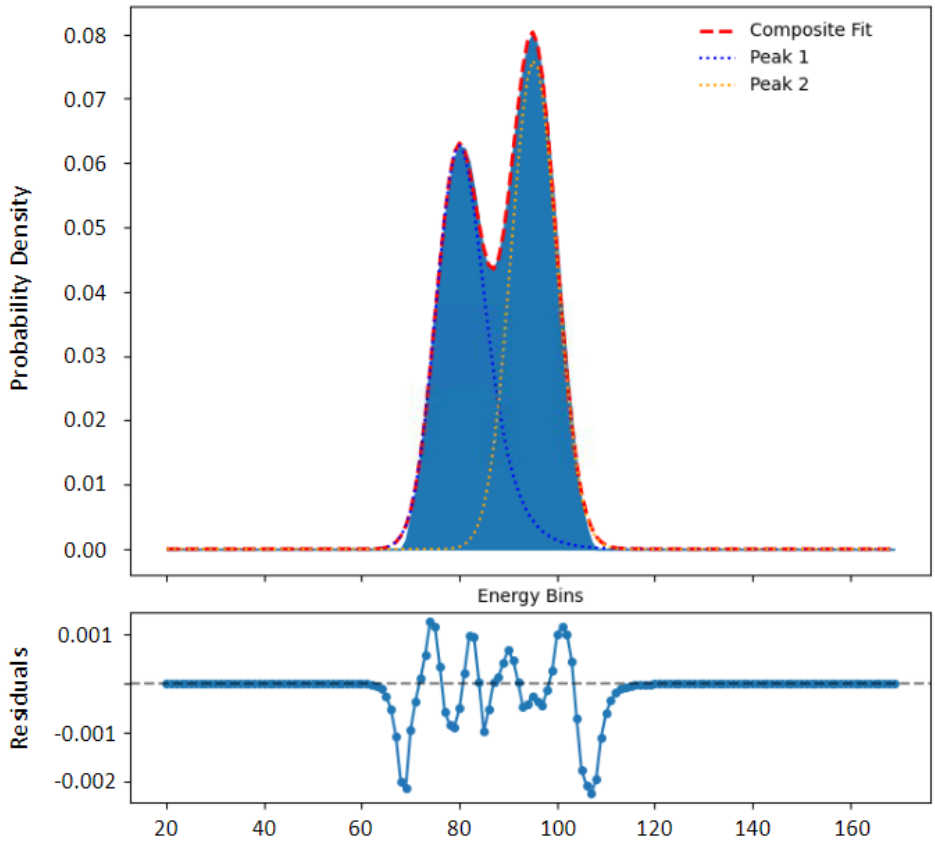

Figure 6.5: Probability density histogram displaying the energy projection onto the point-cloud fit line for a ^{21}Mg $p - \alpha$ candidate, with a total energy of ∼1.78 MeV. The energy contributions of particle 1 (∼860 keV) and particle 2 (∼920 keV) are represented by the blue and orange dotted lines, respectively. The composite fit of the energy distribution is indicated by the red dashed line. Below the main panel are the residuals of the fit.

when dealing with larger datasets.

6.3 Range vs Energy Histogram

As is discussed in Section 4.2.1, Principal Component Analysis (PCA) was utilized to model tracks by determining lines and planes that optimally represent the data through least squares optimization. Within this framework, the primary and secondary principal components represent the track's length and width, respectively. The track length is determined, followed by the aggregation of charge across all pads, which is subsequently converted into energy. With the range and energy of each event determined we can generate a range vs energy histogram from the experimental data.

Figure 6.6 represents such a plot, derived from a single, 1 hour run from experiment E21072. This plot illustrates how decay events manifest as densely populated clusters in both range and energy. As a result, range vs. energy plots serve as a potent tool for gating on specific decay events. Additionally, protons and alphas form distinctive bands on these plots, reflecting their unique interactions with the gaseous medium based on differences in mass and charge. Importantly, this characteristic separation gives us a powerful method for defining a search region to find our events-of-interest that must lie between these bands. This capability is further explored in the following subsection (Section 6.3.1).

Additionally, comparative analyses of range versus energy histograms, as a function of the event angle relative to the pad plane, provide significant insights. Figure 6.7 exhibits a sequence of range-energy histograms from a single experimental run. Each histogram represents a distinct angular segment, demarcated by 10° intervals, with the complete series spanning from 0° to 90°. These histograms illustrate that events with higher energies, which

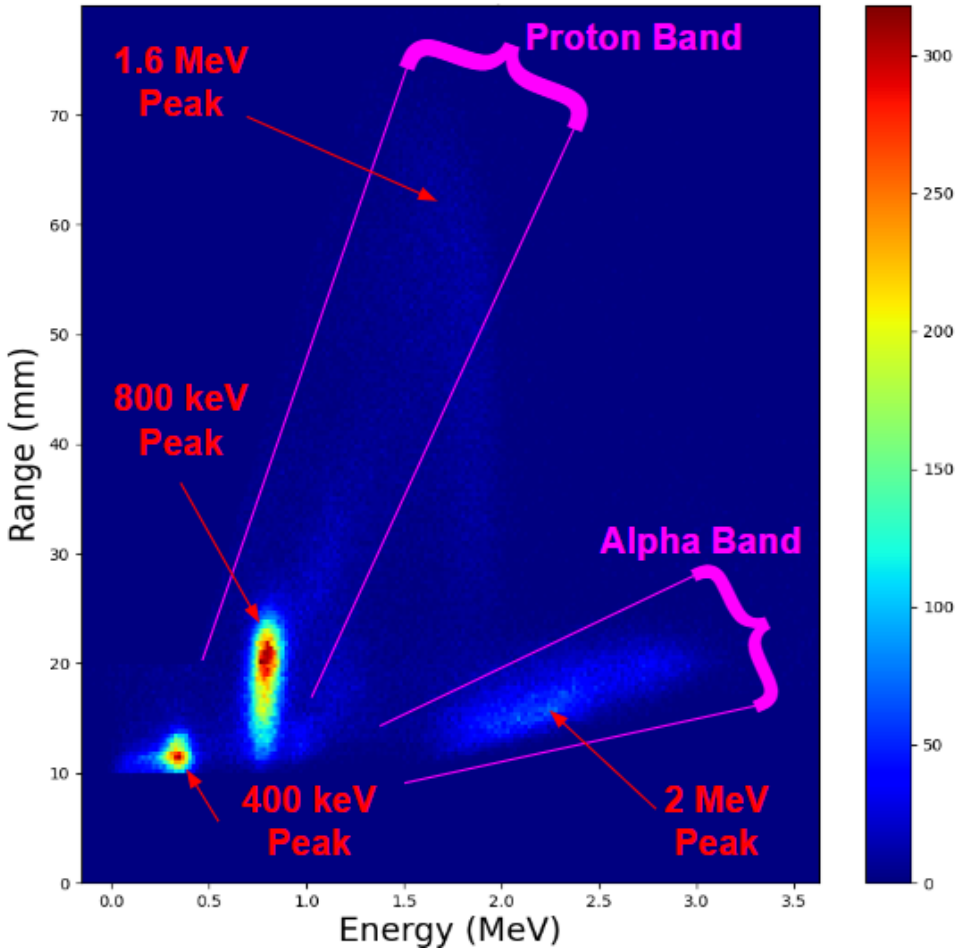

Figure 6.6: Range vs Energy Plot for Experiment 21072 (1 hr run) in linear scale. A few key peaks are highlighted via red arrows, and the distinct proton and alpha bands are marked-out with purple lines.

correspond to elongated particle trajectories, are predominantly observed at more acute angles. This observation is due to the increasing likelihood for longer tracks to be vetoed the more parallel they are with respect to the pad plane. Consequently, events of higher energies tend to exhibit diminished range resolution. This effect arises because the resolution in the xy-plane surpasses that of the z-axis, the latter of which relies on the reconstruction of the z-coordinate. This effect causes the range distribution to be more smeared out for longer tracks as can be seen in Figure 6.8.

6.3.1 Search Region

The ultimate goal of experiment E21072 is to measure $^{20}\mathrm{Mg}(\beta p\alpha)^{15}\mathrm{O}$ events, through the key $^{15}\mathrm{O}(\alpha,\gamma)^{19}\mathrm{Ne}$ resonance. This process is marked by the near-simultaneous emission of a proton and an alpha particle (Ch. 3). The proton energy in this coincidence event is expected to be $1.21^{+0.25}_{-0.22}$ MeV [17]. This was determined previously by analyzing the Doppler-broadened 4.03 MeV gamma peak from the recoiling ^{19}Ne nucleus. By simulating this broadened gamma peak and adjusting the proton energy in the simulations to match the observed data, the energy of the emitted proton from ^{20}Na could be inferred (see Figure 6.9). These protons will have a range in 800 Torr P10 gas of 2-3 cm. The alpha particles in the coincidence event, along with the corresponding ^{15}O recoils, will deposit a total energy 506 keV over a extremely short range (<4mm). Given the energies and ranges of the particles, an identifying feature of the events-of-interest is the ratio of the track length to the total energy deposited, which is distinct from single-proton $\left(^{20}\mathrm{Mg}(\beta p)\right)$ and single-alpha $\left(^{20}\mathrm{Mg}(\beta\alpha)\right)$ events. Thus, these $p{-}\alpha$ events occupy a specific region on the range vs. energy plot, nestled between the distinctly separate proton and alpha bands as illustrated in Figure 6.6. As such, we can apply a well defined search region to the range vs energy histogram based on this

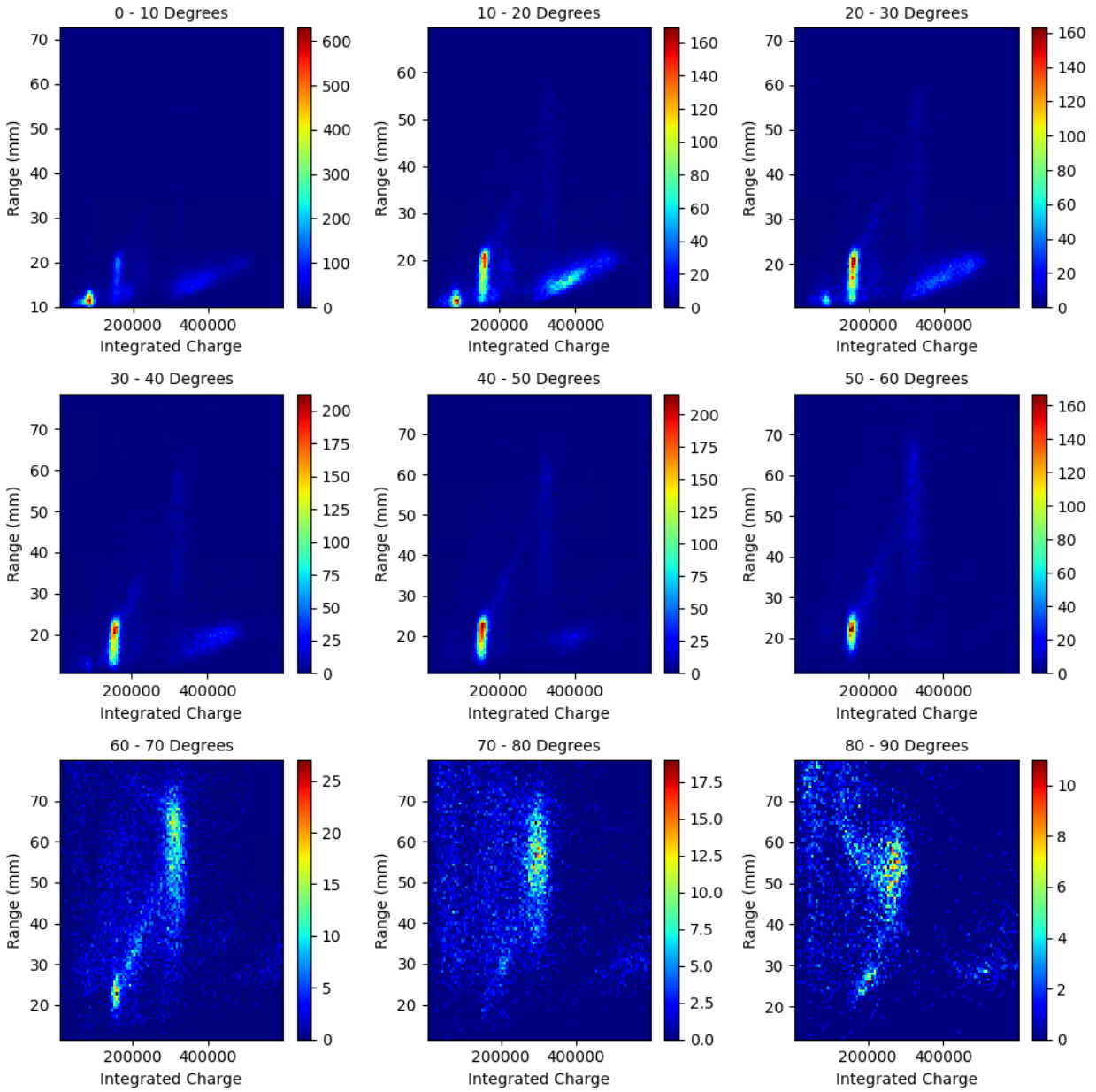

Figure 6.7: Range vs energy histograms for event tracks oriented between 0° to 90° with respect to the pad plane by applying angular cuts of 10°. Note that longer range events are more prevalent at higher angles as they are less likely to be vetoed when more perpendicular to the pad plane.

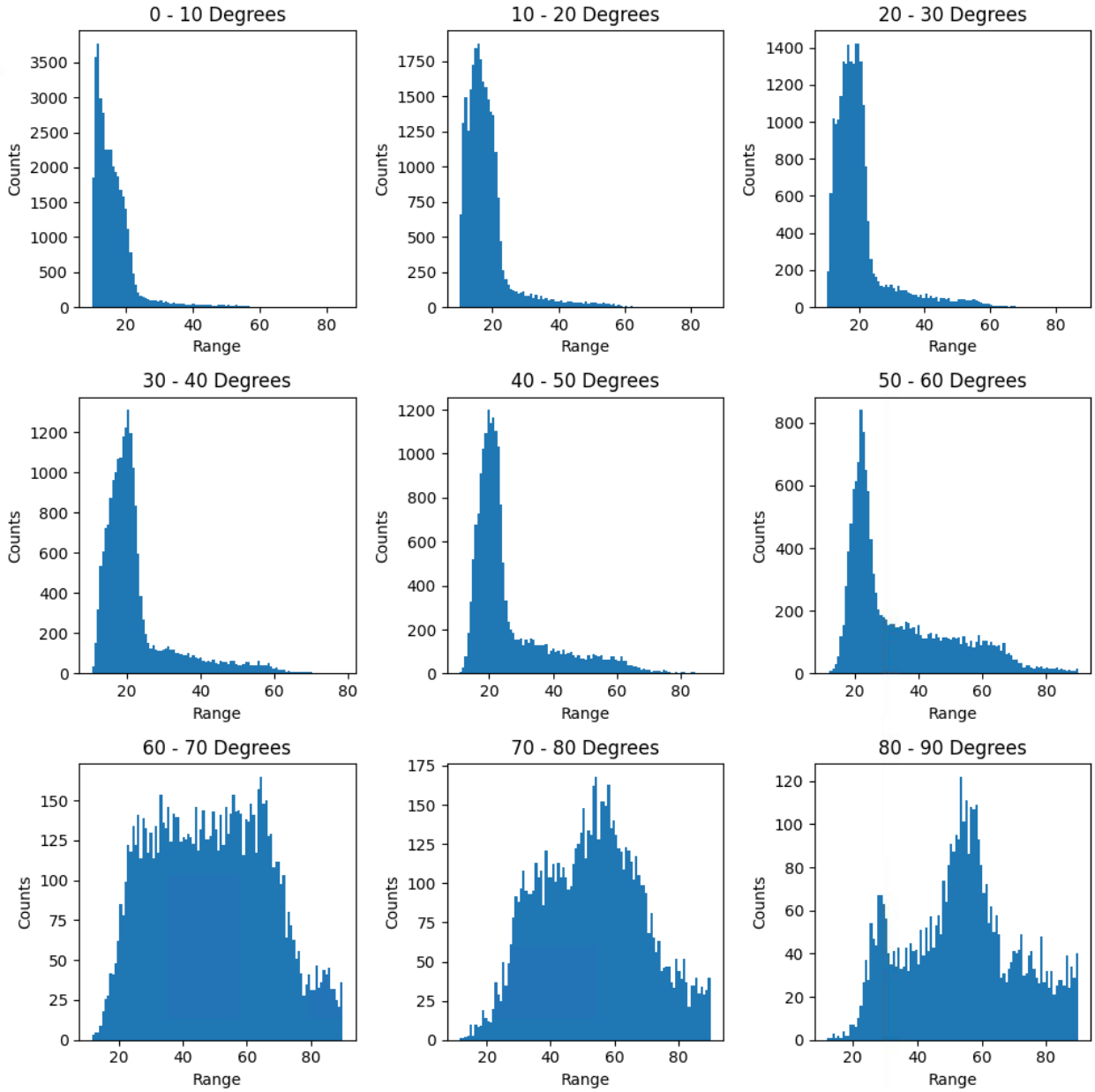

Figure 6.8: Composite of range histograms from a single experimental run, organized into a grid. Each histogram corresponds to a different 10° angular segment relative to the pad plane, ranging from 0° to 90°. The figure demonstrates a more confined range distribution for events occurring parallel to the pad plane, as their range is determined predominantly from the xy-plane measurements. In contrast, events at steeper angles exhibit broader distributions, indicative of longer tracks that necessitate substantial z-coordinate reconstruction, leading to a spread or smearing effect in the observed range.

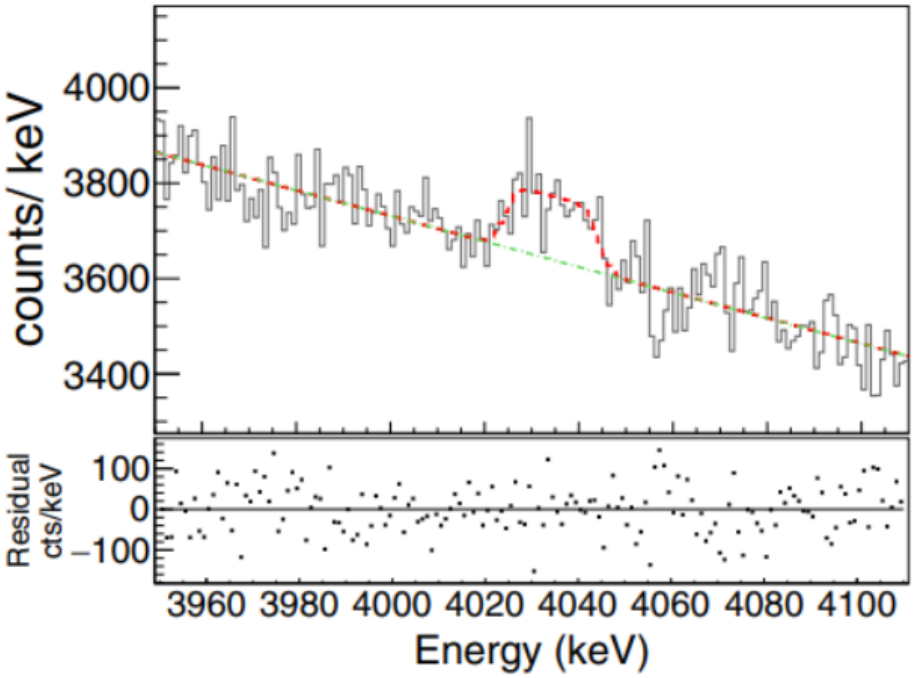

Figure 6.9: Upper panel: A 4.03 MeV Doppler-broadened gamma peak fit with the 1.21 MeV CoM energy. Lower panel: Displays residuals from subtracting the fit function from the data. Figure from [17].

ratio and the expected total energy of 1.7 MeV. Only searching for our events-of-interest in this region eliminates the vast majority of background events (>95%). Figure 6.10 shows such a search region that extends 2 standard deviations in both range and energy.

Even though defining this search region markedly narrows down the volume of data we must sift through to isolate the $p - \alpha$ events, the remaining dataset is still substantial, demanding significant human effort for manual examination. This challenge presents an ideal opportunity to employ machine learning techniques to streamline our search process. The application of machine learning algorithms in enhancing our search efficiency is explored in depth in the subsequent chapter (Ch. 7).

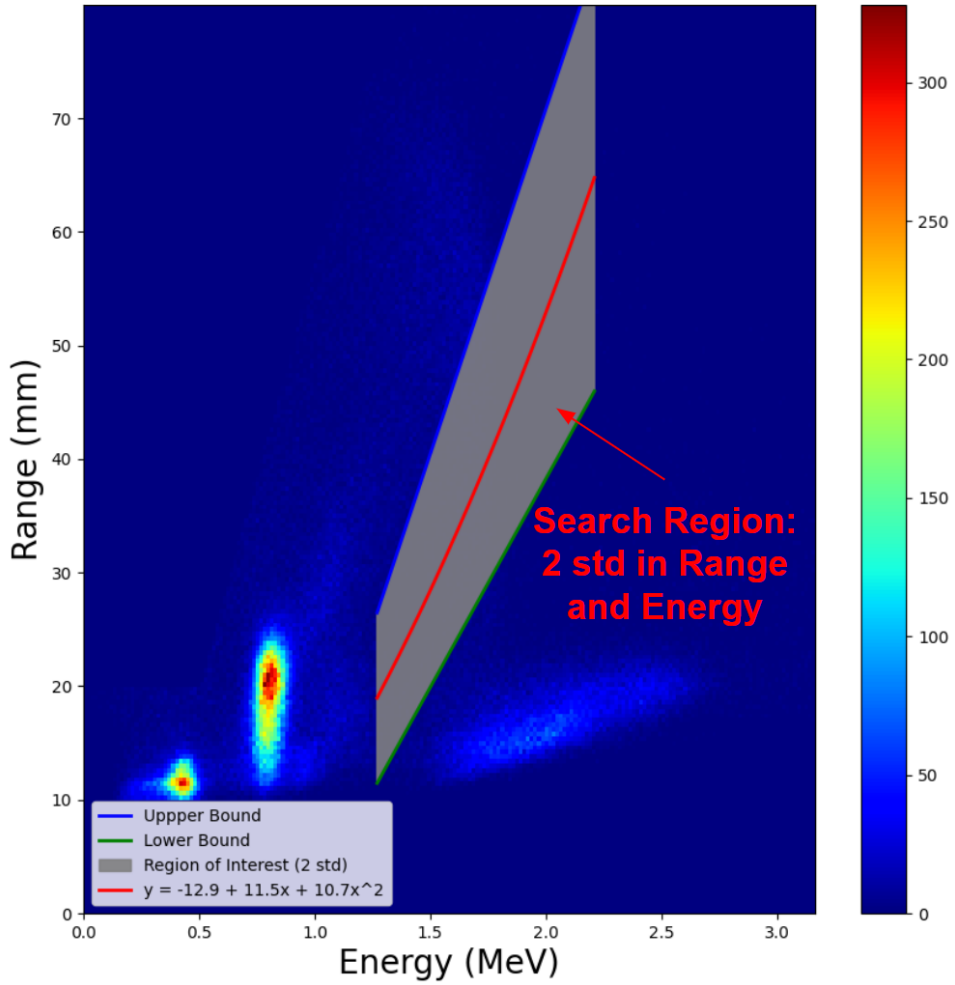

Figure 6.10: Range vs. Energy Plot for Experiment 21072 (1-hour run) displayed on a linear scale. The plot illustrates the designated search region, encompassing 2 standard deviations in both range and energy dimensions. This search region is targeted for isolating $p-\alpha$ events of interest within the dataset.

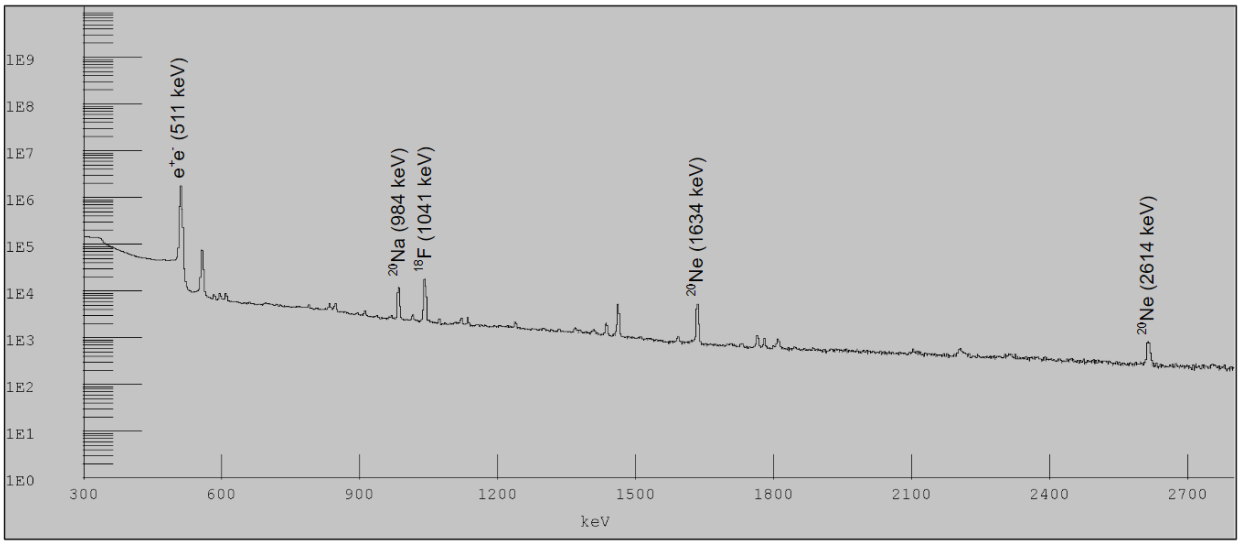

Figure 6.11: Calibrated gamma spectrum taken with DEGAi over 1 run. Prominent peaks associated with the decay of ^{20}Mg are identified and annotated.

6.4 Gamma Spectrum

The experimental setup for E21072 utilized the GADGET II TPC (with a mesh trigger), surrounded by DEGAi for gamma-ray detection. The calibration of the germanium detector array was accomplished using ^{152}Eu and ^{60}Co sources, which were affixed to the exterior of the central region of the TPC chamber.

A calibrated gamma spectrum from 1 run (1 hour worth of data) can be seen in Figure 6.11. A few key peaks from ^{20}Mg decay are labeled in the spectrum, including the prominent 984 keV gamma from ^{20}Na, and two well known peaks from ^{20}Ne that occur following the beta-plus decay of ^{20}Na.

To ensure that the ^{20}Mg beam used during the experiment was in fact being deposited in the center of the active volume, we can view the mesh trigger - gamma time distribution, as can be seen in Figure 6.12. This time distribution was recorded in 100 ns intervals. The resulting dataset was categorized into three subsets: the total count spectrum (red), events gated on the 511 keV gamma peak indicative of positron annihilation (blue), and events

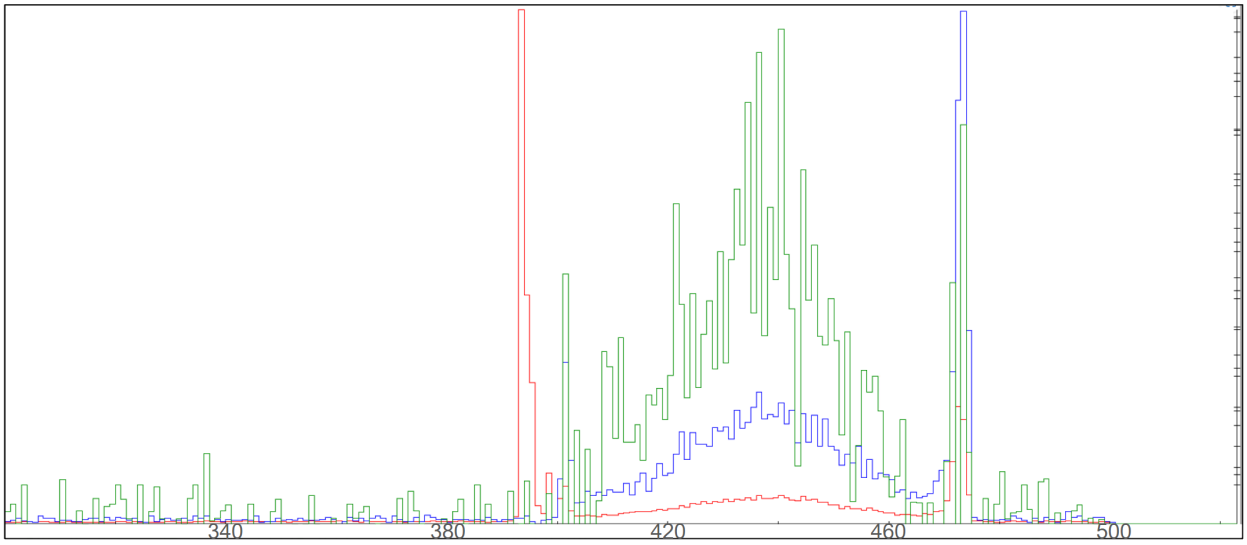

Figure 6.12: Mesh trigger - gamma time distribution from experimental Runs 85-86 using the DEGAi setup. The data, binned at 100 ns per channel is shown with the total event count (red), events gated on 511 keV gamma rays (blue), and events gated on the sum of 238, 275, and 1298 keV gamma rays (green). Channel 400 represents the zero-time reference point, and the TPC's ion centering is evidenced by distribution peaks at 3.6 microseconds.

gated on the combined energies of 238, 275, and 1298 keV gamma rays (green), which are characteristic of specific nuclear transitions in the decay of ^{20}Mg. The time calibration was centered at channel 400, designated as "zero," which means the TPC cathode signal would occur at 7.2 microseconds (the drift time of the detector), equivalent to channel 472. The centered distribution of the gates at 3.6 microseconds suggests that there was optimal ion placement within the center of TPC.

All the gamma spectra from the experiment are in the process of being sorted, calibrated, and analyzed. Part of this analysis will include looking at particle-gamma coincidences by gating on certain energies. For example, we plan to gate on the 4.03 MeV characteristic gamma from ^{19}Ne. Looking at the proton spectrum in coincidence with this prompt-gamma should allow for a more precise measurement of the ^{20}Na proton feeding this astrophysically important state.

6.5 Analysis Software Development

To enhance the efficiency of analyzing TPC data, we developed a software analysis tool. Figure 6.13 showcases the main interface of this analysis framework. The interface is organized with the primary analysis categories on the left in what we will refer to as the navigation column, and corresponding sub-options emerge on the right upon selection of a main category (see Figure 6.14). The tool offers flexibility in data handling, allowing for individual run analysis or aggregate analysis through the "Sum Runs" feature located at the base of the navigation column. After inputting a run number(s), the "Create New Files" radio button is enabled, facilitating the pre-processing of the data via the application of length and integrated charge vetoes, pad and point cloud thresholds, and outlier parameter adjustments. The pre-processed files are organized and saved in a directory reflecting the selected parameters. Once these files are generated, choosing the "Use Existing Files" option enables the selection of a directory containing pre-processed data. This action unlocks the full suite of functionalities available in the navigation column, with further details provided below:

Energy Spectrum: The "Energy Spectrum" feature offers a user-friendly interface for generating energy histograms. Users can specify the desired number of bins for the histogram and initiate the generation process by clicking "Generate Spectrum." Additional customization includes setting lower and upper threshold values, which are visualized on the plot as two vertical lines, alongside a count of the data points within the selected range.

For peak analysis, the "Quick Gaussian Fit" option provides an expedited method to fit a Gaussian to any peak within the selected range. For a more detailed analysis, the "Initial Guesses for Multi-peak Fit" feature enables users to engage directly with the plot.

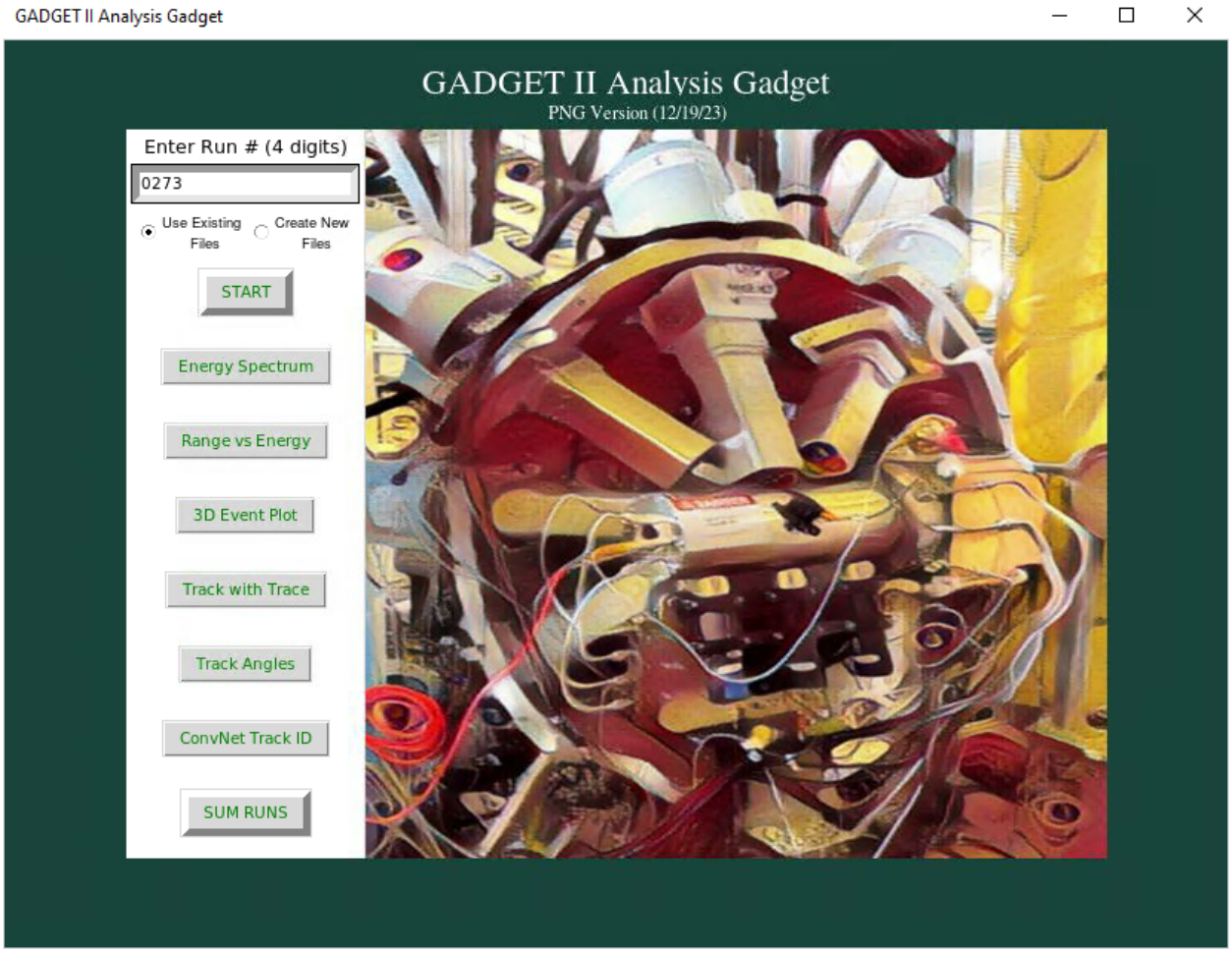

Figure 6.13: Main view of the GADGET II TPC analysis interface. Individual runs can be analyzed (as is the case for run 273 in the image), or runs can be compiled via the "Sum Runs" button at the bottom of the navigation column. Each option in the navigation column opens up additional analysis features in that context on the righ-side of the interface (see Figure 6.14).

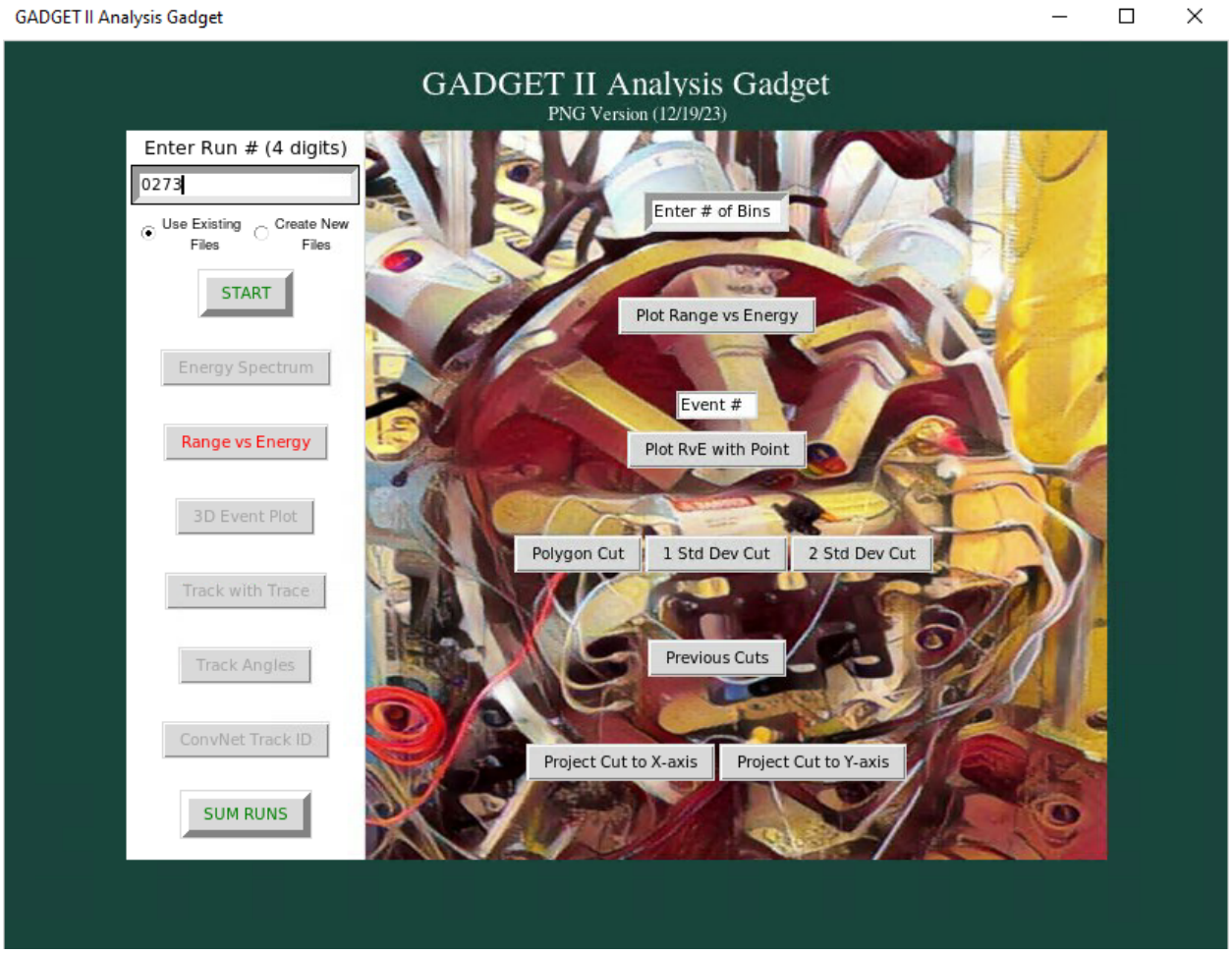

Figure 6.14: An example of sub-options that are available when selecting a main option from the navigation column. In this case "Range vs Energy" is selected allowing for the creation of a range vs energy plot, plotting a point on that plot, applying a polygon or static cut on the plot, viewing previous cuts, or projecting cuts to an axis for fitting and resolution determination.

By actively clicking on the plot, users can set initial guesses for the peak parameters, such as peak amplitude and standard deviation. This interactive method significantly enhances the fitting process by allowing precise and intuitive placement of initial guesses. The chosen fitting functions and the user-defined initial parameters facilitate a tailored fitting experience. The output is a plot with all identified peaks clearly labeled, and the corresponding fit parameters are exported to a separate file for in-depth analysis. The output fit parameter file can be re-imported to refine fits or adjust parameters, with the option to fix specific parameters by marking them with an asterisk. These features ensure a comprehensive and flexible approach to spectrum analysis, catering to both quick assessments and detailed multi-peak fitting.

Range vs Energy: The "Range vs Energy" feature provides a dynamic interface for creating two-dimensional histograms of range versus energy. Users can define the desired number of bins for this histogram and then generate the visualization by clicking the "Plot Range vs Energy" button. A notable feature allows for the input of specific event number(s), which are then highlighted on the histogram, aiding in the identification of their positions within the 2D plot.

A particularly versatile functionality is the "Polygon Cut" option. Activating this feature opens the range vs energy plot, where users can interactively draw a polygon directly on the plot to define a custom selection region. Only data within this polygonal boundary will be selected for further analysis. The software then proceeds to generate data-fused images for the selected events (detailed in Section 7.0.6), which are displayed in an intuitive viewer. This viewer displays both individual images and grid views of the images, and allows you to flag and store any interesting events, enhancing the examination process.

Moreover, the interface includes predefined "1 Std. Cut" and "2 Std. Cut" buttons for

quickly applying standard deviation-based selection criteria, aligning with the search regions discussed in Section 6.3.1. Users have the flexibility to navigate through previously applied cuts, revisiting selected events or projecting the cut data onto the x or y axis for detailed fitting analysis. This capability not only streamlines the identification of relevant data points but also facilitates the derivation of resolutions from the processed data.

3D Event Plot: The "3D Event" feature offers a way to explore individual events within the dataset through 3D visualization. Upon specifying an event number, users can generate and view the event's 3D point cloud representation. Two visualization options are available to cater to different analysis needs. The "Original 3D Point Cloud" option presents the event's point cloud as reconstructed from the HDF5 file, offering a direct view of the spatial distribution captured during the experiment (refer to Section 6.1.1 for details on point cloud reconstruction). Whereas the "Enhanced 3D Point Cloud" option offers a more refined visualization, as it applies additional interpolation techniques to the original point cloud data. The result is a denser and smoother point cloud that outlines the event's tracks with greater continuity and clarity.

Figure 6.15 illustrates a comparison between these two point cloud visualizations for a proton track event. This capability not only enhances the visual examination of the data but also aids in the qualitative assessment of event characteristics.

Track with Trace: The "Track with Trace" feature enables users to delve into the analysis of specific events by generating data-fused images, as detailed in Section 7.0.6. This tool not only visualizes the event but also offers advanced functionality for analyzing the temporal dynamics of particle tracks.

Upon selecting an event, users can engage in interactive analysis by fitting the trace, or time projection, of the event. This is accomplished by clicking directly on the histogram,

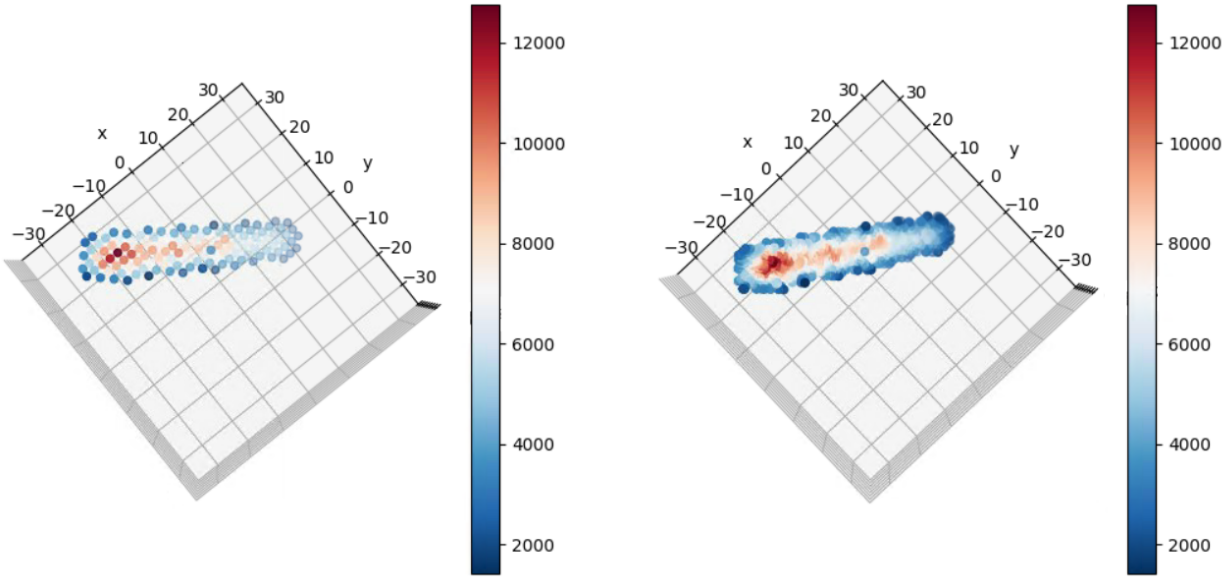

Figure 6.15: 3D point clouds for a typical proton track from experiment E21072. Left) Original point cloud from HDF5 file generated after point cloud reconstruction. Right) Dense point cloud that implements additional interpolation to improve 3D visualization.

allowing for the intuitive placement of initial guesses for the fit parameters. This hands-on approach facilitates a preliminary understanding of the event's structure and dynamics.

Moreover, the feature extends to fitting the particle track itself, enabling the projection of the track's energy onto the fitted line. Analyzing the resultant curve provides insights into the energy distribution along the track, which is particularly useful for understanding energy sharing between two particles in events involving multiple particle emissions.

Track Angles: The "Track Angles" feature enables the examination of energy spectra and range versus energy plots through the lens of angular distribution. Users have the flexibility to either define a specific angular range for detailed analysis or to explore a comprehensive overview of the data across varying angles via a systematic grid of images.

This function allows for the investigation of how events vary as a function of angle with respect to the pad plane, providing insights into the directional dependence of these events.

For instance, users can generate and compare histograms for different angular segments, offering a visual representation of the angular dependence of range and energy. As an illustrative example, Figure 6.7 presents range versus energy histograms from a single run, where each plot is segmented into 10° angular intervals ranging from 0° to 90° relative to the pad plane. This is valuable as

ConvNet Track ID: The "ConvNet Track ID" feature introduces a powerful application of machine learning to the analysis process, specifically utilizing Convolutional Neural Networks (CNNs) for event classification. Upon selecting a subset of the data via previously established cuts, users have the option to employ either a single CNN model or an ensemble of CNNs, detailed in Section 2, to automatically process and classify data-fused images associated with the subset (refer to Section 7.0.6). This process is fully automated, with the CNNs evaluating each image to determine its likelihood of belonging to predefined classes.

Following the classification process, the interface dynamically updates to present a series of buttons, each representing a different event class as determined by the CNN model(s). Users can then interact with these buttons to filter and visually inspect all images predicted to belong to a particular class, facilitating an efficient review and further analysis of the data.

This integration of ConvNet technology with the analysis software streamlines the classification and review process, significantly enhancing the ability to quickly identify and categorize complex event patterns within the data. This method not only accelerates the analysis but also improves the accuracy of event classification, leveraging the sophisticated pattern recognition capabilities of CNNs.

Chapter 7

Rare Event Search Using 2D Convolutional Neural Networks

One of the main goals of experiment E21072 is detecting rare two-particle events, namely, $^{20}\mathrm{Mg}(\beta p\alpha)^{15}\mathrm{O}$ events. In the following sections a novel approach for finding these rare events will be described. This includes methods for leveraging Convolutional Neural Networks (CNNs) alongside various data processing techniques (for details on how CNNs work see Ch. 2). Our approach employs early data fusion strategies to take advantage of the different TPC data modalities, converting 3D TPC tracks into 2D representations that still capture all the relevant features of the 3D topology. This adaptation facilitates the use of computationally efficient 2D CNNs while also allowing us to leverage an extensive collection of pre-trained models.

Recognizing the limitations posed by the rare nature of the events under investigation and the risk of discrepancies arising from heavy reliance on simulated data, our methodology incorporates a layered approach. To enrich our training dataset we utilize techniques such as active learning and iterative reinforcement. Additionally, to maximize the utility of each genuine two-particle event within our training data, we apply custom data augmentation techniques.

In order to effectively use simulations in the training data, we introduce perturbations

into our simulations to account for physics parameter and detector response uncertainties, thereby enhancing the model's adaptability to differences between simulated and real-world data. In parallel, we refine our training methodologies to produce CNNs that act as highly discerning filters for our events-of-interest. This includes training with data that, while not directly representing our target events, exhibits characteristics suggestive of such events, ensuring that even the most subtly indicative events are captured for detailed interrogation by humans. As a result, we develop models that excel in identifying rare two-particle events.

The subsequent sections/subsections are adapted from our other work that is currently in preparation [26]. These adaptations are used with permission and have been modified to fit the context of this thesis.

7.0.1 Addressing Class Imbalance

Within our TPC data, the rare two-particle events we seek are vastly outnumbered by more common occurrences. This imbalance presents a significant hurdle, as models trained on such skewed datasets can become biased toward the more prevalent class, thereby neglecting the less common but critically important events. To counteract this, we implement two main approaches: class reweighting and selective data sampling.

Class Reweighting: Given the paramount importance of accurately identifying rare events, we can significantly enhance the impact of these occurrences within our model's learning process by applying a disproportionately high weight factor to the minority class [72]. This strategic reweighting serves to intensify the consequences of incorrectly classifying these pivotal events. By imposing a substantial penalty for each misclassification of rare events, we effectively compel the model to allocate more focus and resources towards understanding the unique characteristics and subtle indicators of these events. Such a deliberate

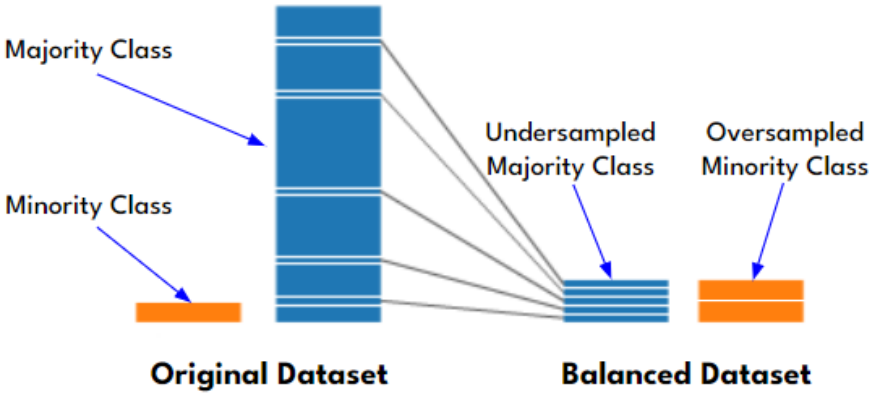

Figure 7.1: A figure showing the balancing of a training dataset through oversampling of the minority class (rare events) and undersampling the majority class.

adjustment in the learning dynamics is instrumental in guiding the model to achieve a deeper comprehension of the rare event features, thereby enhancing its overall detection capability.

Balancing Through Sampling: We adopt a dual approach of oversampling the minority class and undersampling the majority class to cultivate a balanced training environment. Augmenting the minority class through oversampling ensures that the dataset is replete with examples of the events-of-interest for the model to learn from. However, it is important to note that excessive oversampling will lead to overfitting, where the model performs well on the training data but poorly on new, unseen data [72]. Thus, finding the optimal amount of oversampling is a delicate process that requires meticulous experimentation and validation. Simultaneously, reducing the prevalence of the majority class via undersampling helps in diminishing its overwhelming influence on model training. The undersampling is done by taking random subsets of the majority class such that the total data across all subsets is equal to the amount of data in the over sampled minority class. This balanced approach is depicted in Figure 7.1, showcasing how oversampling and undersampling are used to create a balanced dataset which mitigates the issues of imbalanced classes.

7.0.2 Active Learning

Active learning emerges as a pivotal strategy once a model demonstrates a basic proficiency in making predictions, serving to further enhance its accuracy. This technique empowers the model to sift through a reservoir of unlabeled data and earmark instances its uncertain about for closer scrutiny. Concentrating on these ambiguous events allows for targeted improvements in areas where the model stands to gain the most from additional information. This approach is exceptionally beneficial in scenarios where acquiring labeled data is a challenge, either due to scarcity or the high cost of labeling, by ensuring that the labeling efforts are directed towards the most impactful samples [73].

Upon identification, these instances are subjected to expert review for correct labeling, embedding human expertise into the loop to resolve the model's uncertainties. This integration of newly labeled data back into the training corpus enables the model to evolve, learning from its prior uncertainties to enhance its comprehension iteratively. This process, as illustrated in Figure 7.2, not only enriches the pool of labeled data but also methodically fine-tunes the model's performance by continuously adapting and refining its predictions.

7.0.3 Ensemble Method

Ensemble techniques stand out in the realm of machine learning for their capacity to amalgamate the unique capabilities of various models, thereby surpassing the performance that any individual model could achieve on its own [74]. For our problem, the strategy involves the parallel training of several models, each on a distinct partition (different random subsets) of the majority class alongside the complete set of the minority class, as illustrated in Figure 7.3. The essence of an ensemble's advantage lies in the diversity it brings into play: disparate

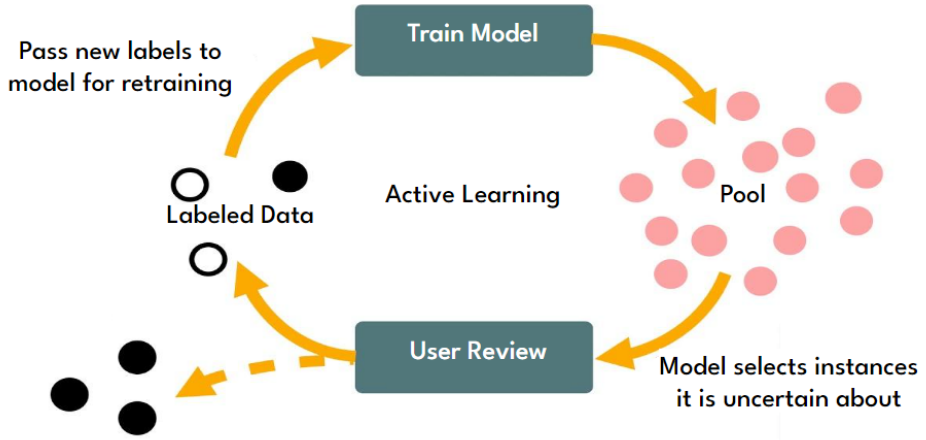

Figure 7.2: Illustration of the Active Learning Process. This figure demonstrates the cyclic nature of active learning: beginning with the model's application to unlabeled data, identifying uncertain instances, which are then evaluated and labeled by specialists. This freshly labeled data is reincorporated into the training dataset, enabling the model to refine its predictions through successive training cycles. Figure adapted from [18].

models can elucidate different facets of the dataset, and when their predictions are pooled, the outcome tends to be more comprehensive and precise. Additionally, because prediction is aggregated across models, this method works to eliminate individual model bias.

Although ensemble methods necessitate additional computational resources, the improvement in detection accuracy they facilitate is frequently a worthwhile trade-off, especially in scenarios where achieving a high detection rate is crucial.

7.0.4 Simulating Events

To augment our training dataset and bolster the accuracy of our CNNs, we integrate simulated events into the data pool. These simulations, crafted to closely emulate real decay events observed in the GADGET II TPC, are generated with the ATTPCROOTv2 analysis framework. This framework was developed by the ATTPC group at MSU, and is built atop the foundations provided by the FairSoft and FairRoot suites, drawing upon established nu-

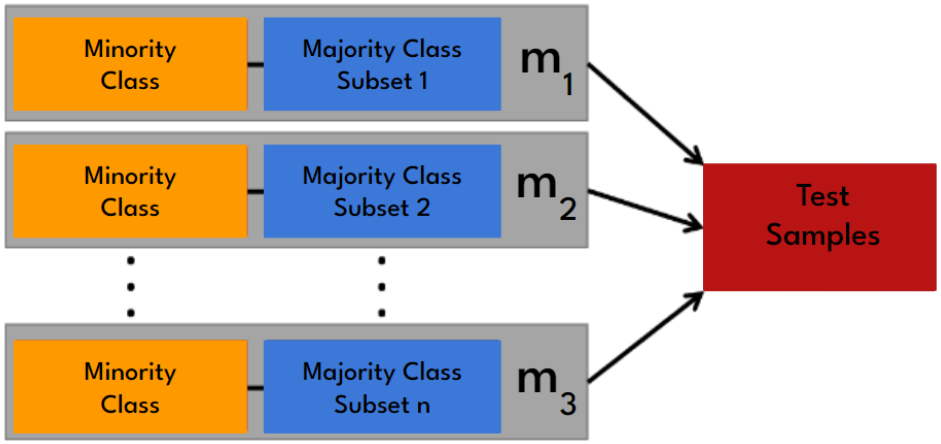

Figure 7.3: The ensemble method visualized. Here, multiple models (m_1-m_n) are each trained on unique combinations of the majority class and the entire minority class. These models then collectively influence the final decision on test samples, employing a majority vote system.

clear physics libraries and an array of physics generators to simulate decay events with high fidelity.

ATTPCROOTv2 equips users with the versatility to create a custom environment that includes detector specifications, and generates event-by-event simulations via a virtual Monte Carlo package. It enables the simulation of particular decay pathways, including $^{20}\mathrm{Mg}(\beta\mathrm{p}\alpha)^{15}\mathrm{O}$ and $^{220}\mathrm{Rn}$ α-decay, as depicted in Figure 7.4. One of the standout features of ATTPCROOTv2 is it produces simulated outputs in a format that mirrors real data from our data acquisition system, facilitating a seamless transition to analysis phases.

Upon the creation of these simulated datasets, pulse shape analysis is performed on the simulated signals from the pad plane. Employing sophisticated pattern recognition algorithms, the system assesses each event and determines the particle paths within the detector's active volume. These Monte Carlo simulations utilize the Geant4 toolkit for physics processes, while data structuring is managed using the HDF5 library. For further insights into the simulation framework and the digitization methodology, the reader is directed to

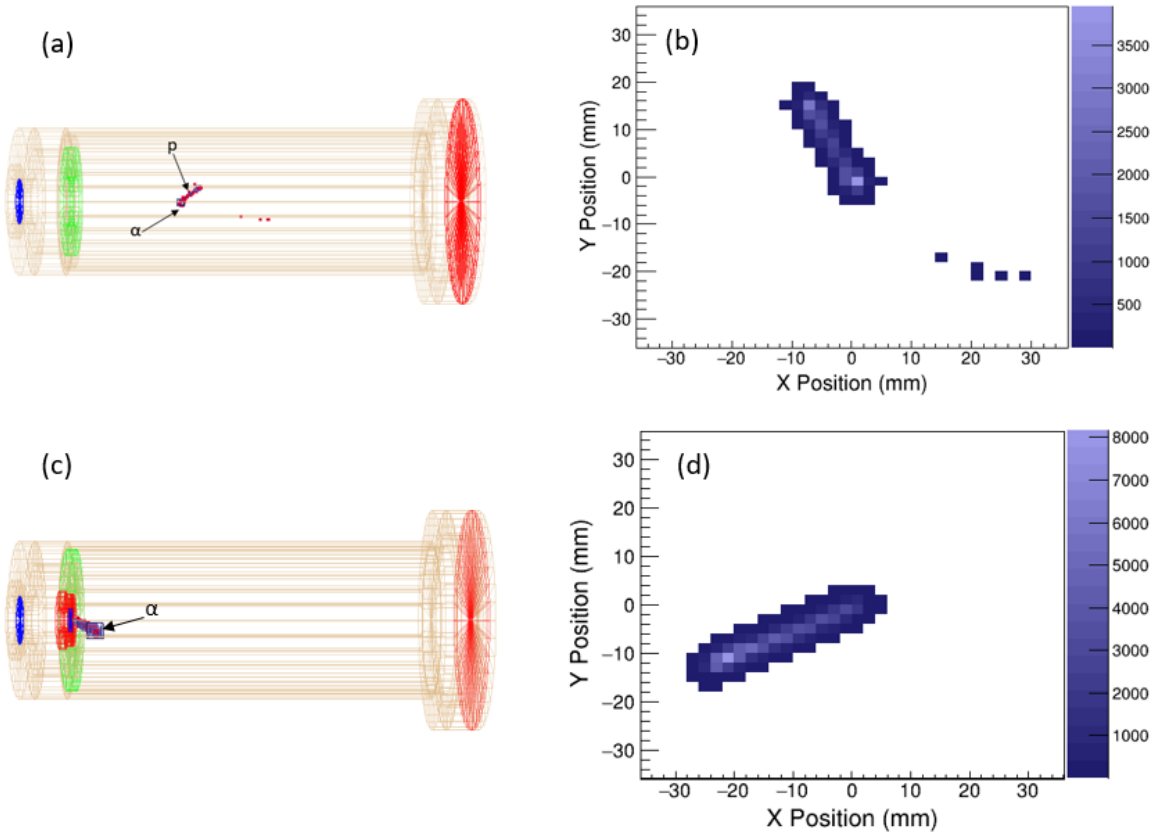

Figure 7.4: Visual representations from ATTPCROOTv2 simulations for the GADGET II TPC: (a) and (b) show the simulation for the ^{20}Mg(βpα)^{15}O decay process, illustrating both the three-dimensional rendering and two-dimensional projection. Panels (c) and (d) exhibit the ^{220}Rn α-decay simulation in analogous representations.

Ref.[75].

7.0.5 Issues with 2D Projections

The rare proton-alpha coincidence events under investigation possess a distinct 3D topology. However, their uniqueness in 2D projections is preserved only when the event trajectory is almost parallel to the projection plane, which is an issue if we want to use 2D CNNs for event classification.

To elaborate, let's consider two classes of events that a CNN could confuse if one used only 2D projections: the proton-alpha coincidence event and a lone proton event. When these events occur parallel to the pad plane, distinguishing a proton-alpha coincidence is feasible due to the significant energy deposition observed at both extremities of the track, as depicted in Figure 7.5a-b. This is characterized by the proton's Bragg peak at one end and the alpha's point-like energy deposition at the other. In contrast, when these events are perpendicular to the pad plane, they resemble nondescript blobs, making differentiation challenging (see Figure 7.5c-d).

This observation highlights that the likelihood of a CNN misidentifying these events increases as their orientation with respect to the pad plane becomes more perpendicular. Nonetheless, a contrasting feature is notable in the time projection of these events, which aggregates the track's charge over time. Here, while parallel-oriented events appear indistinguishable, perpendicular alpha-proton coincidence events reveal a distinct dual-peak profile, as shown in Figure 7.6c. This characteristic underscores the utility of merging these two data representations for improved event classification, a topic we will delve into in the sections that follow.

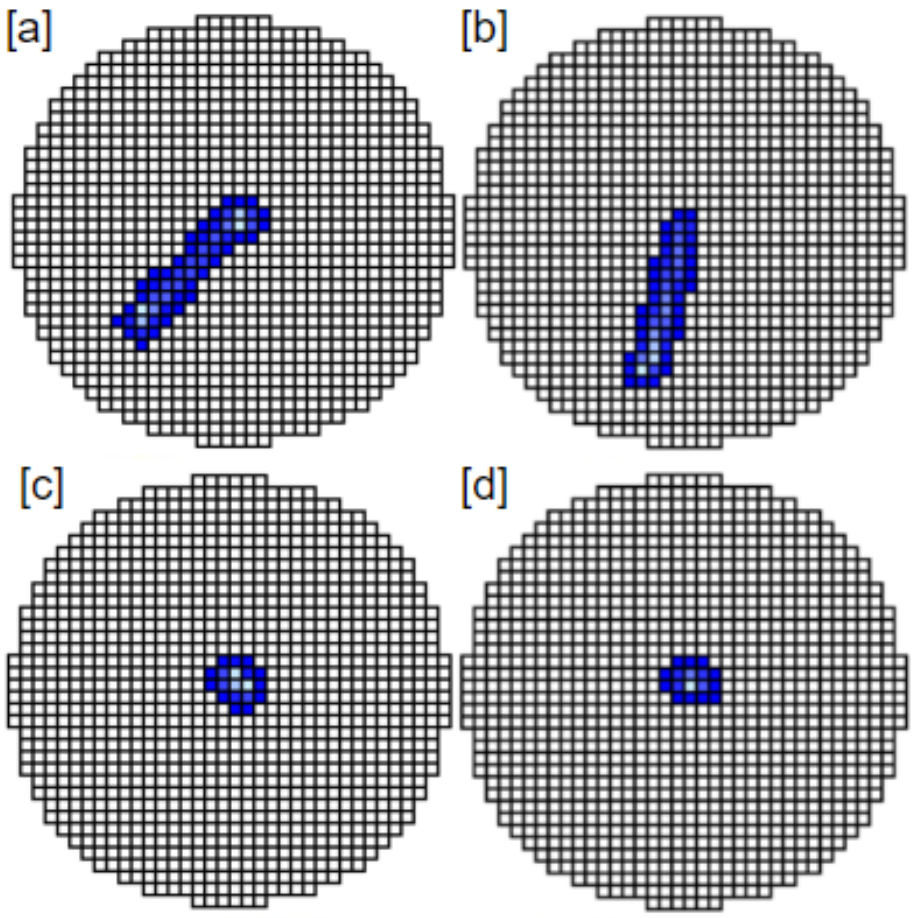

Figure 7.5: Illustrative comparison of 2D event projections on the pad plane: (a) A proton-alpha coincidence event aligned parallel, showing clear energy deposition at both ends. (b) A single proton event parallel to the plane. (c) A proton-alpha coincidence event perpendicular to the plane. (d) A lone proton event also perpendicular.

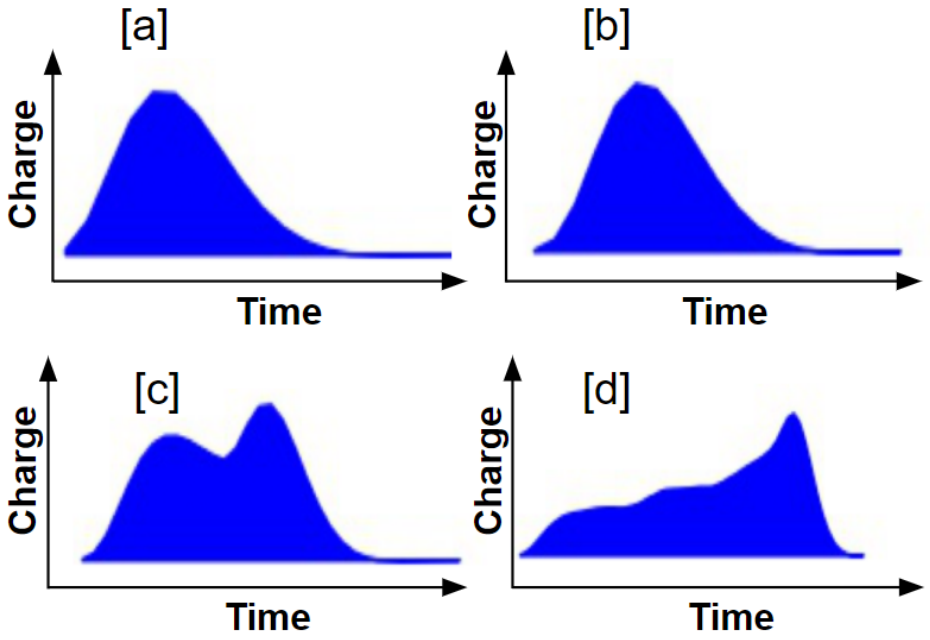

Figure 7.6: Time projection views for the described particle events: (a) The development over time of a parallel proton-alpha coincidence event. (b) Time projection for a lone proton event parallel to the pad plane. (c) The unique double-peak feature of a perpendicular proton-alpha coincidence event. (d) Time projection for a lone proton event occurring perpendicular to the pad plane.

7.0.6 Early Data Fusion

In confronting the issues arising from the reduction of event data to 2D projections, our strategy employs early data fusion, or data-level fusion [76]. In our case, this technique entails appending the feature space of our 2D images with different data modalities. The types of data we integrate are as follows:

- **2D Particle Track Projections:** These provide a spatial visualization of the particle's path, projected onto the pad plane. This projection emphasizes the relative distribution of charge along the particle's trajectory.
- **1D Time Projections:** Also referred to as the trace signal, this dimension aggregates the charge collected over time from all pads for each event, offering insight into the temporal evolution of the particle track within the active volume of the detector.
- **Scalar Energy:** Visually represented through what we refer to as the "energy bar," this metric quantifies the total energy deposited in the event.

This multi-faceted data is synthesized into a unified composite image, herein referred to as a data-fused image (depicted in Figure 7.7). This fusion process ensures that the CNN is furnished with a holistic view, encompassing all critical information that mirrors the unique 3D structure of the events under scrutiny. Such a data representation not only facilitates the precise categorization of these events but also enhances the CNN's learning efficacy by providing a richer dataset for both training and inference phases.

It should be noted that alternative strategies exist for merging these data sources. For instance, one could use a late fusion technique, and deploy a 2D CNN to analyze the 2D track projection and a separate 1D CNN for the time projection histogram data, subsequently

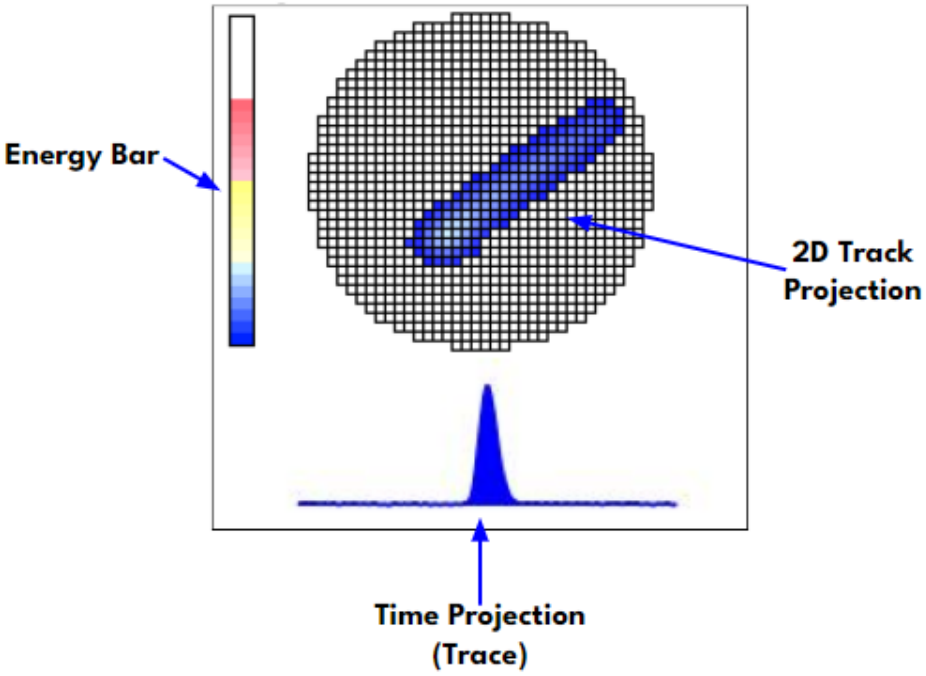

Figure 7.7: Illustration of a data-fused image, incorporating the three principal data modalities: the 2D particle track projection, the 1D time projection (trace signal), and the scalar event energy depicted through the "energy bar".

integrating the outputs using an aggregation function for final predictions. Nevertheless, we discovered that generating a unified, data-fused image—where all pertinent information undergoes convolution and interpretation by a singular CNN—not only yields computational efficiency but also enhances the clarity of events of interest for manual labeling.

7.0.7 Robustification through Parameter Variation

The challenge of aligning network training with simulations to the complex realities of actual data lies in the inherent differences between simulated environments and real-world conditions. These differences can lead to a shift in data distribution, potentially reducing the effectiveness of the model. A strategic approach to mitigate this issue involves the concept of robustification, inspired by strategies developed to counter adversarial perturba-

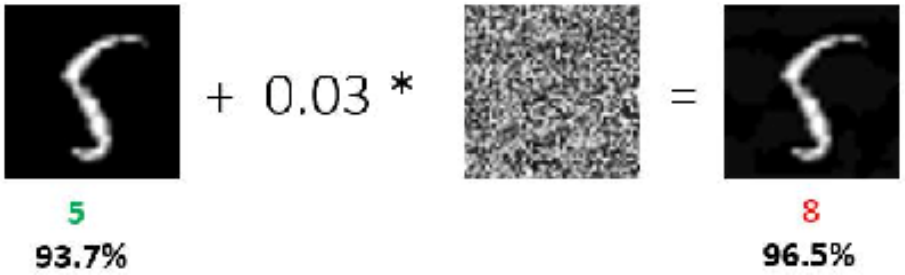

Figure 7.8: An example of adversarial perturbation leading to misclassification. The original image is recognized as a 5, but after perturbation, it is misclassified as an 8.

tions. Such perturbations are minor modifications to input data designed to deceive machine learning models, as depicted in Figure 7.8 with a handwritten digit being misclassified due to intentional noise.

To bolster our network against the discrepancies between simulated and real datasets, we engage in a process similar to adversarial training. This process introduces intentional variations or perturbations into our simulation parameters, thereby preparing the model to withstand real-world data variations. For example, variations in the transverse diffusion coefficient within our simulations could result in inaccuracies in event representation, such as the number of detector pads activated, leading to potential misclassifications.

Our approach to minimizing simulation-real data discrepancies involves a dual-phase strategy. Initially, we calibrate our simulations to more accurately reflect observed real data by adjusting simulation parameters based on actual decay events. This calibration involves a specialized algorithm that dynamically modifies simulation parameters, seeking to minimize the difference between simulated outcomes and real event characteristics.

Upon refining our simulation parameters, we introduce a phase of parameter variation. Here, we establish Gaussian distributions centered around each optimized parameter value (gas gain, gas pressure, transverse and longitudinal diffusion, charge dispersion, etc), allowing for random selection of specific parameters for each simulated event. This approach,

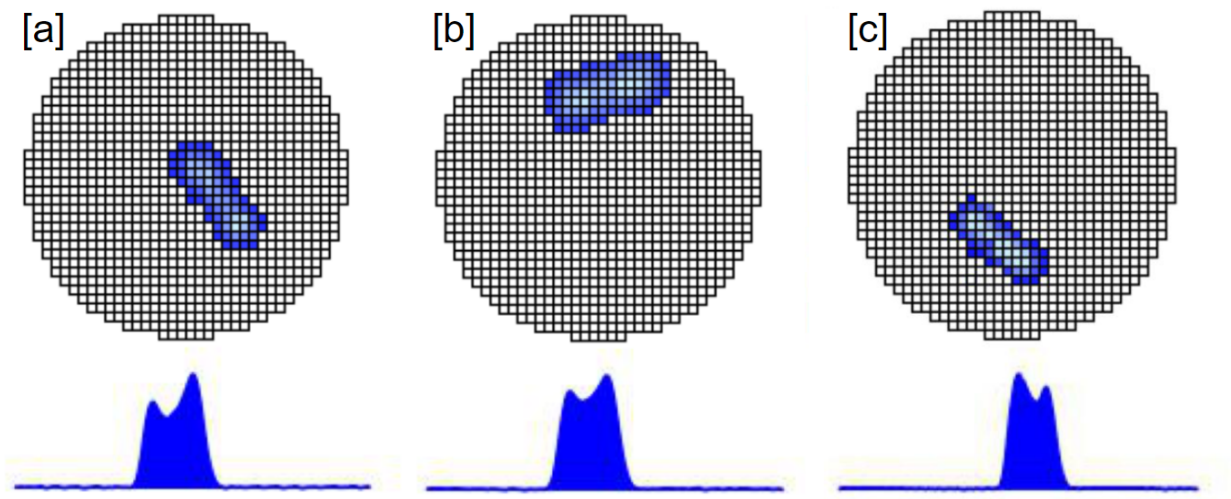

Figure 7.9: Illustration of simulated proton-alpha events with variable physics parameters and their time projections: (a) shows the standard simulation, (b) introduces increased transverse diffusion, and (c) demonstrates adjustments in gain and pad threshold settings.

visualized in Figure 7.9, diversifies the possible event representations in the training dataset, thereby providing the model with a broad spectrum of data scenarios to learn from. Such a varied training set aids the model in identifying more consistent and robust features across a range of real-world events, significantly improving its classification accuracy.

7.0.8 Filter Method

Our CNN ensembles are engineered to serve as highly sensitive filters, designed to identify any events bearing even a slight resemblance to two-particle events. The preparatory step in this process involves the creation of data-fused images derived from our experimental data. A meticulous hand-labeling effort follows, where tens-of-thousands of images are classified. Most of the classes are straightforward, for example, a 1.6 MeV proton event gets labeled as a proton event. However, for the two-particle event class we cast a very wide net. Any event that is either a different two-particle event than the one we are looking for (recall we are specifically interested in ^{20}Mg p-alphas), or even shares any common features with our

events-of-interest is used for training.

For instance, early in our experiment we took a ^{21}Mg beam rather than ^{20}Mg. ^{21}Mg also has a p-alpha branch, but with a significantly (orders of magnitude) higher branching ratio compared to ^{20}Mg, providing a rich source of training data. Additionally, we identified "pseudo-events-of-interest" which, while not actual two-particle events, exhibit key characteristics of interest. Examples include tracks mimicking a double Bragg peak caused by random ionization fluctuations, or the ionization from a recoiling daughter nucleus. The rationale behind integrating pseudo-two-particle events lies in their ability to enhance the dataset, compensating for the rarity of actual two-particle events. This method ensures that our CNNs are exposed to a wide range of pertinent features, some of which might only subtly suggest the presence of the events we seek.

Training our models on this diversified dataset, which also includes parameter varied simulated images (Section 7.0.7), yields CNNs that function as ultra-sensitive filters. Given our emphasis on sensitivity, the CNNs exhibit a high detection rate for our target events, but this comes at the cost of a large number of false positives. This balance between detection rate and false positive rate is deemed acceptable due to the infrequency of the events under investigation.

Employing CNNs as filters in this manner offers significant advantages for our research. The scarcity of the target events necessitates a method that leaves no stone unturned, yet manually reviewing the entire dataset is untenable. By leveraging our CNNs, we drastically streamline the data review process, achieving a substantial reduction in the dataset volume that requires expert analysis. This approach not only ensures that no potential event is overlooked but also enhances the efficiency and manageability of the data review process.

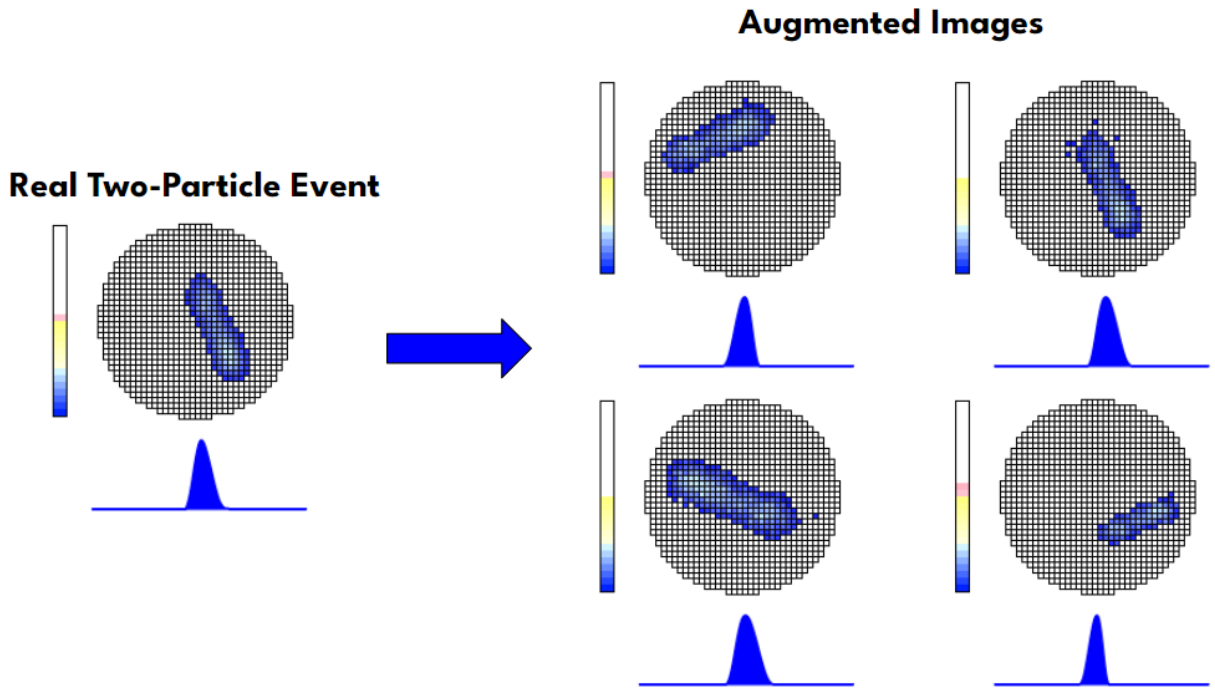

Figure 7.10: Illustration of data augmentation on a real two-particle event from experimental data. This figure showcases the transformation of a singular event into multiple augmented versions, employing techniques such as track rotations, translations, noise addition, random pad activations, scaling, and blurring for spatial adjustments, alongside trace scaling, shifting, mirroring, and energy scaling for temporal/energy modifications. Each augmented image represents a potential variation in training data, enabling the convolutional neural network (CNN) to more robustly learn and identify the key features of two-particle events, thereby enhancing model generalization and precision.

7.0.9 Data Augmentation

As more and more real two-particle events are found in the experimental data via the filtering technique (Section 7.0.8), data augmentation emerges as the best strategic method to substantially enhance our training dataset. Given the scarcity of two-particle events, each instance is exceedingly precious. Yet, the specialized nature of our data imposes limitations on the applicability of standard augmentation techniques, such as cropping or random rotations applied to whole images.

To adapt to our unique dataset, we concentrate on manipulating the 2D projections of particle tracks on the pad plane. By selectively applying our augmentation features

(track rotations, translations, track and edge noise, random pad fires, track scaling, and track blurring) to this aspect of the data, we enable the CNN to recognize and learn the fundamental characteristics of real two-particle events.

Beyond spatial modifications, we also apply augmentation features to the time projection component of our data through the addition of trace scaling, trace shifting, and trace mirroring. Additionally, we also apply energy scaling as an augmentation feature. Figure 7.10 shows an example of a real two-particle event and how we can create an arbitrary number of augmented images from it by applying our augmentation features.

Employing this strategy, we can transform a solitary two-particle event into a plethora of varied training examples. This approach not only enriches the model's exposure to the minority class but also significantly broadens its capability to generalize from even a single occurrence of an event-of-interest. Given this, we can train new models that are far more precise than the initial filtering ensembles. These new models still have a high detection rate for our target events, along with a reduction in the number of false positives.

7.0.10 Performance Metrics

As is common when evaluating CNN performance, we will use the metrics **precision**, **recall**, and **F1 score** [77, 19]. To lay the groundwork for understanding these evaluation metrics we will look to the confusion matrix. When dealing with a binary classification problem, confusion matrices work by categorizing model predictions into four distinct outcomes: true positives (TP), false positives (FP), true negatives (TN), and false negatives (FN) (see Figure 7.11).

Precision measures the model's accuracy in predicting two-particle events. Specifically, it answers the question: "Of all the events predicted to be two-particle events, how many

were actually two-particle events?" A higher precision score indicates a model that is more accurate in its positive predictions, minimizing the risk of false positives. The metric is defined as the ratio of true positives to the sum of true positives and false positives:

$$\text{Precision} = \frac{TP}{TP + FP} \tag{7.1}$$

Recall evaluates the model's ability to identify all actual two-particle events. It addresses the question: "Of all the actual two-particle events, how many did the model successfully identify?" This metric is essential in scenarios where missing an actual two-particle event (a false negative) could lead to significant oversight or loss of crucial information. Thus, a high recall score signifies that the model is proficient at detecting two-particle events, ensuring minimal loss of vital events-of-interest. As such, it is this metric that we are most concerned with, and it is calculated as the ratio of true positives to the sum of true positives and false negatives:

$$\text{Recall} = \frac{TP}{TP + FN} \tag{7.2}$$

F1 score harmonizes the balance between precision and recall, offering a single metric that encapsulates both the model's accuracy and its completeness in identifying two-particle events. It is particularly useful when you need to compare models that might have a trade-off between precision and recall, allowing for a balanced assessment of model performance. The harmonic mean is used because it is more sensitive to low values, ensuring that models can only achieve a high F1 score by performing well in both precision and recall. A high F1 score indicates a model that is both accurate and comprehensive in its identification of two-particle events, striking a desirable balance where both false positives and false negatives

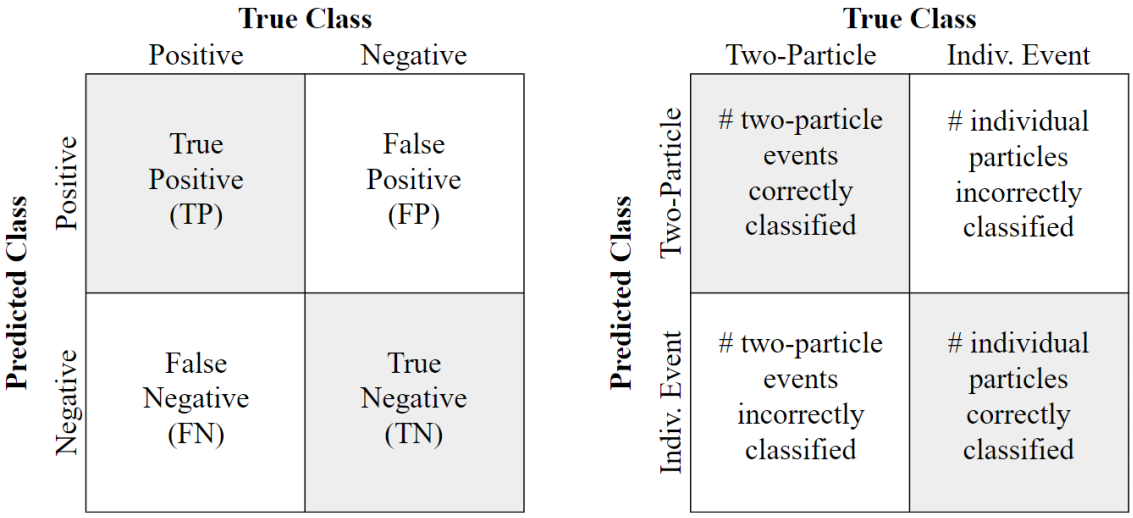

Figure 7.11: Depiction of a confusion matrix in binary classification. Rows illustrate predictions made by the classifier, and columns indicate actual class labels. The left matrix defines the terminology for each component of the matrix, while the right matrix demonstrates how these terms are utilized in the context of the GADGET II TPC rare event search. In an ideal scenario, the classifier would produce a confusion matrix with all values concentrated along the diagonal, showcasing perfect predictive accuracy (adapted from [19]).

are minimized.:

$$\mathrm{F1} = 2 \times \frac{\mathrm{Precision} \times \mathrm{Recall}}{\mathrm{Precision} + \mathrm{Recall}} \tag{7.3}$$

Employing precision, recall, and the F1 score provides a nuanced understanding of model performance in the GADGET II TPC data. These metrics, ranging from 0 to 1, allow for a detailed evaluation of models' abilities to correctly identify two-particle events.

7.0.11 Results

The filter method (Section 7.0.8) necessitated the training of a large number of models. The 5 best performing models were selected to operate as an ensemble (Section 7.0.3). In this case, the performance metric we were most concerned about was recall (Section 7.0.10), as we wanted to ensure that few events of interest were missed, even at the cost of false positives.

The selected models shared common training characteristics: they leveraged the pre-

Figure 7.12: Depiction of the learning curve for Model A, illustrating the evolution of the model's loss on the training set (in blue) and the validation set (in red) across epochs.

Model	Precision	Recall	F1
Model A	0.85	0.96	0.90
Model B	0.73	0.96	0.83
Model C	0.74	0.97	0.84
Model D	0.82	0.95	0.88
Model E	0.71	0.97	0.82
Ensemble	0.75	0.98	0.85

Table 7.1: Performance metrics for models A-E, and the corresponding ensemble. Models in the ensemble were chosen to favor recall for the two-particle class. The models were trained on a combination of parameter varied simulated data, and experimental data using the filter method (Section 7.0.8).

trained VGG16 architecture which was fine-tuned with a custom classifier (Section 2.1.2). The training employed cross-entropy loss and utilized an SGD optimizer with a momentum setting of 0.9. To adjust the learning rate, we applied a ReduceLROnPlateau scheduler, initialized with a learning rate of 0.001 and a patience interval of four epochs (Section 2.2.3). To counteract data imbalance, we implemented sampling strategies to ensure a balanced training dataset (Section 7.0.1), with a batch size set to four. Additionally, the training protocol augmented the class weight for the minority class, which pertains to the two-particle

events-of-interest, amplifying the loss impact from errors in this category by a factor of ten (Section 7.0.1). The training duration spanned 100 epochs, and Figure 7.12 shows an example of a learning curve (loss vs epochs) plot for Model A. Performance metrics for individual models and the ensemble are presented in Table 7.1, showcasing that the ensemble is able to successfully identify >98% of two-particle events within the dataset.

Refined Model	Precision	Recall	F1
Model F	0.78	0.98	0.87
Model G	0.79	0.98	0.87
Model H	0.87	0.98	0.92

Table 7.2: Performance metrics for refined models F-H. The models were trained on additional augmented images of real events found during the ensemble filter process. Note that each model performs better than the ensemble from Table 7.1, and the models are get progressively better as additional augmented images are added.

This ensemble was applied to well-defined search regions on runs of experimental data (Section 6.3.1). These search regions typically have tens-of-thousands of events in them, thus our week long experimental campaign would require the manual examination of millions of images. After applying the ensemble filter the dataset is reduced by over an order of magnitude, making the total amount of data requiring human review closer to hundreds of thousands of images. While still sizable, this is a massive reduction in the person-power required for event classification.

As the ensemble filter is applied and new two-particle-events are found, we then use the data augmentation software (Section 7.0.9) to turn those events into a much larger training pool. Then new, more precise models are trained that still have a high recall, but also improved precision leading to a reduced number of false positives. Table 7.2 highlights the performance of three such refined models, each outperforming the initial ensemble. Notably, the models improve sequentially, with each subsequent model benefiting from an increased

number of augmented images found with the ensemble filter. As of writing this thesis, the process of training refined models from events found via the ensemble filter is still on going. Once enough refined models are trained, a more precise ensemble will be deployed on the remaining data to find all outstanding two-particle events.

Chapter 8

Summary and Outlook

The $^{15}O(\alpha, \gamma)^{19}Ne$ reaction rate is a critical uncertainty in the modeling of X-ray bursts emanating from neutron stars. The essence of determining this reaction rate lies in the precise measurement of the small alpha-particle branching ratio from the 4.03 MeV state in ^{19}Ne. This state is populated in the decay of ^{20}Mg, with $^{20}Mg(\beta p\alpha)$ events offering a unique $p-\alpha$ signature that can be used to measure the key alpha branching ratio.

To capture these elusive events the GADGET II TPC was built, and tested. The tests were performed using ^{220}Rn and ^{216}Po and revealed the TPC's proficiency in detecting and identifying charged particles, alongside measuring their trajectory, range, and energy with notable precision. Utilizing P10 gas, the GADGET II TPC showed an energy resolution of $\sim$5.4% at 6.288 MeV, achieved through detailed charge integration methods. The sensitivity of the TPC was also established from its ability to detect low-ionizing cosmic-ray muons. This also allowed for the determination of the drift velocity under normal operating conditions. Notably, the GADGET II TPC is among the first micro pattern gaseous detectors to utilize a resistive anode in the realm of low-energy nuclear physics. Additionally, its the first TPC to be surrounded by an array of HPGe detectors for the measurement of gamma-rays [15].

Extensive development work was done to couple this new TPC to DEGAi, the HPGe array, which is part of FRIB Decay Station initiator. This coupled system forms the full GADGET II experimental setup employed in E21072. Experiment E21072, conducted at the FRIB, utilized the newly upgraded GADGET II detection system. Early in the experiment

we received a beam of ^{21}Mg, which we used to commission the detector, and successfully measured $p-\alpha$ events that closely mirror our primary events-of-interest. Subsequent to that, we received an isotopically pure beam of ^{20}Mg, albeit at a substantially lower intensity than initially anticipated. Owing to this, our projections have been cautiously adjusted to anticipate the identification of no more than 4 events-of-interest under the most optimistic scenarios, and 0.4 based on the lowest estimate of the branching ratio. The astrophysical problem in question can be satisfactorily resolved by achieving a branching ratio uncertainty of 50%. This corresponds to the identification of approximately four events-of-interest. Therefore, there is a strong possibility that a subsequent experimental campaign will be needed to collect a sufficient amount of statistics to determine the branching ratio with an acceptable level of uncertainty.

In our pursuit to find these events-of-interest in the data, a search region was applied to range vs energy histograms, on which the $p-\alpha$ events will occupy a specific region, facilitating a targeted analysis. The sophistication of this search is significantly enhanced through the integration of machine learning algorithms, particularly CNNs. Our methodology utilizes early data fusion techniques to leverage the different TPC data modalities, transforming 3D TPC tracks into 2D representations that retain essential 3D topological information. This approach takes advantage of the computational efficiency of 2D CNNs, and takes advantage of a wealth of pre-trained models.

In light of the challenges presented by the scarcity of the events under investigation and the potential inaccuracies stemming from the significant use of simulated data, our approach adopts a comprehensive strategy. We enhance our training dataset through the adoption of active learning and iterative reinforcement techniques, and fully leverage each authentic two-particle event in our dataset through the implementation of custom data augmentation

methods. Additionally, to ensure the effective incorporation of simulations into our training dataset, we integrate perturbations that reflect physics parameter and detector response uncertainties. This significantly improves the model's ability to bridge the gap between simulated and real data. Concurrently, we refine our training protocols to cultivate CNNs that operate as extremely sensitive filters for our specified events-of-interest, and deploy them as ensembles to reduce individual model bias. The resulting ensembles applied to the experimental data are able to identify >98% of all two-particle events in the dataset [26]. Approximately half of the experimental dataset has been meticulously searched for rare events-of-interest, with models undergoing refinement based on two-particle events detected by the ensemble filter. This process is enhancing both the accuracy and precision of the models, consequently accelerating the search for rare events.

Looking forward, we will continue to diligently analyze the dataset in search of events-of-interest. Upon identification, such events will undergo a thorough validation process to confirm their derivation from the anticipated state in ^{19}Ne, with a special focus on the detailed examination of the $p-\alpha$ energy distribution. This scrutiny is essential for accurately distinguishing between various decay mechanisms. In the event that $^{20}\mathrm{Mg}(\beta p\alpha)$ occurrences are detected within our data, thus allowing for a finite measurement of the ^{19}Ne alpha branching ratio, our next steps will involve calculating the $^{15}\mathrm{O}(\alpha,\gamma)^{19}\mathrm{Ne}$ reaction rate. Achieving this milestone will not only advance our comprehension of the fundamental nuclear reactions involved but also facilitate the precise modeling of Type I X-ray burst light curves from neutron stars.

Additionally, we have a PAC 2 approved FRIB experiment to measure the next two critical reactions in Type I X-ray bursts. This experiment will also utilize the GADGET II system, and will investigate $^{56}\mathrm{Ni}(\alpha,p)^{59}\mathrm{Cu}$ and $^{59}\mathrm{Cu}(p,\gamma)^{60}\mathrm{Zn}$ using the beta decay

of ^{60}Ga. The primary objective of this study is to identify and characterize resonances, alongside quantifying branching ratios for proton, alpha, and gamma emissions.

BIBLIOGRAPHY

BIBLIOGRAPHY

[1] Alejandro Sonzogni. Nndc chart of nuclides. In *International Conference on Nuclear Data for Science and Technology*, pages 105–106. EDP Sciences, 2007.

[2] S. J. Ling, J. Sanny, and W. Moebs. *University Physics*. OpenStax, Rice University, 2018.

[3] K.K. S. *Introductory Nuclear Physics*. Wiley India, 2008.

[4] Z. Abdallah. Investigating temporal convolutional neural networks for satellite image time series classification. *Multidisciplinary Digital Publishing Institute*, 2022.

[5] FirelordPhoenix. Pictorial example of max-pooling. `https://computersciencewiki.org/index.php/File:MaxpoolSample2.png`, Feb 2018. Online; accessed 26-Feb-2018.

[6] LANIT JSC. What is the cnn algorithm? learn cnn algorithm from a – z. `https://lanit.com.vn/thuat-toan-cnn.html`, Oct 2023. Accessed: date-of-access.

[7] Khuyen Le. An overview of vgg16 and nin models. *MLearning.ai*, Mar 2021. Accessed: date-of-access.

[8] Ivica Miskovicova. Feeding the monster: Wind accretion in black hole binaries, URL: `https://www.black-hole.eu/index.php/general-public/p7-feeding-the-monster-wind-accretion-in-black-hole-binaries.html`, 2021, cited 2024-02-27. Accessed: 2024-02-27.

[9] Christian Iliadis. *The Nuclear Physics of Stars*. Weinheim, 2007.

[10] B. E. Glassman. *^{20}Mg β-decay and the $^{15}O(\alpha, \gamma)^{19}Ne$ Reaction Sequence in Type I X-ray Bursts*. PhD thesis, Michigan State University, Lansing MI, USA, 2019.

[11] R.H. Cyburt. Dependence of x-ray burst models on nuclear reaction rates. *The Astrophysical Journal*, 830(2):55, 2016.

[12] C. Wrede and B. Glassman. New portal to the ^{15}o(α, γ)^{19}ne resonance triggering cno-cycle breakout. *Physical Review C*, 96(3), 2017.

[13] Matthaeus Leitner, B Bird, F Casagrande, S Chouhan, C Compton, J Crisp, K Elliot, A Facco, A Fox, M Hodek, et al. The frib project at msu. In *Proc. of the 16th Workshop on RF Superconductivity*, page 1, 2013.

[14] M. Hausmann, A.M. Aaron, A.M. Amthor, M. Avilov, L. Bandura, R. Bennett, G. Bollen, T. Borden, T.W. Burgess, S.S. Chouhan, V.B. Graves, W. Mittig, D.J. Morrissey, F. Pellemoine, M. Portillo, R.M. Ronningen, M. Schein, B.M. Sherrill, and A. Zeller. Design of the advanced rare isotope separator aris at frib. *Nuclear Instruments and Methods in Physics Research Section B: Beam Interactions with Materials and Atoms*, 317:349–353, 2013. XVIth International Conference on ElectroMagnetic Isotope Separators and Techniques Related to their Applications, December 2–7, 2012 at Matsue, Japan.

[15] R. Mahajan, T. Wheeler, E. Pollacco, C. Wrede, A. Adams, H. Alvarez-Pol, A. Andalib, A. Anthony, Y. Ayyad, D. Bazin, T. Budner, M. Cortesi, J. Dopfer, M. Friedman, A. Jaros, D. Perez-Loureiro, B. Mehl, R. De Oliveira, L. J. Sun, , and J. Surbrook. Time projection chamber for gadget ii. 2024. Submitted to PRC.

[16] Triangle Universities Nuclear Laboratory. 20mg β^+-decay evaluated data, URL: `https://nucldata.tunl.duke.edu/nucldata/GroundStatedecays/20Mg.shtml`, 2023. Accessed: 2024-02-26.

[17] B. E. Glassman, D. Pérez-Loureiro, C. Wrede, J. Allen, D. W. Bardayan, M. B. Bennett, K. A. Chipps, M. Febbraro, M. Friedman, C. Fry, M. R. Hall, O. Hall, S. N. Liddick, P. O'Malley, W.-J. Ong, S. D. Pain, S. B. Schwartz, P. Shidling, H. Sims, L. J. Sun, P. Thompson, and H. Zhang. Doppler broadening in ^{20}Mg$(\beta p\gamma)^{19}$Ne decay. *Phys. Rev. C*, 99:065801, Jun 2019.

[18] Rens. Active learning explained. `https://asreview.nl/blog/active-learning-explained/`, April 2022. Accessed: [insert access date here].

[19] M.P. Kuchera, R. Ramanujan, J.Z. Taylor, R.R. Strauss, D. Bazin, J. Bradt, and Ruiming Chen. Machine learning methods for track classification in the at-tpc. *Nuclear Instruments and Methods in Physics Research Section A: Accelerators, Spectrometers, Detectors and Associated Equipment*, 940:156–167, 2019.

[20] Klaus Hentschel. *Atomic Models, J.J. Thomson's "Plum Pudding" Model*, pages 18–21. Springer Berlin Heidelberg, Berlin, Heidelberg, 2009.

[21] Ernest Rutherford. The scattering of α and β particles by matter and the structure of the atom. *Philosophical Magazine*, 92(4):379–398, 2012.

[22] James Chadwick. Possible existence of a neutron. *Nature*, 129(3252):312–312, 1932.

[23] SM Kane, IS Padda, and DD Davis. Technetium-99m, URL: `https://www.ncbi.nlm.nih.gov/books/NBK559013/`, Jan 2023, cited 2023-04-24. Updated 2023 Apr 24.

[24] N Bloembergen. National academy of sciences: Abstracts of papers presented at the annual meeting, 24-26 april 1961, washington, dc. *Science*, 133(3461):1363–1370, 1961.

[25] Karen Simonyan and Andrew Zisserman. Very deep convolutional networks for large-scale image recognition, 2015.

[26] Tyler Wheeler, R. Mahajan, S. Ravishankar, C. Wrede, A. Andalib, A. Anthony, Y. Ayyad, B. Jain, A. Jaros, and L. Schaedig. Rare event search in gadget ii tpc data using 2d convolutional neural networks with early data fusion. Manuscript in preparation, 2023.

[27] Kaiming He, Xiangyu Zhang, Shaoqing Ren, and Jian Sun. Delving deep into rectifiers: Surpassing human-level performance on imagenet classification, 2015.

[28] Alex Krizhevsky, Ilya Sutskever, and Geoffrey E Hinton. Imagenet classification with deep convolutional neural networks. In F. Pereira, C.J. Burges, L. Bottou, and K.Q. Weinberger, editors, *Advances in Neural Information Processing Systems*, volume 25. Curran Associates, Inc., 2012.

[29] Jason Yosinski, Jeff Clune, Yoshua Bengio, and Hod Lipson. How transferable are features in deep neural networks?, 2014.

[30] David E Rumelhart, Geoffrey E Hinton, and Ronald J Williams. Learning representations by back-propagating errors. *nature*, 323(6088):533–536, 1986.

[31] Jack Kiefer and Jacob Wolfowitz. Stochastic estimation of the maximum of a regression function. *The Annals of Mathematical Statistics*, pages 462–466, 1952.

[32] Everton Gomede. Sparse neural networks and pruning: Trimming the fat for efficient machine learning. *Medium*, Oct 2023.

[33] Arthur E Hoerl and Robert W Kennard. Ridge regression: Biased estimation for nonorthogonal problems. *Technometrics*, 12(1):55–67, 1970.

[34] W. Lewin. X-ray bursts. *Space Science Reviews*, 62, 1993.

[35] R. K. Wallace and S. E. Woosley. Explosive hydrogen burning. *Astrophysical Journal Supplement Series*, 45:389–420, February 1981.

[36] Y. Herrera, G. Sala, and J. José. Mass-loss and composition of wind ejecta in type i x-ray bursts. *Astronomy amp; Astrophysics*, 678:A156, October 2023.

[37] E. Margaret Burbidge, G. R. Burbidge, William A. Fowler, and F. Hoyle. Synthesis of the elements in stars. *Rev. Mod. Phys.*, 29(4):547, 1957.

[38] Jacob Lund Fisker, Joachim Görres, Michael Wiescher, and Barry Davids. The importance of 15o(α,γ)19ne to x-ray bursts and superbursts. *The Astrophysical Journal*, 650(1):332, oct 2006.

[39] D.R. Tilley, H.R. Weller, C.M. Cheves, and R.M. Chasteler. Energy levels of light nuclei a = 18–19. *Nuclear Physics A*, 595(1):1–170, 1995.

[40] R. Kanungo, T. K. Alexander, A. N. Andreyev, G. C. Ball, R. S. Chakrawarthy, M. Chicoine, R. Churchman, B. Davids, J. S. Forster, S. Gujrathi, G. Hackman, D. Howell, J. R. Leslie, A. C. Morton, S. Mythili, C. J. Pearson, J. J. Ressler, C. Ruiz, H. Savajols, M. A. Schumaker, I. Tanihata, P. Walden, and S. Yen. Lifetime of ^{19}ne*(4.03 mev). *Phys. Rev. C*, 74:045803, Oct 2006.

[41] W. P. Tan, J. Görres, J. Daly, M. Couder, A. Couture, H. Y. Lee, E. Stech, E. Strandberg, C. Ugalde, and M. Wiescher. Lifetime of the astrophysically important 4.03-mev state in ^{19}Ne. *Phys. Rev. C*, 72:041302, Oct 2005.

[42] S. Mythili, B. Davids, T. K. Alexander, G. C. Ball, M. Chicoine, R. S. Chakrawarthy, R. Churchman, J. S. Forster, S. Gujrathi, G. Hackman, D. Howell, R. Kanungo, J. R. Leslie, E. Padilla, C. J. Pearson, C. Ruiz, G. Ruprecht, M. A. Schumaker, I. Tanihata, C. Vockenhuber, P. Walden, and S. Yen. Lifetimes of states in ^{19}Ne above the ^{15}O+α breakup threshold. *Phys. Rev. C*, 77:035803, Mar 2008.

[43] B. Davids, A. M. van den Berg, P. Dendooven, F. Fleurot, M. Hunyadi, M. A. de Huu, R. H. Siemssen, H. W. Wilschut, H. J. Wörtche, M. Hernanz, J. José, K. E. Rehm, A. H. Wuosmaa, and R. E. Segel. Astrophysical rate of $^{15}\mathrm{O}(\alpha,\gamma)^{19}\mathrm{Ne}$ via the (p,t) reaction in inverse kinematics. *Phys. Rev. C*, 67:065808, Jun 2003.

[44] K. E. Rehm, A. H. Wuosmaa, C. L. Jiang, J. A. Caggiano, J. P. Greene, A. Heinz, D. Henderson, R. V. F. Janssens, E. F. Moore, G. Mukherjee, R. C. Pardo, T. Pennington, J. P. Schiffer, R. H. Siemssen, M. Paul, L. Jisonna, and R. E. Segel. Branching ratio of the 4.033 mev 3/2+ state in 19ne. *Phys. Rev. C*, 67(6):065809, Jun 2003.

[45] W. P. Tan, J. L. Fisker, J. Görres, M. Couder, and M. Wiescher. $O15(\alpha,\gamma)ne19breakoutreactionandimpactonx - rayburst s.$ *Phys.Rev.Lett.*, 98(24) : 242503, $Jun2007$.

[46] Barry Davids, Richard H. Cyburt, Jordi José, and Subramanian Mythili. The influence of uncertainties in the15o(α, γ)19ne reaction rate on models of type i x-ray bursts. *The Astrophysical Journal*, 735(1):40, June 2011.

[47] P.V. Magnus, M.S. Smith, A.J. Howard, P.D. Parker, and A.E. Champagne. Measurement of 15o(α,γ)19ne resonance strengths. *Nuclear Physics A*, 506(2):332–345, 1990.

[48] A. M. Laird, S. Cherubini, A. N. Ostrowski, M. Aliotta, T. Davinson, A. Di Pietro, P. Figuera, W. Galster, J. S. Graulich, D. Groombridge, J. Hinnefeld, M. Lattuada, P. Leleux, L. Michel, A. Musumarra, A. Ninane, M. G. Pellegriti, A. C. Shotter, Spitaleri, A. Tumino, J. Vervier, and P. Woods. Indirect study of the astrophysically important $^{15}O(\alpha,\gamma)^{19}Ne$ reaction through $^{2}H(^{18}Ne,^{19}Ne)^{1}H$. *Phys. Rev. C*, 66:048801, Oct 2002.

[49] D. W. Visser, J. A. Caggiano, R. Lewis, W. B. Handler, A. Parikh, and P. D. Parker. Particle decay branching ratios for states of astrophysical importance in ^{19}Ne. *Phys. Rev. C*, 69:048801, Apr 2004.

[50] E. Pollacco, L. Trache, E. Simmons, A. Spiridon, M. McCleskey, B.T. Roeder, A. Saastamoinen, R.E. Tribble, G. Pascovici, M. Kebbiri, J.P. Mols, and M. Raillot. Astrobox: A novel detection system for very low-energy protons from β-delayed proton decay. *Nuclear Instruments and Methods in Physics Research Section A: Accelerators, Spectrometers, Detectors and Associated Equipment*, 723:102–108, 2013.

[51] D. Attié, M. Batkiewicz-Kwasniak, P. Billoir, A. Blanchet, A. Blondel, S. Bolognesi, D. Calvet, M.G. Catanesi, M. Cicerchia, G. Cogo, P. Colas, G. Collazuol, A. Delbart, J. Dumarchez, S. Emery-Schrenk, M. Feltre, C. Giganti, F. Gramegna, M. Grassi, M. Guigue, P. Hamacher-Baumann, S. Hassani, F. Iacob, C. Jesús-Valls, R. Kurjata, M. Lamoureux, M. Lehuraux, A. Longhin, T. Lux, L. Magaletti, T. Marchi, A. Maurel, L. Mellet, M. Mezzetto, L. Munteanu, Q.V. Nguyen, Y. Orain, M. Pari, J.-M. Parraud, C. Pastore, A. Pepato, E. Pierre, B. Popov, H. Przybiliski, T. Radermacher, E. Radicioni, M. Riallot, S. Roth, A. Rychter, L. Scomparin, J. Steinmann, S. Suvorov, J. Swierblewski, D. Terront, N. Thamm, F. Toussenel, V. Valentino, G. Vasseur, U. Yevarouskaya, M. Ziembicki, and M. Zito. Characterization of resistive micromegas detectors for the upgrade of the t2k near detector time projection chambers. *Nuclear Instruments and Methods in Physics Research Section A: Accelerators, Spectrometers, Detectors and Associated Equipment*, 1025:166109, 2022.

[52] M. Chefdeville, R. de Oliveira, C. Drancourt, N. Geffroy, T. Geralis, P. Gkountoumis, A. Kalamaris, Y. Karyotakis, D. Nikas, F. Peltier, O. Pizzirusso, A. Psallidas, A. Teixeira, M. Titov, and G. Vouters. Development of micromegas detectors with resistive anode

pads. *Nuclear Instruments and Methods in Physics Research Section A: Accelerators, Spectrometers, Detectors and Associated Equipment*, 1003:165268, 2021.

[53] M.s. Dixit. Position sensing from charge dispersion in micro-pattern gas detectors with a resistive anode. *Nuclear Instruments and Methods in Physics Research Section A: Accelerators, Spectrometers, Detectors and Associated Equipment*, 518(3):721:727, 2004.

[54] M.s. Dixit. Simulating the charge dispersion phenomena in micro pattern gas detectors with a resistive anode. *Nuclear Instruments and Methods in Physics Research Section A: Accelerators, Spectrometers, Detectors and Associated Equipment*, 566(2):281:285, 2006.

[55] E.C. Pollacco, G.F. Grinyer, F. Abu-Nimeh, T. Ahn, S. Anvar, A. Arokiaraj, Y. Ayyad, H. Baba, M. Babo, P. Baron, D. Bazin, S. Beceiro-Novo, C. Belkhiria, M. Blaizot, B. Blank, J. Bradt, G. Cardella, L. Carpenter, S. Ceruti, E. De Filippo, E. Delagnes, S. De Luca, H. De Witte, F. Druillole, B. Duclos, F. Favela, A. Fritsch, J. Giovinazzo, C. Gueye, T. Isobe, P. Hellmuth, C. Huss, B. Lachacinski, A.T. Laffoley, G. Lebertre, L. Legeard, W.G. Lynch, T. Marchi, L. Martina, C. Maugeais, W. Mittig, L. Nalpas, E.V. Pagano, J. Pancin, O. Poleshchuk, J.L. Pedroza, J. Pibernat, S. Primault, R. Raabe, B. Raine, A. Rebii, M. Renaud, T. Roger, P. Roussel-Chomaz, P. Russotto, G. Saccà, F. Saillant, P. Sizun, D. Suzuki, J.A. Swartz, A. Tizon, A. Trifiró, N. Usher, G. Wittwer, and J.C. Yang. Get: A generic electronics system for tpcs and nuclear physics instrumentation. *Nuclear Instruments and Methods in Physics Research Section A: Accelerators, Spectrometers, Detectors and Associated Equipment*, 887:81–93, 2018.

[56] S.-C. Wu. Nuclear data sheets for a = 216. *Nuclear Data Sheets*, 108(5):1057–1092, 2007.

[57] K. Auranen and E.A. McCutchan. Nuclear data sheets for a=212. *Nuclear Data Sheets*, 168:117–267, 2020.

[58] Irad Ben-Gal. *Outlier Detection*, pages 131–146. Springer US, Boston, MA, 2005.

[59] Svante Wold, Kim Esbensen, and Paul Geladi. Principal component analysis. *Chemometrics and Intelligent Laboratory Systems*, 2(1):37–52, 1987. Proceedings of the Multivariate Statistical Workshop for Geologists and Geochemists.

[60] J. Giovinazzo, J. Pibernat, T. Goigoux, R. de Oliveira, G.F. Grinyer, C. Huss, B. Mauss, J. Pancin, J.L. Pedroza, A. Rebii, T. Roger, P. Rosier, F. Saillant, and G. Wittwer. Metal-core pad-plane development for actar tpc. *Nuclear Instruments and Methods in Physics Research Section A: Accelerators, Spectrometers, Detectors and Associated Equipment*, 892:114–121, 2018.

[61] J. Giovinazzo, J. Pancin, J. Pibernat, and T. Roger. Actar tpc performance with get electronics. *Nuclear Instruments and Methods in Physics Research Section A: Accelerators, Spectrometers, Detectors and Associated Equipment*, 953:163184, 2020.

[62] M. Heffner, D.M. Asner, R.G. Baker, J. Baker, S. Barrett, C. Brune, J. Bundgaard, E. Burgett, D. Carter, M. Cunningham, J. Deaven, D.L. Duke, U. Greife, S. Grimes, U. Hager, N. Hertel, T. Hill, D. Isenhower, K. Jewell, J. King, J.L. Klay, V. Kleinrath, N. Kornilov, R. Kudo, A.B. Laptev, M. Leonard, W. Loveland, T.N. Massey, C. McGrath, R. Meharchand, L. Montoya, N. Pickle, H. Qu, V. Riot, J. Ruz, S. Sangiorgio, B. Seilhan, S. Sharma, L. Snyder, S. Stave, G. Tatishvili, R.T. Thornton, F. Tovesson, D. Towell, R.S. Towell, S. Watson, B. Wendt, L. Wood, and L. Yao. A time projection chamber for high accuracy and precision fission cross-section measurements. *Nuclear Instruments and Methods in Physics Research Section A: Accelerators, Spectrometers, Detectors and Associated Equipment*, 759:50–64, 2014.

[63] P. Konczykowski, B. Fernández-Dominguez, H. Alvarez-Pol, M. Caamaño, G.F. Grinyer, A.T. Laffoley, B. Mauss, J. Pancin, D. Pérez-Loureiro, and T. Roger. Validation of the energy-loss response of α particles in ic4h10 with actarsim. *Nuclear Instruments and Methods in Physics Research Section A: Accelerators, Spectrometers, Detectors and Associated Equipment*, 927:125–132, 2019.

[64] Angel Gutarra-Leon, Cioli Barazandeh, and Walerian Majewski. Atmospheric Muon Lifetime, Standard Model of Particles and the Lead Stopping Power for Muons. In *APS April Meeting Abstracts*, volume 2017 of *APS Meeting Abstracts*, page E2.008, January 2017.

[65] Weinan E, Weiqing Ren, and Eric Vanden-Eijnden. Finite temperature string method for the study of rare events. *The Journal of Physical Chemistry B*, 109(14):6688–6693, 04 2005.

[66] M. Friedman. Gadget: a gaseous detector with germanium tagging. *Nuclear Instruments and Methods in Physics Research Section A: Accelerators, Spectrometers, Detectors and Associated Equipment*, 940, 2019.

[67] FRIB Decay Station Initiator. FRIB Decay Station Initiator, URL: `https://fds.ornl.gov/initiator/`, 2023. Accessed: 2024-02-10.

[68] C.J. Prokop, S.N. Liddick, B.L. Abromeit, A.T. Chemey, N.R. Larson, S. Suchyta, and J.R. Tompkins. Digital data acquisition system implementation at the national superconducting cyclotron laboratory. *Nuclear Instruments and Methods in Physics Research Section A: Accelerators, Spectrometers, Detectors and Associated Equipment*, 741:163–168, 2014.

[69] Mike Folk, Gerd Heber, Quincey Koziol, Elena Pourmal, and Dana Robinson. An overview of the hdf5 technology suite and its applications. In *Proceedings of the EDBT/ICDT 2011*

Workshop on Array Databases, AD '11, page 36–47, New York, NY, USA, 2011. Association for Computing Machinery.

[70] Triangle Universities Nuclear Laboratory. 20na β^+-decay evaluated data, URL: `https://nucldata.tunl.duke.edu/nucldata/GroundStatedecays/20Na.shtml`, 2023. Accessed: 2024-02-26.

[71] Glenn F. Knoll. *Radiation detection and measurement*. John Wiley Sons, 2012.

[72] Haibo He and Edwardo A. Garcia. Learning from imbalanced data. *IEEE Transactions on Knowledge and Data Engineering*, 21(9):1263–1284, 2009.

[73] Burr Settles. Active learning literature survey. Technical Report 1648, University of Wisconsin–Madison Department of Computer Sciences, 2009.

[74] L.K. Hansen and P. Salamon. Neural network ensembles. *IEEE Transactions on Pattern Analysis and Machine Intelligence*, 12(10):993–1001, 1990.

[75] Y. Ayyad, N. Abgrall, T. Ahn, H. Álvarez Pol, D. Bazin, S. Beceiro-Novo, L. Carpenter, R.J. Cooper, M. Cortesi, A.O. Macchiavelli, W. Mittig, B. Olaizola, J.S. Randhawa, C. Santamaria, N. Watwood, J.C. Zamora, and R.G.T. Zegers. Next-generation experiments with the active target time projection chamber (at-tpc). *Nuclear Instruments and Methods in Physics Research Section A: Accelerators, Spectrometers, Detectors and Associated Equipment*, 954:161341, 2020. Symposium on Radiation Measurements and Applications XVII.

[76] Konrad Gadzicki, Razieh Khamsehashari, and Christoph Zetzsche. Early vs late fusion in multimodal convolutional neural networks. In *2020 IEEE 23rd International Conference on Information Fusion (FUSION)*, pages 1–6, 2020.

[77] Christopher D Manning. *An introduction to information retrieval*. Cambridge university press, 2009.